Design Method on Plantship and Cold Water Pipe for Ocean Thermal Energy Conversion (OTEC)

リスティヤント, アディプトラ

https://doi.org/10.15017/2534403

Design Method on Plantship and Cold Water Pipe for Ocean Thermal Energy Conversion (OTEC)

Ristiyanto Adiputra

April 2019

Doctoral Dissertation

Design Method on Plantship and Cold Water Pipe for Ocean Thermal Energy Conversion (OTEC)

Submitted to the Department of Maritime Engineering,
Graduate School of Engineering, Kyushu University,
as a partial fulfillment of the requirements for
Degree of Doctor of Engineering

By:

Ristiyanto ADIPUTRA

Supervised by:

Prof. Dr. Eng. Tomoaki UTSUNOMIYA

Department of Maritime Engineering,
Graduate School of Engineering, Kyushu University

April 2019

ACKNOWLEDGEMENTS

Even though a doctoral dissertation is generally considered as an individual achievement, the processes and the results were supported by numerous people. I am so delighted and so grateful to all who have contributed, encouraged, and accompanied this work.

First and foremost, Prof. Tomoaki Utsunomiya, he is much more than just a `supervisor` for me. He was the person who introduced me this research topic and made me enthusiastic to begin this work. Until the end, he never stopped giving me guidance, encouragement and constructive suggestion. Personally, I am very appreciated and so thankful that at the beginning of my enrolment process, even I had not been granted by any scholarship, he still wanted to accept me as his student and tried his best to find me a proper financial support. He is also a good example of how `a responsible person` should take care of the responsibilities. It is my honoured to be his student.

Prof. Takao Yoshikawa, he was my supervisor at my master degree. Even he was not directly related to my doctoral degree. He was the one who introduced me to Prof. Utsunomiya and also the one who supported me to continue my doctoral degree. Thank you very much for your encouragement.

I also would like to thank to the co-supervisors and the dissertation committee who generously helped me finishing this works by offering their time, support and guidance, Prof. Ikegami, Ass.Prof. Yasunaga, Prof. Jaswar Koto, Prof. Shinoda and other co-supervisors. Thank you very much for your support. I really appreciated that.

I also tender my best thanks to the laboratory members especially the ones who are in the OTEC team. Thank you very much for make enjoy working in this laboratory. Thanks also go to all colleagues and roommates, who made my days always full of joy and laugh.

I would like to deliver my gratitude to my family, my parents, my brother and my sister. Their loving support, continuous encouragement, and sincere interest give me energy to complete my degree.

In the future, when the hardship comes in to my life, I want to read back at this dissertation, not to ensuring that I am a great man having enough power to overcome it but to reminding me that there are a lot of people who love me, support me, and hope for my success. In the future, I want to read this again and again in order to stay an honest and sincere person. I will work hard without hints of shame. I will do my best to be a responsible person as I can.

Thank you very much.

Ristiyanto Adiputra
Japan, May 8th, 2019.

ABSTRACT

Ocean Thermal Energy Conversion (OTEC) is one of the promising renewable energies. Even though its potential is undeniable, it is relatively still unexplored due to high capital cost and unsettled design of the Cold Water Pipe (CWP) for being utilized in commercial scale. Considering these issues as the research background, this dissertation has two main subthemes. The first subtheme, written down in chapter 2, as an effort to reduce the capital cost, introduces a concept design of the floating structure from converted oil tanker ship. The second subtheme, broken down in chapter 3, is to design the Cold Water Pipe (CWP) based on the dynamic stability of the pipe.

Even though the whole chapters discuss all about the component of OTEC plantship, Chapter 2 more focuses on the design of the floating structure but chapter 3 deals with the design of the CWP. Thus, to ease the readers for understanding the contents, Chapters 2 and 3 have each introduction, methods, conclusion and references in specific manners.

In chapter 2, to propose the floating structure design process, the general principles of designing a converted tanker FPSO is adapted and then modified to deal with OTEC characteristic. In the design process, the arrangement of the OTEC layout is carried out by constraint satisfaction method and the prospective floating structure size is varied using Monte Carlo Simulation. The variables in the design process consist of the velocities of cold water and warm water transport, the size of the plantship, and the location of the OTEC equipment to the seawater tank. Constraints are introduced as allowable border to determine the acceptability for particular case including the provided space and buoyancy, and the net power output estimation. The results show that the `typical` size of Suez-max oil tanker ship is the optimum one for the plantship with the velocity of the water transport of 2-3 m/s. The general arrangement is also conceptualized in this chapter.

In chapter 3, OTEC CWP is designed focusing on the effects of internal flow to the stability of the pipe. The design analysis is deliberated to select the pipe material, top joint configuration (fixed, flexible, pinned) and bottom supporting system (with and without clump weight). Initially, a fully coupled fluid structure interaction analysis between the

pipe and the ambient fluid is carried out using ANSYS interface referring an integration of Computational Fluid Dynamics (CFD) and Computational Structural Mechanics (CSM). Separately, the analytical solution is built by taking into account the components of the pipe dynamics and then solved via power series expansion by inserting the boundary conditions at the top joint connection and bottom supporting system. Using scale models, the results obtained from the analytical solution are compared with the ones from numerical analysis to examine the feasibility of the analytical solution. After being verified, the analytical solution is used to observe the dynamic behavior of the CWP for 100 MW-net OTEC power plant in full-scale model. The results yield conclusions that pinned connection at the top joint is preferable to decrease the applied stress, clump weight installation is necessary to reduce the motion displacement and Fiber Reinforced Plastic (FRP) is the most suitable material among the examined materials due to its light weight and high strength.

Gathering the process and results obtained from chapters 2 and 3 together, chapter 2 gives the required main scantlings of the CWP in which will be used as the input data to analyze the stability of the pipe in chapter 3. Chapter 3 states the suitable material of the pipe and the necessity of clump weight installation so that the weight of the riser can be determined and can be used to calculate the total weight in chapter 2.

Table of Contents

List of Figures

List of Table

CHAPTER I
GENERAL INTRODUCTION

1.1 Background

Energy issue is one of the biggest issues in this 21st century. So many efforts have been done to ensure the sustainability of energy supply by changing the contribution of fossil fuel with renewable energy resources. For a country with a big area of sea, one of the prospective ocean energy resources to be developed is ocean thermal energy [I.1].

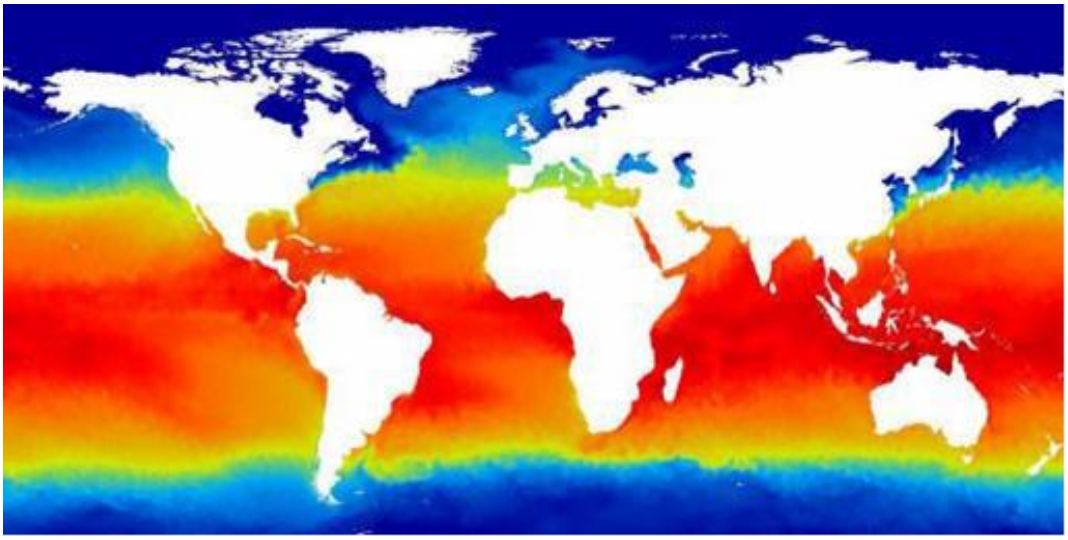

Figure I.1 OTEC potential distribution [I.2]

Figure I.1 above shows the OTEC potential distribution all over the world. Since OTEC uses the temperature difference between sea surface and subsurface, a country with maritime tropic such as Indonesia has a very big potential of OTEC development. Based on study obtained by National Energy Council of Indonesia [I.3], the nationwide ocean energy potentials are listed in table I.1.

Beside the big potency explained above, Indonesia is archipelago state. The problem of energy issues is not just about its supply but also its distribution to cover all area of the lands. Since OTEC is natural ocean energy, it is possible to spread OTEC power plants to cover all area and even for the remote islands. The most important one is that OTEC

requires no fuel, developing OTEC will not require an added technology related to the fossil fuel supply to the power plant. Hence, it is suitable for a remote area such as islands located in the east of Indonesia.

Table I.1 Electrical energy potential from ocean resources in Indonesia

	Theoretical (GW)	Technical (GW)	Practical (GW)
Tidal current	160.0	22.5	4.8
Ocean wave	510.0	2.0	1.2
Ocean thermal	57.0	52.0	43.9

OTEC technology consists of an evaporator, turbine, condenser which are placed on the floating structure. Up to know, OTEC patent applications are led by US, Japan, and European countries. The system of the operation can be world-widely adopted. But in the case of structure, it must be designed based on local environmental condition. Concerning this matter, there are some points to be overcome in order to implement OTEC technology in Indonesia efficiently:

1. Figure I.2 below shows the track and intensity of tropical storm [I.4]. The existing developed floating structures are designed based on severe environmental condition. If this floating structure design is purely adapted to be implemented in Indonesia which has relatively calm sea state, it will be very inefficient, costly and unprofitable.

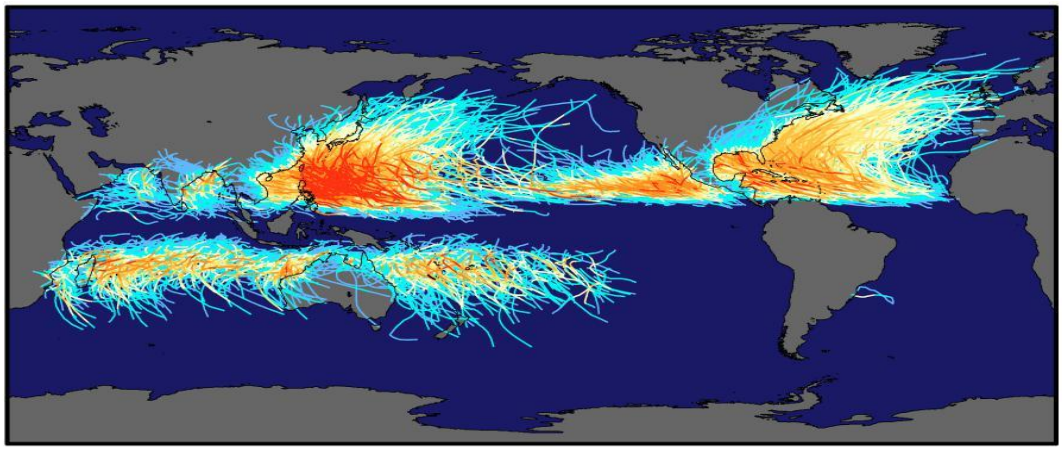

Figure I.2 Track and intensity of tropical storm [I.4]

2. Indonesia has very large sea area. A portable floating structure will give more advantages, especially in disposal activities. But the existing proposed structure for OTEC technology is a fixed structure.

Additionally, the production cost for building new OTEC power plant is relatively high especially for building the floating structure. So, it is necessary to propose a possible way to decrease the production cost. This research introduces a method to minimize the production cost by replacing the role of floating structure with a converted commercial ship concerning the sea environmental condition in Indonesia. Furthermore, the riser also will be developed in this study to get a light riser design with a big capacity of water transport.

The detailed background and introduction for each subtheme (floating structure and riser design) will be presented in corresponding chapters.

1.2 Purpose

The main purpose of this study is *to design an efficient, economical and safe floating structure for OTEC power plant*. In order to achieve the main purpose of the research study, the specific and particular purpose must be obtained including:

1. Determining the required operational capability of the floating structures for OTEC power plants
2. Examining the constraint and design standard to build the failure barriers
3. Analysing required technologies and systems and its possible variants
4. Deciding the final baseline concept design
5. Designing the general arrangements and the plans for each part of structures.
6. Designing the supporting structure (anchoring, riser technology, etc.)

1.3 Scope

There is no limitation on the design process, the more we consider the parameters, the more will the design be efficient and economic. However, considering all parameters is time-consuming. Due to time limitation, the design of the floating structure is focused on the plantship size decision and the location of the OTEC system to the seawater tank. In case of the riser design, the considered excitation is only the effect of the internal flow to the dynamic motion of the riser.

1.4 Outline

This dissertation has 2 main subthemes (chapter 2 and chapter 3) which proceeded by a general introduction and definition in chapter 1 and also followed by the general conclusion in chapter 4. In chapter 1, the research background is explained in general including the potential and the barriers of OTEC technology for the worldwide and for Indonesia especially in which the observed site locates. Along with the research purposes, the scope of the research is also stated in this chapter. In the last part of the chapter, the fundamentals theory of OTEC system will be explained.

In chapter 2, the discussion will be focused on the floating structure design. It covers the overview of recent proposed floating structure in the introduction, the design method, the result of the on-site experiment including the temperature gradient in the observed area, the explanation for each variable, the result of the plantship size decision and the general arrangement.

The third chapter of this dissertation deals with the preliminary design of riser for OTEC application, even though also applicable for the dynamic stability of free hanging riser conveying fluid in general. This chapter also has an introduction discussing the historical sight of OTEC riser and the general theory of free hanging riser conveying fluid which is correlated with the riser for OTEC application. The method and case configuration are explained in the firstly in the big scope. After that, the analysis will be sharpened into analytical and numerical analysis. Using scaled models, analytical solution is compared with the numerical one. After being verified, the analytical solution will be

used to investigate the full-scale of the OTEC riser. The result of this particular chapter will be about the material of the riser, the top joint connection and the necessity of the clump weigh installation.

The last chapter, chapter 4, summarizes what have been done in the previous chapters and concludes the results generally. It also provides some thoughts for future study for both floating structure and riser design.

1.5 OTEC system

Figure I.3 shows the components and process of OTEC cycle. Basically, OTEC system has four main components which are heat exchanger, working fluid, turbine generator and pumps. The warm sea water passes through the evaporator providing heat to the working fluid, in this case ammonia, then the working fluid will form into gas phases. The vaporized ammonia is pumped to drive the turbine and produces the electricity using generator. After that, low pressure working fluid will be condensed into liquid form using the cold water pumped from deep water. To maintain the cycle, the liquid ammonia will be pumped back to the evaporator. This cycle is repeated continuously [I.5].

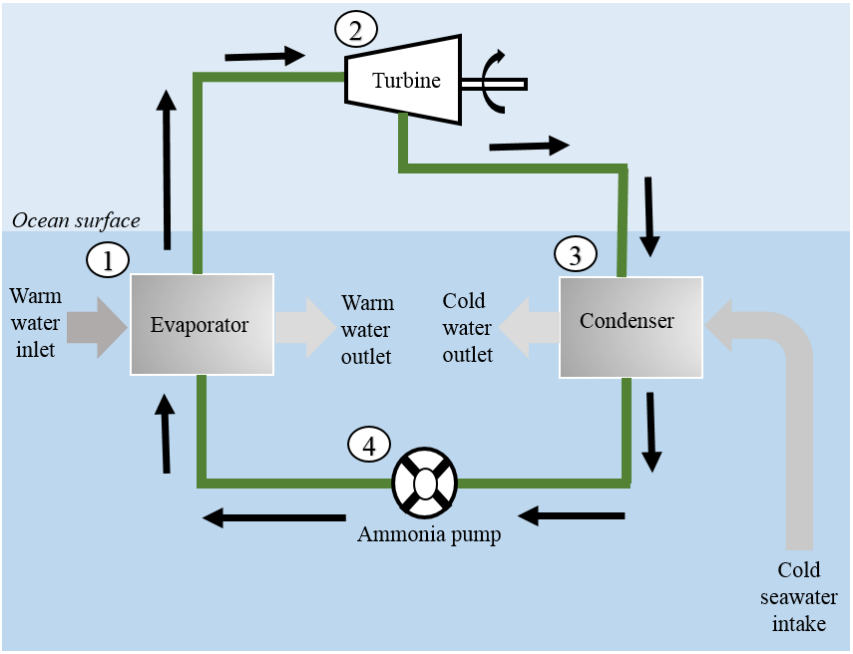

Figure I.3 The process of OTEC cycle

REFERENCES

[I.1] Syamsuddin ML, Attamimi A, et al (2015) OTEC potential in the Indonesian seas. Energy Procedia 65:215 – 222

[I.2] UK Met Office. Heat Content of the Earth's Oceans. 2010. http://www.offinf.com/what_is_otec.htm

[I.3] Mukhtasor (Member of National Energy Council of Indonesia). Ocean Energy Workshop Slide Presentation. 2011. http://energy--indonesia.com

[I.4] Laing Arlene. 2011. Introduction to tropical meteorology. Online book. USA. University Corporation for Atmospheric Research. https://www.meted.ucar.ed

[I.5] Vega LA, Michaelis D (2010) First generation 50 MW OTEC plantship for the production of electricity and desalinated. In: Proceeding of offshore technology conference (OTC 20957). Offshore technology conference, Texas, pp 1-17.

CHAPTER II
PRELIMINARY DESIGN OF THE PLANTHSIP

2.1 Introduction

OTEC is a technology which utilizes the temperature difference between warm surface water and cold deep water. To be deployed in viable and effective way, the temperature gradient between surface and subsurface should be more than 20^{o}C [II.1]. With the surface temperature of about 25^{o}C and deep cold water of 5^{o}C, reduced by the efficiency of OTEC equipment, the efficiency of the Rankine cycle of this system was only about 3-5 percent [II.2]. Ammonia is selected as the working fluid due to its low boiling point which allows it to transform into gas and liquid phases with small temperature difference [II.3, II.4]. Nowadays, with the state of the art of OTEC system technology, the Rankine cycle efficiency of the OTEC system is predicted still around 6-7% [II.5]. Additionally, the system requires around 30% of the gross-energy product to maintain the process especially used for pumping system. The necessity of very high capital investment is also a reason why this technology gets stuck on the pilot project [II.6].

Literature survey on OTEC cost estimation resulted very limited resources which mainly undergone by Vega and Lockheed Martin [II.6- II.13]. It was early assessed by Vega in 1990 resulting a statement that the required cost per kW decreases as much as how bigger the capacity of the power plant is [II.7]. It indicates that developing OTEC power plant in commercial scale is more cost-effective compared with the small scale. Completing the capital cost estimation for 100 MW-Net capacity, in 2003, Vega included the effect of the offshore distance to the estimation yielding result how the capital cost increase with an increase of the offshore distance [II 2.8].

Updating the previous estimation, Vega recalculated the required capital cost in 2010 with considering the recent development of OTEC system technology and its implication to the OTEC system costs [II.9] and then attempting to reduce the capital cost by project fund management scenario [II.6]. Enhancing the cost estimation procedures proposed by Vega, in 2012, Lockheed Martin evaluated the cost estimation for the whole life cycle of

commercial OTEC power plant associated with long-term operation, for 100 MW, 200 MW and 400 MW capacity [II 2.10]. The results of the cost estimation done by Vega and Lockheed Martin are also highlighted in several papers [II.11, II.12]. Gathering information from those studies related to the present paper, some point can be highlighted as follow: 1) For OTEC power plant with capacity more than 50 MW, a floating structure is economically feasible; 2) The required capital cost for building 100 MW OTEC power plant is approximately about 8000 USD/kW which is much higher compared with other renewable energy; 3) The cost of heat exchanger and floating vessel takes the biggest portion of the total cost which is about 21% for heat exchanger and 22% for the floating vessel.

There are limited design concepts for OTEC floating structure available. Some of the proposed designs are just a sketch without appropriate detailed explanations how the arrangement is set [II.6, II.8, II.13]. At the beginning of the early stage study, several projects were carried out to analyze the must-have characteristic of OTEC power plant both for land-based and offshore plants [II.14- II.17]. More detail early stage design of floated OTEC power plant was proposed by George and Richard [II.18]. There are two types of floating structure which are moored barge and grazing barge. Both of them are for 40 MW-net OTEC power plant. Offering more detailed consideration yet remained conventional, Vega conceptualized a barge type floating vessel made from concrete with 250 m length, 60 m breadth, 28.5 m height and draft of 20 m [II.13].

By the end of 20th century, due to the rapid development of other energy resources such as nuclear power plant and coal power plant, the interest on the OTEC development was not so appealing [II.12]. During this period, the improvement of the OTEC floating structure did not show any significant progress except the introduction of semi-submersible and spar type OTEC floating structure by Avery and Wu in 1994 [II 2.19]. In the early 2010s, the rising concern of green energy issues made renewable energy got more attention. After recovery of the OTEC interest, some new `modernized` OTEC floating structures have been proposed. Vega suggested a new-built ship-shaped floating structure for 50 MW-Net OTEC power plant [II.3], Yee designed very large floating structure for OTEC application [II.20] and Lockheed Martin suggested grid connected floating structure type [II.10]. Those new floating structure concepts are to ensure the

safety of the floating structure. Because the designs are made of steel, the new floating vessel cost is higher compared with the conventional one.

The attempt to reduce the capital cost through new design concepts was also undergone by Srinivasan. He designed a floating structure with J-spar type, tensioned-leg platform type and semi-submersible type. Even though the new designs were claimed to be successfully decrease the required size of the floating vessel, the decrease of the floating vessel cost is only about 10% compared with the barge type [II.21]. This number is appreciable but effort is still necessary to get more cost-effective design.

In the term of safety, the capital cost is not the only concern. The proposed floating vessel must be able to sustain the applied load from both external and internal. The configuration must meet the requirements of the OTEC system as well as the convenience of the workforce.

In order to overcome the addressed issues, this paper aims to design and conceptualize a plantship for OTEC floating structure with target of 100 MW-net electricity. Considering the success of building FPSO from oil tanker conversion, its design philosophy is adopted to propose the floating structure for OTEC application. It has been already practically well-known that converting oil tanker ship has some benefits compared with the new built. The two main motivations which persuade to utilize converted oil tanker ship are cost saving benefit and shorter delivery time [II.22, II.23]. Additionally, to reduce the capital cost and parasitic loss energy, this paper also evaluates the most optimum size of the plantship and the arrangement of the OTEC system. To ensure the safety of the plantship, the general arrangement is designed following the guidance notes of OTEC floating structure regulation issued by a classification society [II.24].

In order to bring the technology into commercial scale, it must be profitable, appealing for the investment and ensuring that all the system works. Thus, the performance of the whole electricity power generation system must be evaluated using the actual data on the site. To deal with that issue, the on-site experiment was also conducted to measure the environment of the work and then the data is used as the basic input for the design requirements.

2.2 Design method

In the conventional floating structure design for OTEC power plant, the required capacity for the OTEC system is calculated and the floating structure will be design based on the required capacity. But in the design process of converting oil tanker to be a plantship for OTEC power plant, the provided capacity has been determined by the typical dimension of the oil tanker ship. Thus the OTEC system arrangement must be adjusted to dealt with the limitation capacity of the converted oil tanker ship. In a simple manner, in conventional way, the design of the floating structure follows the OTEC system. But in this case, the OTEC system is the one which follows the capacity of the floating structure.

Even though the idea to utilize the oil tanker ship conversion to be OTEC floating structure is adapted from the success of building FPSO from oil tanker ship conversion, the design process of converting oil tanker ship to be the OTEC floating structure differs with the FPSO design process from oil tanker ship conversion. In the oil-tanker-ship-based FPSO, the cargo hold of oil tanker ship can be directly used as the storage space of the FPSO. Additionally, the cargo condition for oil tanker and FPSO are both in still condition. Thus the applied load is same between oil tanker and the FPSO. In case of OTEC floating structure, the cargo hold of the oil tanker ship must be modified to be the seawater tank and the size must be adjusted to overcome the required size of the seawater tank. In the OTEC system, the seawater tanks are not merely for storage space but also to deliver the seawater from the riser to the heat exchanger which means that the seawater is in flowing condition. This makes the wall of seawater tank not only subject to steady state load but also dynamic load due to seawater flow. Furthermore, the efficiency of the power plant does not only depend on the efficiency of the major components, but also its arrangement and installation [II.2].

Figure II.1 shows the design flowchart. There are two main processes. Initially Monte Carlo Simulation is used to vary the possible size of the oil tanker ship and then for each size of the proposed plantship, constraint satisfaction method is employed to optimize the OTEC system. These two flow design process is correlated in the calculation of net power output.

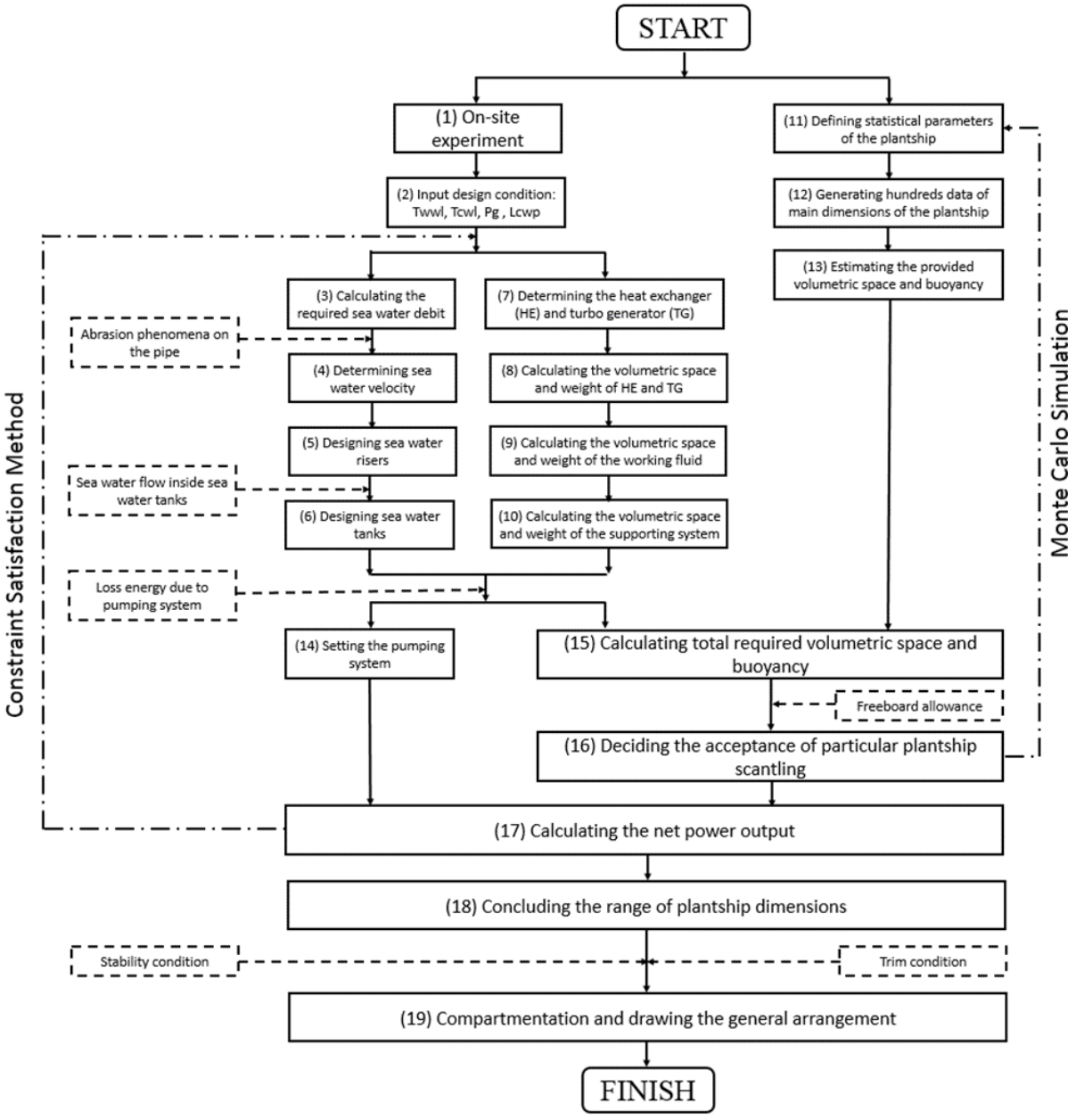

Figure II.1 Floating Structure design process

Constraint Satisfaction Method is a method to narrow down a very large possible solution considering the imposed constraints [II.25]. The purpose of this particular step is not defining the best size of the plantship but rather than categorizing whether the specific size of the plantship is acceptable, rejected or even over-design based on the constraints. Thus, the recommended size of the oil tanker ship is in range. This study also examines the effects of the position of the OTEC equipment to the required work of pumping system.

There are three types of parameters imposed in the design process named as fixed variables, independent variables and constraints. Fixed variables are the parameters which kept constant during the iteration. These parameters entail the environment data of the site and the target of net power output. Independent variables are the parameters which varied during the analysis including the size of the plantship, the velocity of sea water transport and the location of the OTEC equipment to the sea water tank. Constraints are variables set as limitation during the process to ensure the acceptability of the cases. In figure II.1, the constraints are shown in the dotted rectangular shape.

The constraints imposed in this step are constraint due to abrasion phenomena on the seawater pipe, constraint due to seawater flow inside seawater tanks, loss energy due to pumping system and freeboard allowance. After procuring the size of the plantship, the constraint satisfaction method is also used to determine the placement of the OTEC system equipment and the compartmentation of the plantship. The constraints include the stability and trim condition.

In figure II.1, the number inside the parenthesis denotes the procedure order which is also identical to the numbering in the following explanations. In the design process, initially on-site experiment was conducted to measure the surface temperature and gradient temperature decrease at substantial depth. The measurement was done until the temperature difference between the surface water and deep water reached more than 20^{o}C (1). From these data, the required gross power for yielding 100 MW-net electricity and the required length of the risers can be assessed (2).

After acquiring the input design conditions, the constraint satisfaction method can be undergone. The first step is determining the required seawater debit (3). By keeping the seawater debit constant, the required diameter of the risers is calculated for various seawater transport velocities. The limitation of the seawater transport velocity is determined by the constraint due to abrasion phenomena on the pipe (4). Knowing the length and diameter of the risers, its required thickness is estimated considering the properties of the chosen material. Then, the dry weight and wet weight of the risers are estimated to be included in total weight calculation (5).

To deposit the seawater before being delivered to the heat exchanger or spilled out back to the ocean, the seawater tanks are required to be installed. As the seawater transport brings huge momentum which may trigger excessive pressure acting on the seawater tanks, it is important to analyze the fluid phenomena inside the tanks and use the results as constraints to design the seawater tanks. This simulation is done using Ansys inc. interface software. The result of the analysis is the dynamic pressure acting on the seawater walls. Summing up the dynamic pressure obtained from the simulations and static pressure adopted from classNK, the total pressure can be evaluated. The obtained total pressure then will be compared with classNK regulation for tank installation codes. Employing the comparison result, the required size for seawater tanks can be decided for various velocities of seawater transport (6).

Targeting net electricity product of 100 MW with 30% energy loss as the constraint, the major OTEC components including heat-exchanger, turbine-generator and pumps are determined (7). The capacity and dimensions of the components are adopted from well-established manufacturer. This particular step informs the numbers, required space and required weight of major OTEC components (8). The next steps are estimating the volumetric space and weight of the working fluid (9) and supporting systems (10). By adding the required capacities of risers, seawater tanks and major OTEC components with 20 % spare for additional equipment, the total required volumetric space and buoyancy can be computed.

Separately, Monte Carlo Simulation is used to vary the prospective size of the plantship. There are four types of plantship including Afra-max, Suez-max, VLCC, and ULCC. The first step is defining the statistical parameters of the plantship dimensions which cover the length, the breadth, the draft, and block coefficient of the plantship (11). For each type, 250 set of plantship dimensions are generated (12). For every single dimension set, the provided space and buoyancy capacity are estimated (13).

Comparing the provided capacities with the required capacities obtained previously from constraint satisfaction method procedure (15), the acceptance for particular plantship dimension will be determined based on the constraint due to freeboard allowance (16). If the provided capacities are not enough to cover the required one, the

case will be rejected. If the plantship has enough space and buoyancy, the process will continue to the arrangement of OTEC major components.

Adapting the common design practice of cargo hold for oil tanker ship [II.26, II.27], the space for OTEC system components is set to be 80% of the total plantship length locating from forepeak bulkhead to after peak bulkhead. On the deck at the designated draft, the major OTEC components are arranged considering its required space and the piping diagram. The arrangement is done based on the condition where the heat exchanger is located next to seawater tanks and above seawater tanks. The space for heat exchanger is estimated by reducing the provided space for OTEC components with the required space for seawater tanks.

From the arrangement, the length of the pipeline, the joint configurations, elbowing, bending of the pipeline and other piping layout parameters can be approximated to get the coefficients for calculating the pressure difference. The total pressure difference will be used to get the required pump works (14). The net power output can be obtained by reducing the gross power with the required pumps works. This process is repeated for all plantship dimensions and for two OTEC system arrangement layouts (17).

Taking into account the constraint due to abrasion phenomena on the pipe, seawater flow inside seawater tanks, loss energy due to pumping system, and freeboard allowance, the case can be concluded whether it is rejected, recommended or even over design (18). After defining the size of the plantship, a set of scantling is picked up from the range to design the general arrangement (19). The details for each step are broken down in the following sections.

2.3 Independent Variables

2.3.1 Size of the plantship

The size of the plantship was set to be constant based on several types. However, in the real condition, it is merely hard to find the exact size of the plantship. Thus, the size of the plantship in this study is varied using Monte Carlo Simulation. The stochastic data including the mean value of the size is adopted as reported from [II.28, II.29] and the variance of the data is assumed to follow normal distribution. The mean value of the statistical data of the plantship is shown in table II.1. Referring the statistical parameters, 1000 sets data of ship are generated, analyzed and then classified to find the acceptability for the conversion.

Table II.1 Statistical parameters of `typical` dimension of oil tanker ship [II.28, II.29]

Type	Length		Breadth		Draft		Block coefficient	
	Mean (m)	COV (%)	Mean (m)	COV (%)	Mean (m)	COV (%)	Mean (m)	COV (%)
Afra-max	245	12	34	10	16	2.5	0.834	2
Suez-max	285	15	50	11	23	4	0.84	2
VLCC	330	15	55	12	28	5	0.852	1
ULCC	415	16	63	12	32	5	0.86	1

2.3.2 Velocity of sea water transport

The velocity of sea water transport is the base value to determine the size of the risers and seawater tanks. With constant required seawater debit, the higher velocity will make the size of the riser smaller. But high water transport velocity will cause additional dynamic pressure acting on the riser and the seawater tanks. Initially, the velocity of sea water transport through the riser is varied from 2 m/s to 6 m/s with increment of 0.5 m/s.

During the iteration process on the constraints analysis, the velocity of sea water transport above 4 m/s caused exceeded pressure on the top part of sea water tank. Here on ward, the considered velocity is limited from 2 m/s to 4 m/s.

2.3.3 Location of OTEC system to the seawater tanks

The placement of the heat exchanger and turbine generator will affect the piping system which covers around 30% of total energy loss. In this analysis, the OTEC system is placed either above sea water tank or next to sea water tank. If the heat exchanger is located next to sea water tank, the seawater flow direction is parallel to the heat exchanger. This makes the energy loss due to pumping system will be less but the required width of the plantship will be larger. On the other hand, if the heat exchanger is located above the sea water tank, the pumping system will require more energy to pump up the sea water to the heat exchanger, but the compartmentation, construction and maintenance will be easier to do. The sketch of the piping diagram is shown in figure II.2 for OTEC system equipment above seawater tanks and figure II.3 for OTEC system equipment next to seawater tanks.

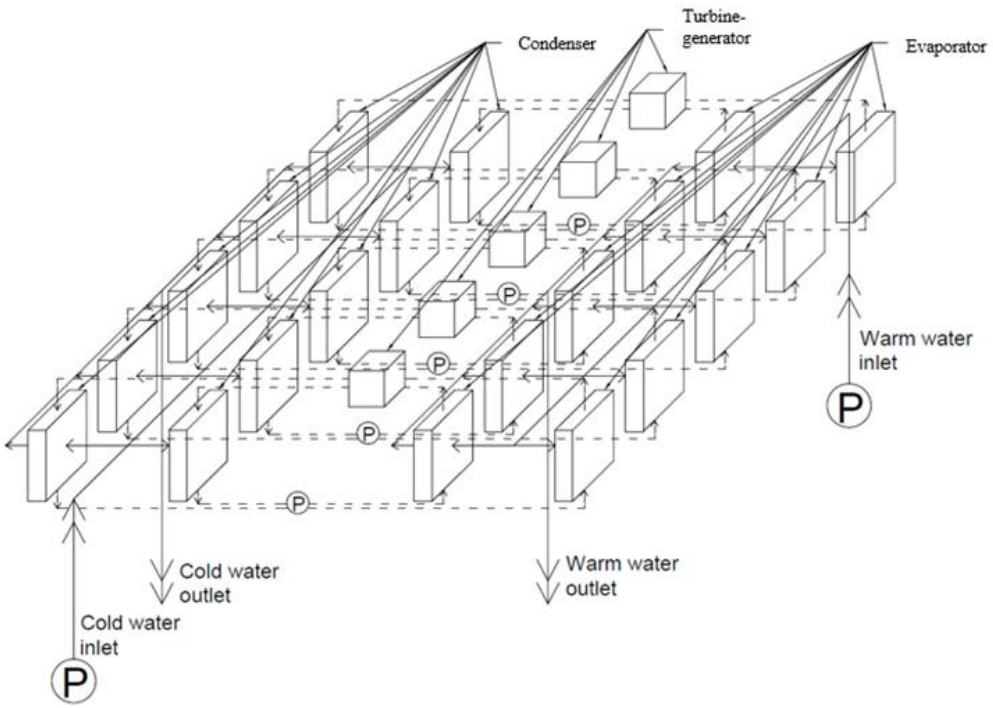

Figure II.2 Piping diagram where heat exchanger is above seawater tanks

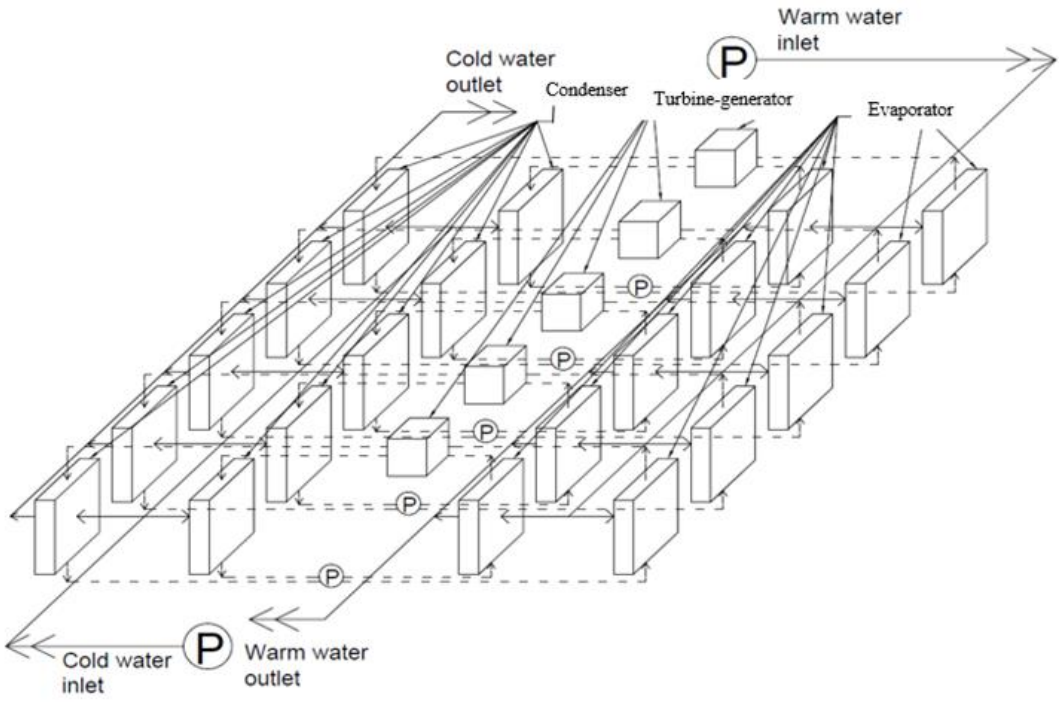

Figure II.3 Piping diagram where heat exchanger is next to seawater tanks

2.4 Fixed Variables

2.4.1 Location of the site

Having tropical ocean, small temperature variation throughout the year and relatively calm seawater make Indonesia one of the countries having huge potential of OTEC development [II.1]. The potential of OTEC development has been studied by several researchers in all around the country. Jaswar Koto et al stated several locations in Indonesia where harvesting OTEC in commercial scale is possible as shown in figure II.4 [II.30- II.32].

Region A is Siberut island located in West Sumatra, region B is North Sulawesi, region C is Morotai island, region D is West Papua, region E is Buru island and region F is Seram island. Koto et al (2017) studied on 100 kW of Ocean Thermal Energy Conversion in Karangkelong, North Sulawesi, Indonesia [II.33]. Considering the number of population and regional development, Siberut island (S 01^{o} 34.660, E099^{o} 14.443) is chosen as the research focus.

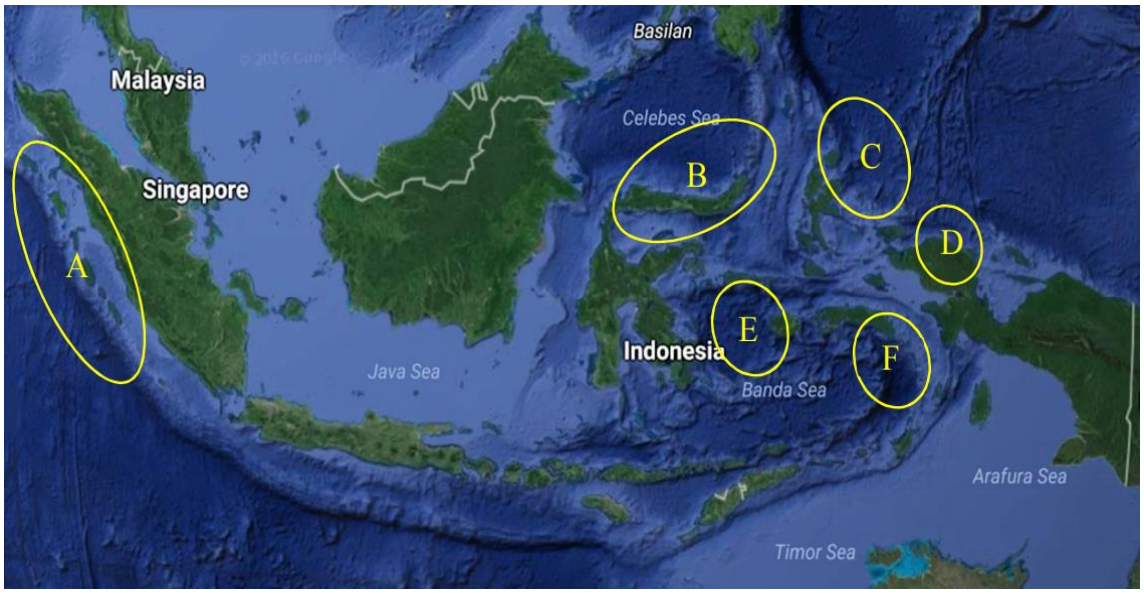

Figure II.4 Piping diagram where heat exchanger is next to seawater tanks

On-site experiment was conducted to measure the temperature profile in the substantial depth. It was undergone from 15th to 20th August 2017. The result is shown in figure II.5 [II.34]. This result is used to determine the surface and deep water temperature and the required length of cold water pipe. As shown in figure II.5, the temperature difference between surface and deep water has been more than 20^{o}C at the depth of 700m. The warm surface water temperature of the Indonesia ocean is affected by the monsoon cycle. The southwest monsoon influences the dry season from June to October and the northwest monsoon causes the rainy season from November to March. The difference of the surface water temperature between the peak of rainy season and the peak of dry season in Mentawai island is about 2^{o}C [II.35]. To bear the uncertainties, the cold sea water will be risen from water depth of 800 m with consideration that the temperature difference between surface water and water depth of 800m is above 20^{o}C for both dry and rainy season.

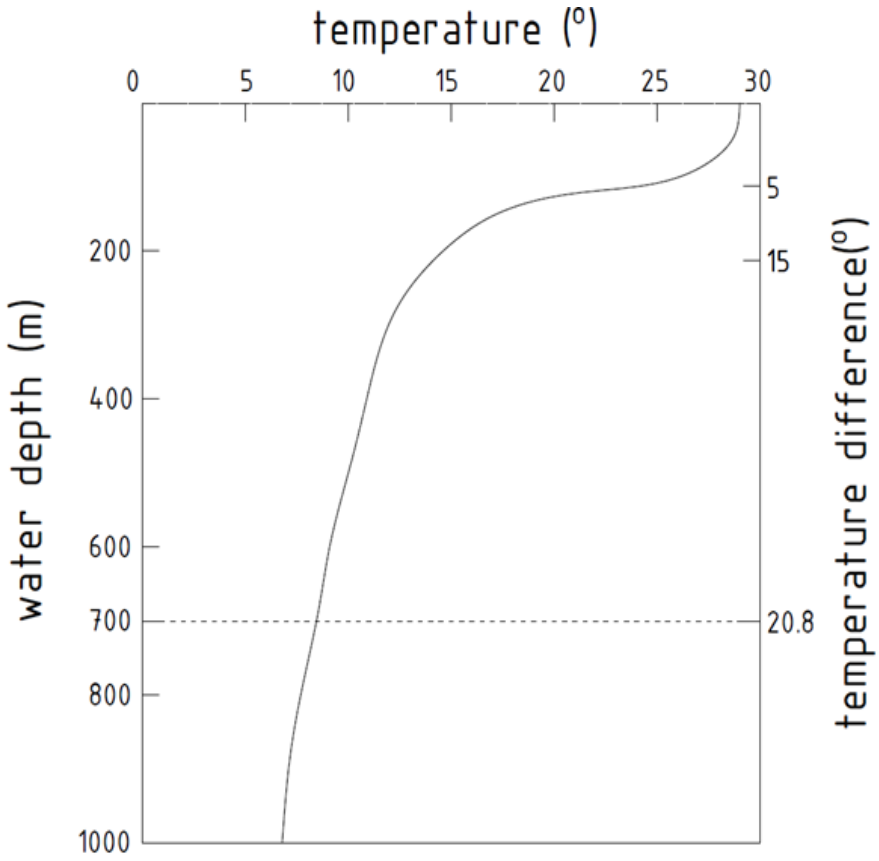

Figure II.5 Temperature profile of the site

2.4.2 Required flowrate

Nihous proposed standard temperature ladder during OTEC process [II.36]. Form the scheme drawn in figure II.6, the gross electrical power P_g can be written as:

$$P_g = \frac{3\rho c Q_{cw} \gamma \varepsilon_{tg} (\Delta T)^2}{16(1+\gamma) T_w} \quad \text{(II.1)}$$

where ρ is the density of sea water in kg/m^3, c is the specific heat of seawater, as 4 kJ/kg K, Q_{cw} is cold water flow rate in m^3, T_w is the temperature of warm surface water in K, ΔT is the temperature difference between warm water and cold water in K, ε_{tg} is the turbine-generator efficiency and γ is the ratio between warm water and cold water flowrate.

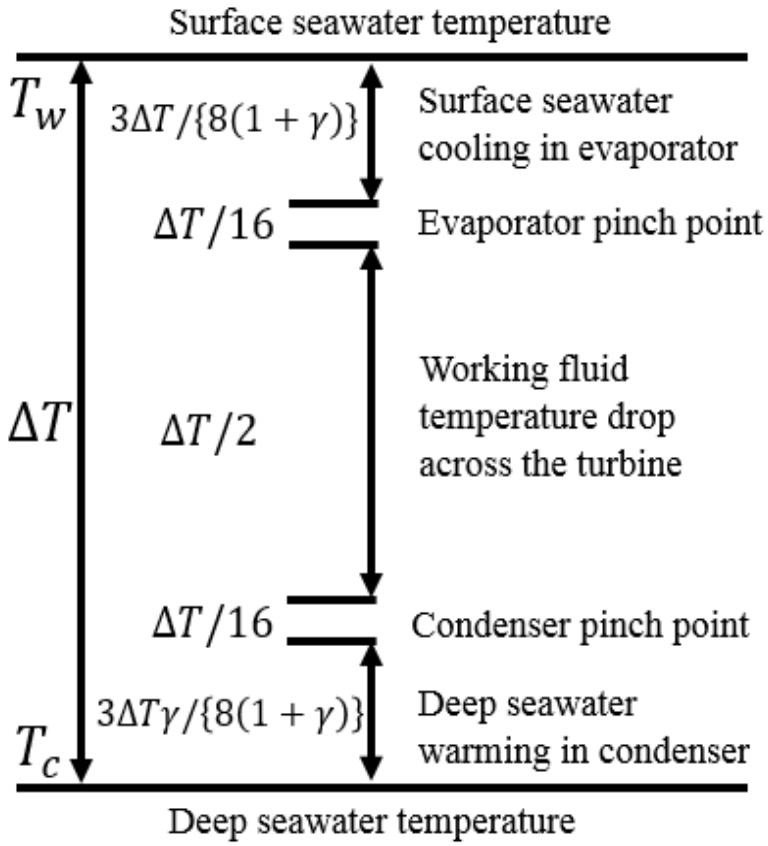

Figure II.6 Nihous temperature ladder model during OTEC process [II.36]

Next step is breaking down the equation of gross power output into net power output equation. The loss energy is mainly due to power consumption to transport the seawater through an OTEC system. This parasitic power consists of two main parts. The first part is the energy to sustain the given deep sea water flow rate as 18% P_g at design and the second is the loss energy which varies if γ is adjusted, e.g. $\{0.12(\gamma/2)^{2.75}\}$ times P_g at design [II.8]. From the simplified theory above, the net power output can be calculated as

$$P_n = \frac{\rho c Q_{cw} \varepsilon_{tg}}{8T_w}\left(\frac{3\gamma(\Delta T)^2}{2(1+\gamma)} - 0.18\left(\Delta T_{design}\right)^2 - 0.12(\gamma/2)^{2.75}\left(\Delta T_{design}\right)^2\right) \quad \text{(II.2)}$$

By setting up the value of γ equal to 2 and assuming that the absolute sea water temperature is fairly constant ($T \cong T_{design}$), the parasitic power can be represented as decrease of $\{0.3\Delta T^2{}_{design}\}$ imposed on ΔT in Eq. (II.2) [II.36]. As stated in [II.36], typical OTEC plant configurations consume about 30% of P_g.

Inputting the value of warm and cold surface temperature from on-site experiment data, it corresponds to a total deep water flowrate of 2.3 m^3/s per MW (net) at design condition γ equal to 2. In this research, the addressed net power output is 100 MW. Thus, the required flow rate will be 230 m^3/s for cold sea water and 460 m^3/s for warm sea water. The required flowrate is kept constant during the design process.

2.4.3 Required OTEC system equipment

2.4.3.1 Risers design

The risers are utilized to transport seawater from the ocean to the seawater tank and vice versa. There are 4 risers suspended on the bottom of the plantship which are inlet cold water pipe, outlet cold water pipe, inlet warm water pipe and outlet warm water pipe. The thickness was estimated using the approximation formula for riser of oil and gas exploration [II.37]. The features of the cold water pipe were adopted here as reported in [II.13]. The Cold Water Pipe (CWP) is made of a Fiberglass reinforced plastic sandwich construction with laminate density of 4125 kg/m^3; the density of syntactic foam of 1015 kg/m^3; modulus of elasticity of 13776 MPa; and the flexural rigidity of $2.89x10^{11}$ Nm^2. The result of the estimation is shown in table II.2.

Table II.2 Main dimensions of the risers

Riser	Length (m)	Average thickness (cm)	Thickness of fiberglass layer (cm)	Thickness of syntactic foam (cm)
Cold water inlet (CWP inlet)	800	16	2	14
Cold water outlet (CWP outlet)	40	8	0.8	7.2
Warm water inlet (WWP inlet)	20	6	0.5	5.5
Warm water outlet (WWP outlet)	40	8	0.8	7.2

2.4.3.2 Heat exchanger, turbine generator and pumps

In this present study, the system and its components of the heat exchangers are simply adopted. Uehara and Ikegami found that plate-type heat exchanger is the best fitted for OTEC [II.2]. Thus, this study adopted the compact plane-fin heat exchanger developed by Argon National Laboratory, USA. The core dimensions of this compact plane-fin heat exchangers are 6.1 m (*L*) x 1.2 m (*B*) x 4.6 m (*H*) [II.3, II.38]. To produce 4 MW-gross power, four heat exchanger cores are required to assembly the submodules. With assumption that the energy loss is about 30% of the total gross power, 36 evaporator and condenser submodules must be integrated to get 100 MW-net.

Table II.3 Volumetric space of heat exchanger and turbine-generator.

Items	Total	Units	Volumetric spaces
Turbine-generator	9 units	Core dimension	12 m (*L*) x 8 m (*B*) x 5 m (*H*)
		Total dimension	30 m (*L*) x 40 m (*B*) x 6 m (*H*)
Evaporator and condenser	36 submodules each	Heat exchanger is located above sea water tanks	
		4 MW-gross assembly	6.1 m (*L*) x 5 m (*B*) x 5 m (*H*)
		4 MW-gross assembly including flanges	10 m (*L*) x 8 m (*B*) x 8 m (*H*)
		Total dimension	100 m (*L*) x 40 m (*B*) x 8 m (*H*)
		Heat exchanger is located next to sea water tanks	
		4 MW-gross assembly	6.1 m (*L*) x 2 m (*B*) x 8 m (*H*)
		4 MW-gross assembly including flanges	10 m (*L*) x 4 m (*B*) x 13 m (*H*)
		Total dimension	100 m (*L*) x 10 m (*B*) x 8 m (*H*)
Pump	150 units	Warm water pump 100 units	100 m (*L*) x 40 m (*B*) x 6 m (*H*)
		Cold water pump 50 units	50 m (*L*) x 40 m (*B*) x 6 m (*H*)
		Total dimension	150 m (*L*) x 40 m (*B*) x 6 m (*H*)

The technology of turbine-generator has been developed in the market and available from well-established manufacturer [II.3]. The maximum capacity is about 15 MW-gross with dimensions 12 m (*L*) x 8 m (*B*) x 5 m (*H*). Totally 9 turbine-generator are required. The pumps used to transport the seawater and working fluid are also inputs from a manufacturer [II.39]. The capacity per unit pump is 18000 m^3/h. The core dimensions of the pump are 9 m (*L*) x 3.5 m (*B*) x 6 m (*H*) including motor and 3.5 m lifting height. The volumetric space of heat exchanger, turbine generator, and pumps is listed in table II.3. It depends on the location of heat exchanger and turbine-generator to the sea water tank.

2.5 Constraints

The constraints induced in this design procedure can be categorized into two functions. The constraints due to abrasion phenomena on the pipe, seawater flow inside seawater tanks, loss energy due to pumping system and freeboard allowance are used to determine the size of the plantship. The constraints due to stability and trim condition are utilized to design and conceptualize the general arrangement of the plantship.

To minimize the required length of the submarine cable, the plantship is floated on the ocean where its local depth is more than the required but close to the shore as near as possible. Thus the distance between seabed and the intake of cold water pipe is relatively close. The deep seawater transported along the seawater pipe will contain sand particle. The friction between the pipe and the seawater will wear the surface of the pipe. The excessive velocity of seawater transport may cause material degradation which gradually trigger the failure relating the piping integrity. The abrasion phenomena are imposed to the design procedure to limit the allowed velocity of the seawater transport. The erosive wear equation is adopted from [II.40]. The estimation yields a result that by setting up the lifetime of the cold water pipe of 25 years, the critical velocity of seawater transport is 3.7 m/s.

The seawater will be stored in the seawater tank before distributed to the heat exchanger. As calculated in section 2.4.2, the required debit of the seawater is so large. This amount of seawater flowrate coming up from the outlet seawater pipe with certain velocity will convey massive momentum. At this point, analyzing the flow inside seawater tank is very crucial to be undertaken. The result of this particular analysis will be used as the constraint to decide the size of the seawater tanks. The analysis will be done using a commercial software named Ansys interface. The detail will be explained in section 2.5.1.

The next constraint is due to loss energy for pumping system. This constraint is to decide the arrangement of the OTEC system including the heat exchanger, turbine-generator and the pumps. The arrangement plan will be used to estimate the required space and buoyancy of the OTEC system. The detail of the pumping power estimation and the net power output calculation will be described in section 2.5.2.

By comparing the required buoyancy and space with the provided capacities, the acceptance of a particular set dimension of a plantship can be determined. This constraint is named as the constraint due to freeboard allowance. The space for OTEC system equipment including the seawater tanks will be located between forepeak bulkhead and after peak bulkhead. The required space depends on the size of seawater tanks which are decided by the constraint due to seawater flow inside seawater tanks and by the arrangement of the OTEC system equipment which is yielded from the constraint due to pumping power. In the case of the required buoyancy estimation, it will be broken down specifically in section 2.5.3.

After obtaining the possible size of the plantship, the next step is setting the general arrangement. To ensure the safety, constraint due to stability and trim condition are imposed to the design procedure. This analysis is also to assess the necessity of ballasting system. The method for analyzing the statistic stability is adopted from [II.26] and then modified to take into account the effects of riser installation. To ensure that the floating structure has adequate stability, IS code is adopted as a parameters guidance [II.24]. For trim estimation, the calculation process is done reffering [II.27]. The common understanding considers that plantahip trim less than 1% of LPP is recommended.

2.5.1 Required size of seawater tank

If the wall of seawater tank does not have adequate distance from the riser, the wall will be subject to pressure caused by seawater momentum delivered during the transportation. As the plantship is converted from an existing stucture, the applied load must not exceed the design load at the initial design condition. The total applied pressure consists of static pressure loading and dynamic pressure loading. The static pressure loading formulation is adopted from ClassNK regulation [II.41] and the dynamic pressure loading is obtained from Ansys interface simulation using Ansys CFX and Ansys Structural [II.42- II.44]. The total applied pressure is then compared with the allowable pressure acting on the wall of the seawater tanks adopted from ClassNK regulation.

The second constraint is the area of sea water tank, A_{swt}, compared with the cross section area of the risers, A_r. Insuffcient area of sea water tank in a ceratin level of seawater transport velocity will increase the pressure difference in the pumping system

calculation as shown in equations II.5 and II.12. The simulation is carried out by varying the value of A_{swt}/A_r from 10 to 50 with an increment of 5.

The case configuration for the Ansys interface simulation and required pumping power estimation due to change of area of seawater tank is listed in table II.4. The details of the analyzed dimension of seawater tank are drawn in figure II.7. Results intended from this particular analysis are minimum distance between riser and side wall of sea water tank, , minimum height of the tank, Ht , and minimum area of the tank, $Lt\ x\ Bt$.

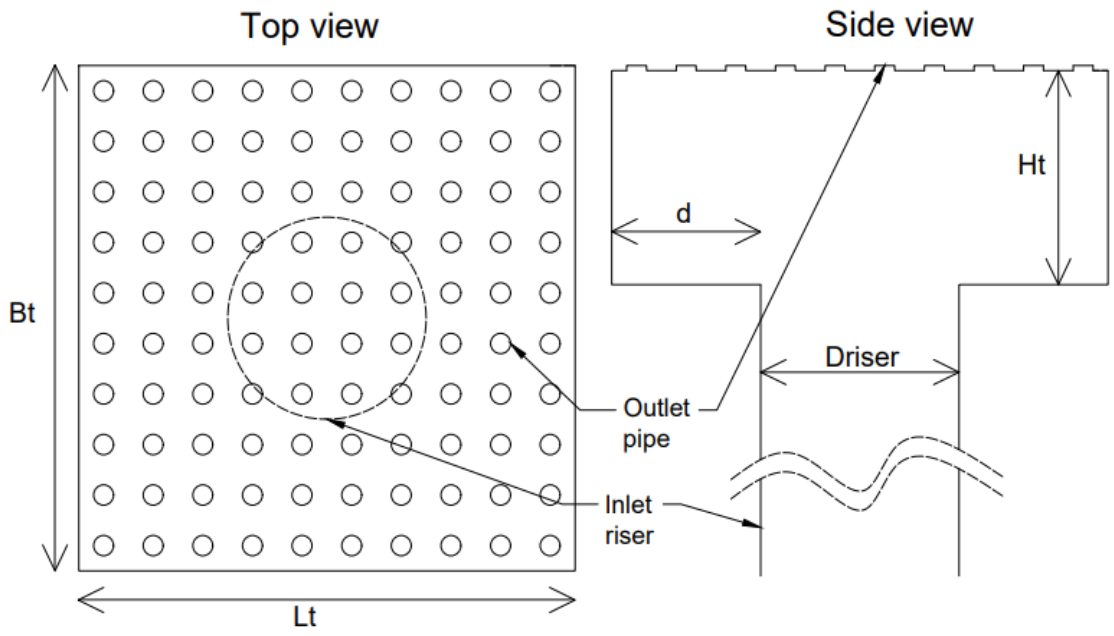

Figure II.7 Seawater tank dimension

The Ansys interface simulation refers to the coupled analysis between Computational Structural Mechanics (CSM) and Computational Fluid Dynamics (CFD). The input data initially is set using CFD in the inlet and outlet boundary condition. The CFD simulation then brings the loads from the fluid dynamics to the strcutural analysis. In the modelleing process, the stucture is divided into three parts which are inlet pipe, outlet pipe and tank walls. Inlet pipe immitates the seawater pipe and outlet pipe is used to model the pipe connecting seawater tanks and heat exchanger. However, to model the whole length of cold water pipe is simply imposible due to software license limitation. Thus, the inlet pipe only covers the 1 m upper part of the cold water pipe. The effect of the shortened inlet pipe model is taken into account in the boundary definition process. Because the main

purpose of the simulation is to measure the pressure acting on the wall of seaweter tanks, the wall of the tanks is modeled as rigid wall which means the shape of the seawater tanks remain the same during the simulation. The convergence analysis is also carried out to define the optimum mesh size. The detail of the model scantling is listed in table II.4.

Table II.4 Case configuration for seawater tank size analysis

Dimension	Variation of scantling			Variation of seawater velocity			Fixed variables	Total cases
	Min	Max	Increment	Min	Max	Increment		
H_t	8 m	19 m	1 m	2 m/s	6 m/s	1 m/s	d= 20 m; $A_{swt}/A_r = 5$	60
d	5 m	25 m	5 m	2 m/s	4 m/s	1 m/s	h= 18 m; $A_{swt}/A_r = 5$	15
A_{swt}/A_r	5	50	5	-			d= 20 m; h = 18 m	10

The boundary condition of the system is numbered as shown in figure II.8 and detailed in table II.5. The environment setting is set so the velocity of seawater transport at the inlet is same with the designed case.

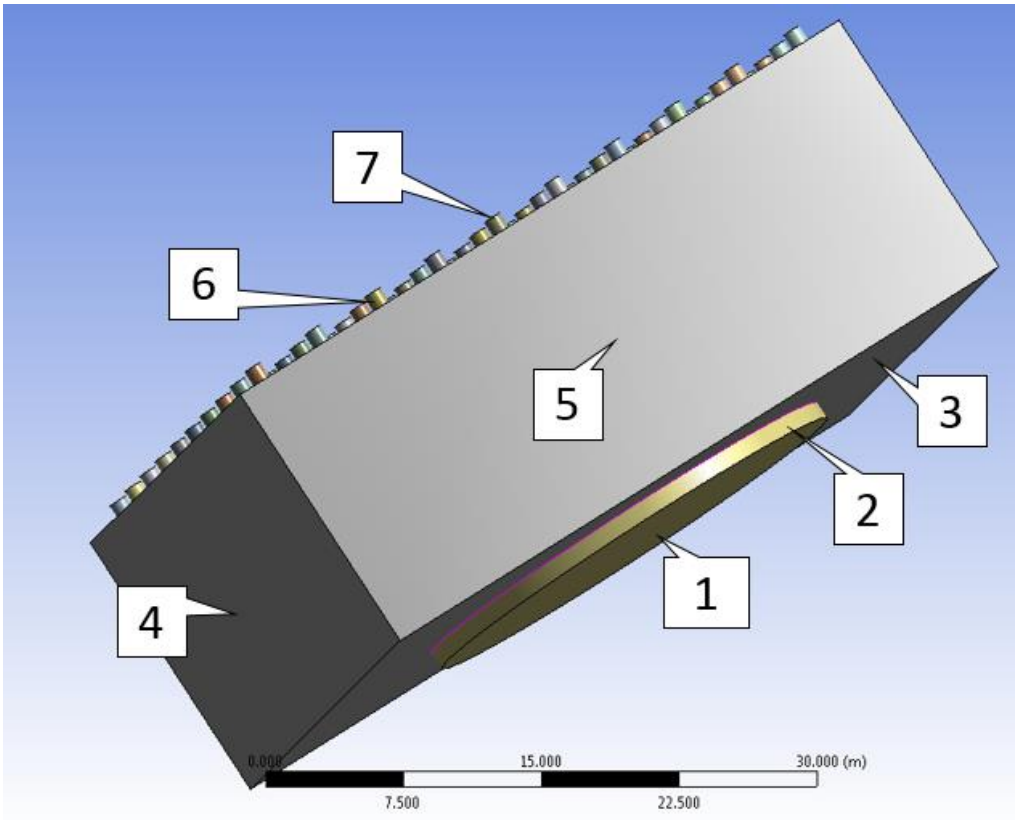

Figure II.8 Boundary condition for Ansys interface simulation

Table II.5 Detail of the boundary condition for Ansys interface simulation

No	Part of the model	Boundary condition	Input data
1	Inlet surface of the inlet pipe	Inlet	Velocity of seawater transport
2	Wall of the inlet pipe	Rigid wall	-
3,4,5	wall of the seawater tanks	FSI interface	Load received from structural analysis
6	Wall of the outlet pipe	Rigid wall	-
7	Outlet surface of the outlet pipe	Opening	Fluid pressure received from fluid dynamic analysis

Figure II.9 shows the sample result for analyzing the minimum distance between riser and sidewall of the tank. In the sample model, the distance between riser and sidewall of the tank is 20 m and the velocity of the seawater transport is 2 m/s. As the model has symmetrical scantlings, the pressure distribution for all side walls is identic.

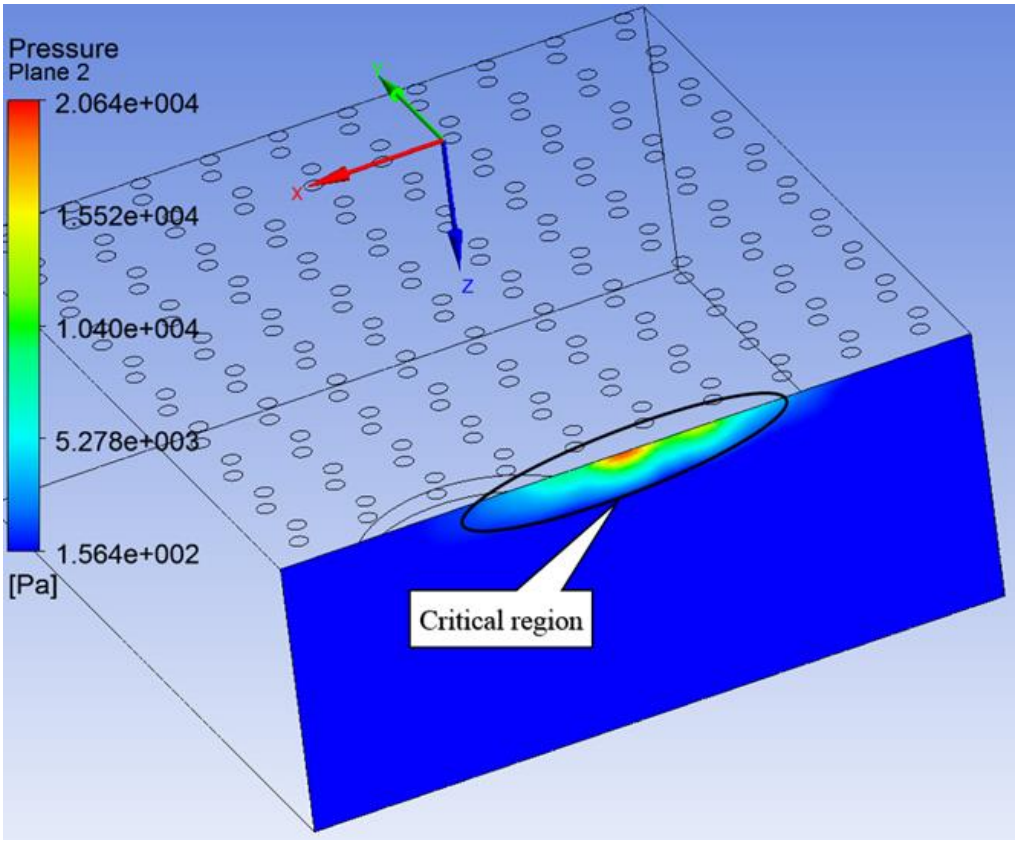

Figure II.9 Sample of numerical result for distance between riser and sidewall of 20 m with seawater transport of 2 m/s

Figure II.9 only shows one part of the sidewall tank. The critical region is rendered in red and pointed inside the cycle. In the ClassNK regulation for designing fluid tanks, the rule states that the maximum allowed pressure acting on the whole surface of the wall should not be more than the value defined by the regulation. Thus, the maximum value of the pressure distribution is taken as the dynamic pressure. This procedure is repetead for all other cases. The collective results will be discussed in the following section.

2.5.2 Net power output product

Equation II.2 is built by assuming that the pumping system will use about 30% of gross energy product. As the pumping system is affected by the layout, it must be analyzed considering the general arrangement plan of the plantship. The elements of the pumping system such us piping diagram, flange position, piping elbow and other elements must be set so the required pumping powers do not exceed the assumption. Basically the pumping system embodies warm sea water pumping system, cold water pumping system, and working fluid pumping system. The equation to calculate the loss energy due to pumping system has been explained detail in [II.2]. The schematic OTEC plant proposed in [II.2] does not have seawater tanks installation. Thus the equation to calculate the total pressure difference adapted from [II.2] has been modified in this present study to involve the pressure drop on the seawater tanks.

2.5.2.1 Working fluid pumping power

The working fluid pumping power E_{wf} is given as [II.2]

$$E_{wf} = m_{wf}\Delta P_{wf} g/\eta_{wfp} \tag{II.3}$$

m_{wf} is working fluid mass transported along the pipe. This mass change depends on its form during the cycle. g is gravity accceleration. η_{wfp} is the efficiency of the working fluid pump. ΔP_{wf} is the the total pressure difference of the working fluid piping modified from [II.2] as

$$\Delta P_{wf} = \left(\Delta P_{wf}\right)_S + \left(\Delta P_{wf}\right)_p + \left(\Delta P_{wf}\right)_c \tag{II.4}$$

$\left(\Delta P_{wf}\right)_S$ is saturation pressure difference between condenser and evaporator as [II.2]

$$\left(\Delta P_{wf}\right)_S = (P_E - P_C)/\rho_{wf} g \tag{II.5}$$

where ρ_{wf} is the density of the working fluid

$\left(\Delta P_{wf}\right)_p$ is pressure difference of the working fluid along the pipes [II.45]. This pressure difference relies on the piping diagram which is a sum of the pressure difference

on the straight pipes $(\Delta P_{wf})_{SP}$ and the bending loss $(\Delta P_{wf})_{B}$. It simply can be defined as [II.45].

$$(\Delta P_{wf})_{p} = (\Delta P_{wf})_{SP} + (\Delta P_{wf})_{B} \quad \text{(II.6)}$$

Where

$$(\Delta P_{wf})_{SP} = 6.82 L_{wf}/{D_{wf}}^{1.17}(V_{wf}/C_{wf})^{1.85} \quad \text{(II.7)}$$

L_{wf} is the length of working fluid pipe, D_{wf} is the diameter of the working fluid pipe, V_{wf} is the velocity of the working fluid and C_{wf} is the roughness coefficient of the pipe.

$$(\Delta P_{wf})_{B} = (\gamma_I + \gamma_V + \gamma_S + \gamma_J + \gamma_O + \gamma_E + \gamma_D + \gamma_R){V_{wf}}^2/2g \quad \text{(II.8)}$$

γ is loss coefficient and indexes are I for inlet, V for valve, S for separating, J for joint, O for outlet, E for elbow, D for diffuser, R for reducer. These loss coeffcients are referred from the reference [II.45]. These coefficients are not a single value. They are calculated based the several parameters which vary depending the local partitions. For example, calculating the loss coefficient due to joint connection, γ_J, it is required to consider the type of the connection, the direction of initial flow, and the elongation angle of the joint connection. Thus the value of γ_J for joint connection between pipes from seawater tank to the heat exchanger, from heat exchanger to the turbine, and other pipe connections will be different. Additionally, although the philosophy of the calculation is same, but the calculation depends on the piping configuration, the concrete values of these loss coefficients cannot be literally referred to the other cases.

$(\Delta P_{wf})_{C}$ is pressure difference of the working fluid side the condenser. This pressure difference can be read as [II.2]

$$(\Delta P_{wf})_{C} = \alpha_C \times {V_{wf}}^2/2g \times l_C/(D_{eq})_{C} \quad \text{(II.9)}$$

α_C is coefficient which depends on the Reynolds number of the working fluid inside condenser, Re_{wf} as $6.19 \times 10^6 {Re_{wf}}^{-1.21}$, l_C is the length of the condenser plate and $\left(D_{eq}\right)_C$ is the equivalent diameter of the condenser.

2.5.2.2 Sea water pumping power

Seawater pumping power E_{sw} consists of warm water pumping power E_{ww} and cold water pumping power E_{cw}. The philosophy and principe to calculate the required work for both are the same. Here the general equation to calculate the required pumping power for seawater are broken down. To transfrom the equation, the index sw is just simple changed to ww for warm water pumping and cw for cold water pumping. The seawater pumping power E_{sw} is calculated as [II.2]

$$E_{sw} = m_{sw} \Delta P_{sw} g / \eta_{swp} \tag{II.10}$$

m_{sw} is seawater mass transported along the pipe. η_{swp} is the efficiency of the seawater pump. ΔP_{sw} is the the total pressure difference of the sea water piping modified from [II.2] as

$$\Delta P_{sw} = (\Delta P_{sw})_p + (\Delta P_{sw})_E + (\Delta P_{sw})_{SWT} \tag{II.11}$$

$(\Delta P_{sw})_p$ is pressure difference of the seawater pipes, $(\Delta P_{sw})_E$ is pressure difference of the working fluid side the heat exchanger [II.2]. The procedure to calculate these pressure differences are the same as equation for calculating the pressure difference for the working fluid as stated in equations II.6- II.9. $(\Delta P_{sw})_{SWT}$ is the depth of seawater on the tanks transported per one second.

In the case of cold water pumping system, the pressure difference calculated in equation II.11 is added by the pressure difference due to density change between warm water and cold water as [II.2]

$$(\Delta P_{cw})_D = l_{cw} - \frac{1}{\rho_{cw}} \left(\frac{1}{2} (\rho_{ww} + \rho_{cw}) l_{cw} \right) \tag{II.12}$$

ρ_{ww} is the density of warm water sea and ρ_{cw} is the density of cold water sea.

2.5.3 Required buoyancy

Required buoyancy is the total weight of the structure and all equipment with added margin of 5% to bear the uncertainties. The total weight of the plantship can be broken down into two main parts which are the weight of the OTEC system equipment and the weight of the supporting system. The supporting system refers to all part of the plantship which does not directly correlate with OTEC process. This weight embodies weight of the steel, accommodation, crew, station keeping system and navigation equipment, sanitation, fresh water and storage, etc. The approach to calculate this weight has been widely known as it is not far different with other types of floating structure [II.46- II.47]. Thus, this part emphasizes more on the estimation process for the weight of the OTEC system.

2.5.3.1 Weight of the riser

From the main dimension of the risers listed in table II.3 and its material properties, the total weight of all riser suspended on the risers is obtained as shown in table II.6.

Table II.6 Weight estimation of the risers

Parameter	CWP inlet	CWP outlet	WWP inlet	WWP outlet
Laminate thickness outer (m)	0.01	0.004	0.0025	0.004
Laminate thickness inner (m)	0.01	0.004	0.0025	0.004
Foam thickness (m)	0.14	0.072	0.055	0.072
Average diameter (m)	12	7 (2 pairs)	10 (2 pairs)	10 (2 pairs)
Total cross sectional area (m^2)	6.03	3.02	3.20	4.27
Cross sectional area of foam (m^2)	5.28	2.71	2.94	3.85
Cross sectional area of laminate (m^2)	0.75	0.30	0.27	0.43
Dry weight (kg/m)	8462	3997	4080	5662
Wet weight (kg/m)	2423	983	878	1392
Total weight (ton)	1700	39	17	56

2.5.3.2 Weight of the heat-exchanger, turbine-generator and pumps

The weight of the heat exchanger, turbine generator and pump is adopted from the manufacturer`s catalogue as shown in table II.7. The supporting equipment such as piping line, pump, flange is calculated referring the sketch as drawn in figures II.2 and II.3 for particular cases of the plantship size.

Table II.7 Weight estimation of main OTEC equipment.

Unit	Weight/item including flanges(ton)	Total weight (ton)
Turbine (9 units)	90	810
Evaporator (36 submodules)	2200	19800
Condenser (36 submodules)	2200	19800
Pump (150 units)	8	1200

2.5.3.3 Weight of the fluids on board

The fluids on board cover the weight of the working fluid and seawaters either circulated through the OTEC equipment or deposited in the tanks. The calculation of the weight of the circulated working fluid is done considering temperature ladder shown in figure II.6 and energy balance of the system as shown in figure II.10. The weight of the working fluid in storage is set as 30% of the weight of circulated working fluid. In case of seawater, its weight depends on the size of the seawater tank. To avoid free surface effect on the seawater tank, the seawater tanks must be in fully-loaded condition.

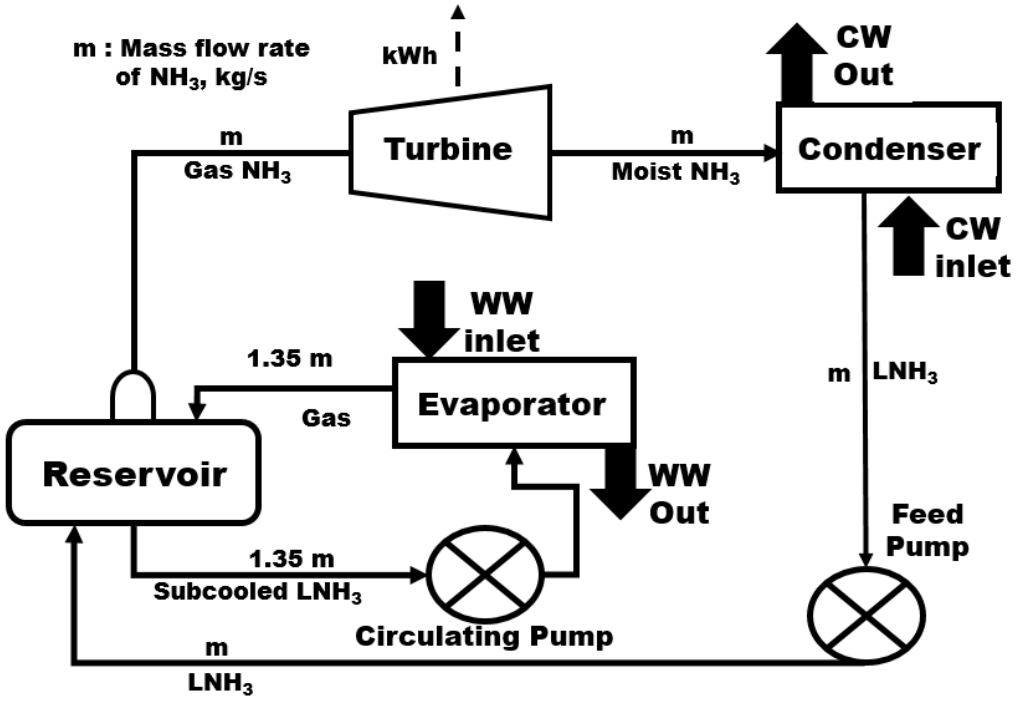

Figure II.10 Energy balance during the OTEC cycle

2.6 Results

2.6.1 Calculation results for net power output estimation

The equation to govern the net power output can be derived as follow

$$P_n = P_g - \left(E_{wf} + E_{ww} + E_{cw}\right) - P_a \quad \text{(II.13)}$$

P_n is gross power output calculated using equation II.1. P_a is additional required power for lightening, control system and other supporting system which assumed to be 5% of P_g. E_{wf}, E_{ww}, and E_{cw} are required pumping power defined in section 2.5.2.

Since net power estimation is done for all plantship dimensions which has sufficient space and buoyancy, the results of the net power estimation are also as many as the number of the analyzed plantship. Obtaining the required pumping power for particular plantship size, the data will be analyzed using statistical formulation to get its mean value. The mean value obtained here is also investigated for both the condition where the heat exchanger is located above seawater tank and next to seawater tank. In the case of Afra-

max type, firstly all of its stocastic dimensions are rejected due to insufficient space and bouyancy. To overcome this matter, a deeper draft is adjusted until it has sufficient space and buoyancy. By this method, the net power estimation for Afra-max also can be undergone. However, at the end of the design process, Afra-max type is excluded in the process due to deficient freeboard allowance.

Figure II.11 is a histogram graph showing the net power output estimation for Suez-max plantship with seawater transport velocity in the OTEC system of 2 m/s and the location of the heat exchanger is next to seawater tank. The mean value of this case is about 100.2 MW.

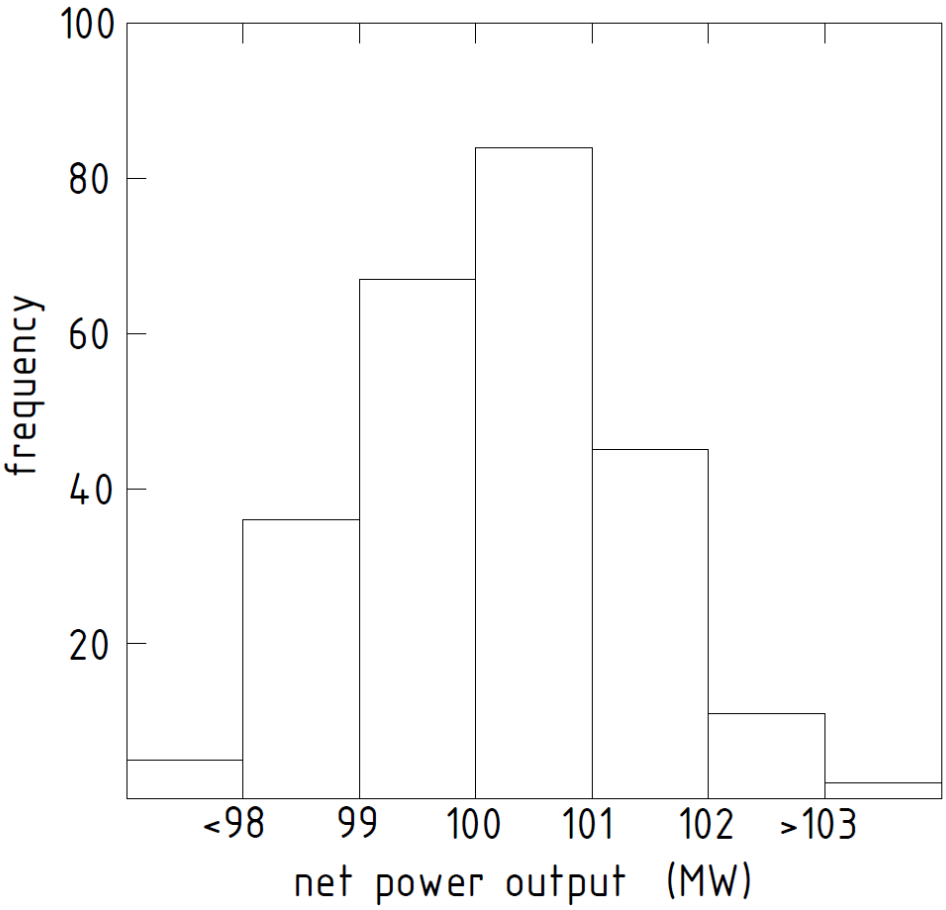

Figure II.11 Net power output distribution for Suez-max plantship with velocity seawater transport in the OTEC system of 2 m/s and heat exchanger is parallel with seawater tanks

Obtaining the histogram graphs for all cases and calculating its mean value, a graph correlating the effect of the sea water transport during the OTEC cycle and location of the heat exchanger to the net power output can be obtained as shown in figure II.12.

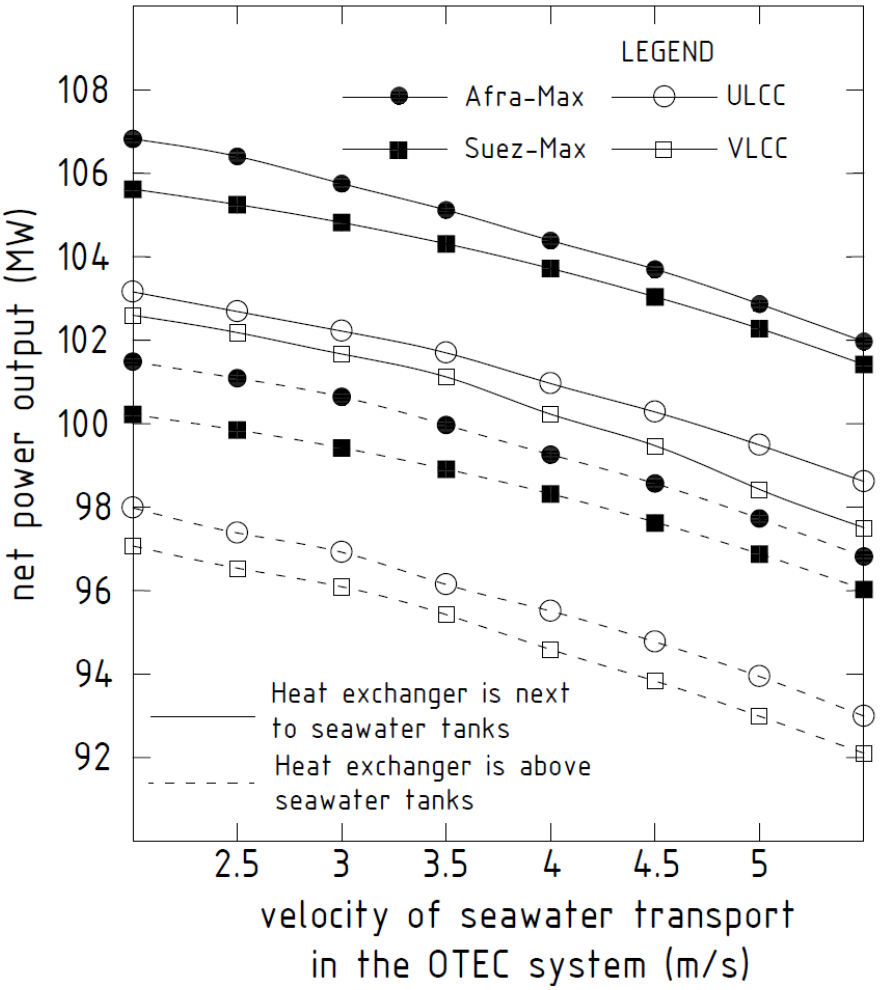

Figure II.12 Result of net power calculation

As shown in figure II.12, the effect of seawater transport velocity in the OTEC system is not relatively significant compared with the effects of the plantship size and the location of heat exchanger. Figure II.12 also indicates that the net power output decreases with increase of seawater transport velocity in the OTEC system. From the figure II.12, it also can be concluded that locating the heat exchanger next to seawater tanks will save around 5-6 MW or around 5% of the net power target. Setting up the targeted net power of 100 MW and locating the heat exchanger parallel with the seawater tanks, Afra-max and Suez-max types of oil tanker ships are still sufficient as the plantship even the seawater

transport velocity during the OTEC cycle is set up to 5 m/s. But locating the heat exchanger above seawater tanks will make Afra-max and Suez-max type suitable as far the velocity of seawater transport in the OTEC system does not exceed 4.5 m/s. For ULCC, the net power output of 100 MW can be achieved if the heat exchanger is located next to seawater tanks with seawater transport during the OTEC cycle below 3.5 m/s. In the case of VLCC, it is clearly pointed that it is not suitable for the plantship. Figure II.13 shows the ratio between the net power output and the gross power output. The graph shows an agreement with the initial assumption that the required pumping power is approximately 30 % of the gross power output.

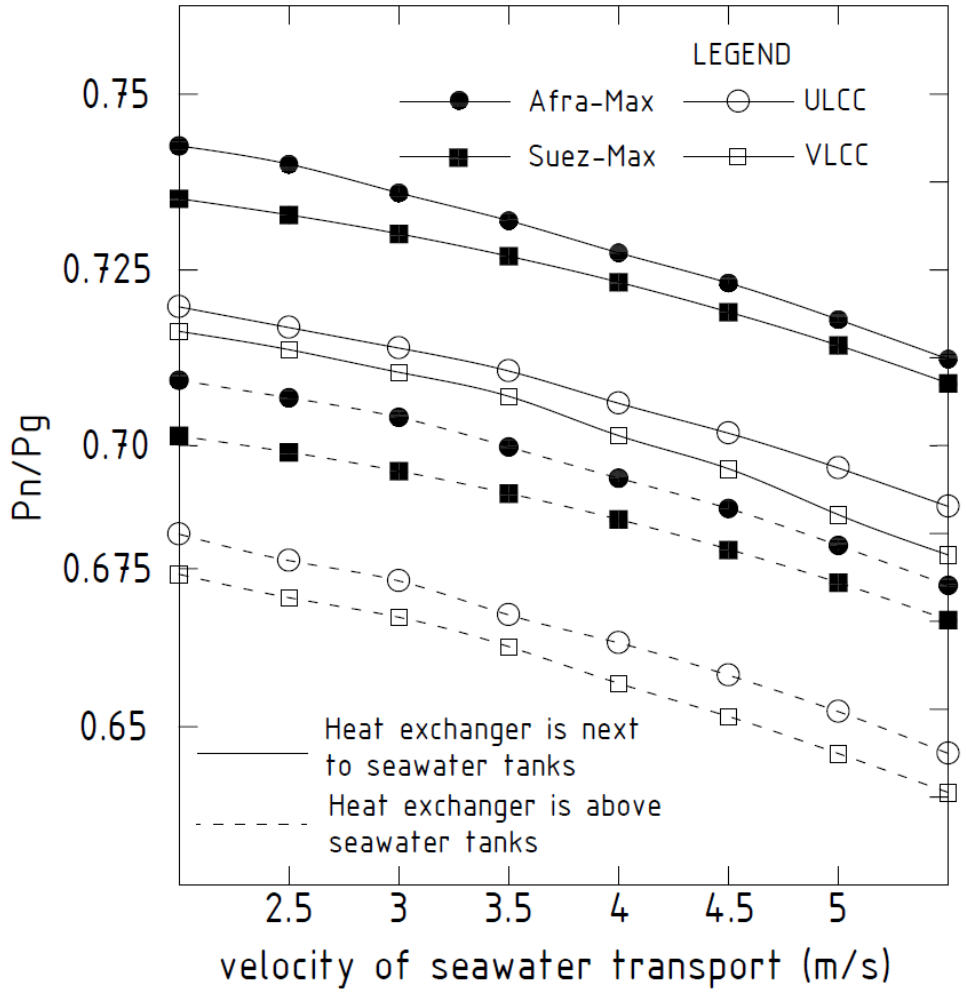

Figure II.13 Ratio of the net power and the gross power

2.6.2 Required size of seawater tanks

The analysis is carried out by varying the height of seawater tank with seawater transport increasing from 1 m/s to 5.5 m/s. The result correlating the velocity of seawater transport and the total pressure acting on the top of the tank for various height of seawater tanks is shown in figure II.14.

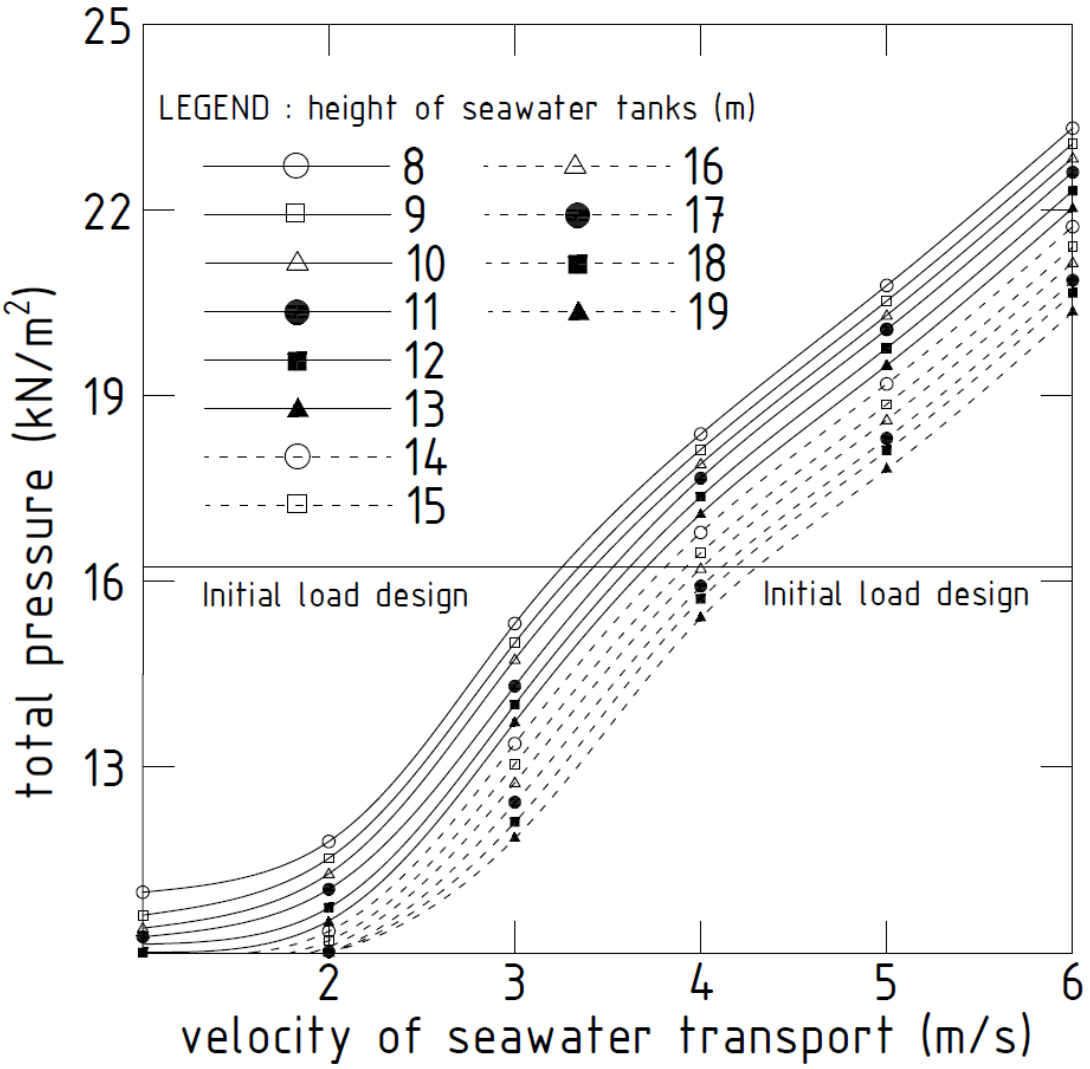

Figure II.14 Total pressure acting on the top part of seawater tank

At the first stage of the analysis, seawater transport velocity of 1 m/s needs excessive size of the risers. This makes the scantling of the riser stated in section 5.3.1 unable to sustain the applied loads. By comparing the total pressure and the initial load design, the minimum height of the seawater tanks at certain level of seawater velocity can be

estimated. In order to naturally push up the deep seawater to the surface, the draft of the plantship must be the same level of the top of seawater tanks. Thus, beside to design the size of seawater tanks, the result from this particular analysis is also used to set the minimum required draft of the plantship. Form figure II.14, it can be clearly known that seawater velocity more than 4 m/s will cause excessive pressure acting on the top part of the tank if the height of seawater tanks is less than 14 m. Hereafter, the seawater transport velocity is focused only from 2 m/s to 4 m/s. The second analysis is to investigate the minimum distance between riser and sidewall of the tanks which then to be the basic consideration to decide the breadth and the length of the seawater tank. Indirectly, the result will also discern the minimum breadth and length of the plantship. Figure II.15 shows the correlation between the distance between riser and sidewall with the dynamic pressure acting on the sidewall of the tank.

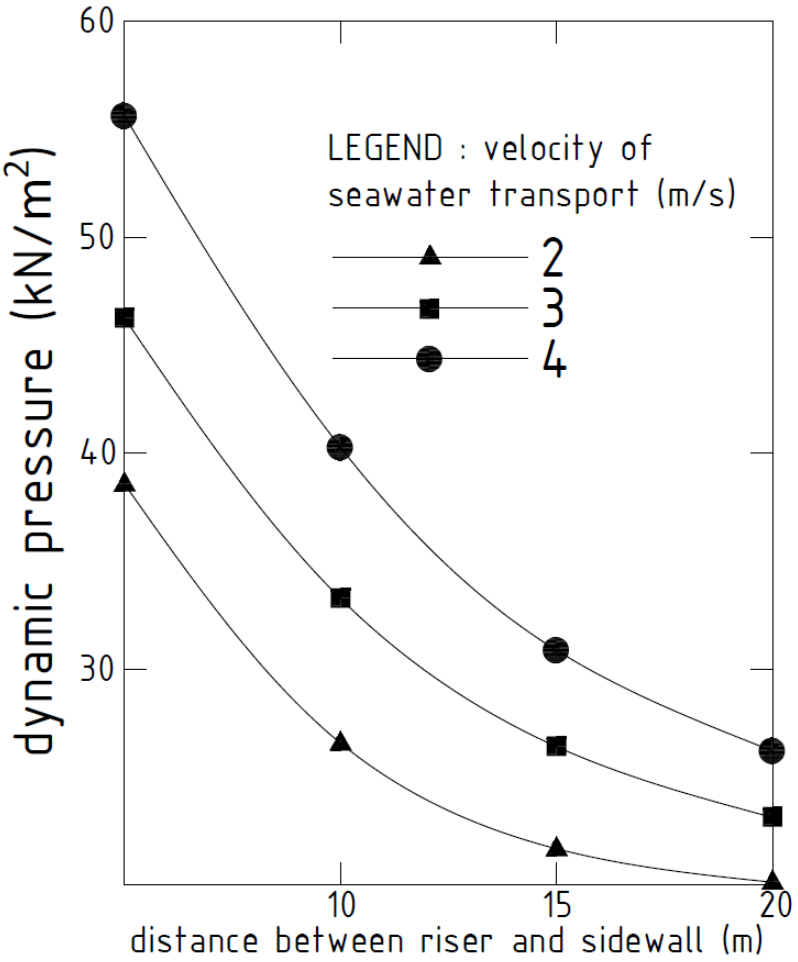

Figure II.15 Total pressure acting on the top part of seawater tank

The total pressure acting on the sidewall is a sum of dynamic pressure in figure II.15 and static pressure which depends on the height of seawater tank. The initial design load for sidewall tank is also affected by the height of seawater tanks but not less than 25 kN/m^2 [II.41]. The static pressure and the initial design load are calculated referring ClassNK regulation [II.41].

2.6.3 Final results

Varying the size of the plantship using Monte Carlo Simulation, sharpening the OTEC system choices using Constraint Satisfaction Method, the final results are obtained as shown in table II.8.

Table II.8 Results from numerical simulation.

Seawater velocity estimation				
1 m/s	The cold water riser size is larger than the design			Failed
2-3 m/s	No problem found			Ok
3-4 m/s	The pressure on the sidewall is larger than the design			Failed
> 4 m/s	The pressure on the top wall is larger than the design			Failed
Plantship decision : heat exchanger is above seawater tanks				
Type	Length of waterline	Breadth	Draft	Conclusion
Afra-max	Failed: the provided length is not enough	Failed: not enough breadth for seawater tanks	Failed: Not enough buoyancy	REJECTED
Suez-max	270-280 m	54-57 m	19-23 m	Ok
	280-295 m	46-52 m	17-20 m	Ok
	295-310 m	45-52 m	16-18 m	Ok
ULCC	Failed: over length	Failed: over length	Failed: over buoyancy	REJECTED
VLCC	Failed: over length	Failed: over length	Failed: over buoyancy	REJECTED
Plantship decision : heat exchanger is next to seawater tanks				
Type	Length of waterline	Breadth	Draft	Conclusion

Afra-max	Failed: the provided length is not enough	Failed: not enough breadth for seawater tanks	Failed: Not enough buoyancy	REJECTED
Suez-max	270-280 m	54-57 m	26-28 m	Ok
	280-295 m	54-57 m	26-27 m	Ok
	295-310 m	54-57 m	26 m	Ok
ULCC	310-320 m	55-60 m	26 m	Ok
VLCC	Failed: over length	Failed: over length	Failed: over buoyancy	REJECTED

From the results, the sufficient velocity of seawater transport is between 2 m/s and 3 m/s. If the velocity of seawater transport is less than 1 m/s, the diameter of cold water pipe will be too large for the top joint connection to sustain the applied load. Considering the constraint due to seawater flow inside seawater tanks, seawater transport velocity of more than 3 m/s requires excessive size of the seawater tanks to keep the acting pressure below the design load.

In the case of plantship decision, if the excessive provided capacity is more than 5% of the required parameter, the plantship will be considered as overdesign. But if the provided capacity is less than the required one, the plantship size will be rejected. It will be recommended if the provided capacity is more than the required one and less than 105% of the required.

The process is divided into two conditions, the first is when the heat exchanger is located above sea water tank and the second is the heat exchange is placed next to seawater tank. In the case one, Afra-max type is rejected because the length, the breadth and buoyancy of the plantship are less than the required ones. On the other hand, ULCC and VLCC are also rejected due to oversize capacity. Suez-max type is the only plantship suits on the criteria with the scantling listed in table II.8. For the case two, Afra-max type is also insufficient because of not enough capacity and VLCC is also unacceptable because the provided scantling was far beyond the required ones. Suez-max type is acceptable for the case two, but compared with the first case, the required breadth of the

plantship is larger. This is because in the case two, the heat exchanger is arranged parallel to the seawater tanks which makes the required breadth of the plantship larger. For the same reason, ULCC type which considered oversize in the case one can be accepted in the case two. The detail scantlings of the possible plantship for case two are also listed in table II.8.

As shown in table II.8, in the case where the heat exchanger is above seawater tanks, the required draft for the OTEC plantship is around 16-20 m. If compared with the original draft listed in table II.1, there is remarkable gap between them. It implies that for the same volumetric space, the required buoyancy for OTEC plantship is lower than oil tanker ship. As the draft per breadth ratio decreases, the stability problem might be triggered. This is one factor to be considered in general arrangement design. In the case two, the heat exchangers are divided into two layers. So the height of seawater tanks at least must be twice than the required height of one submodule. This brings a consequence that the draft must be at least 26 m, which embodies 21 m for seawater tanks and 5 m of riser handling equipment. To submerse the plantship of 26 m, the solid ballast will be installed on board. Additionally, the freeboard allowance should be considered more in this case especially for damaged–ship analysis.

2.7 General Arrangement

The novelty of the general arrangement for OTEC floating structure is the installation of the seawater tanks and suspended pipes for both aspirating and discharging seawater. The inlet pipes are used to deliver the seawater to the floating structure and the inlet seawater tanks are necessary to store the seawater before being distributed to the OTEC system equipment. After utilization, the seawater will be discharged at a substantial depth so the discharged seawater which has lower temperature will not affect the temperature of the warm surface seawater. To spill out the seawater at the certain depth, it is required to install outlet pipes. Following this condition, the outlet seawater tanks are also necessary to collect the seawater from the heat exchanger before being discharged through outlet pipes.

The preliminary design of general arrangement in this section is conceptualized ensuring that it could be designed, installed, and built as commercial platform for OTEC power plant. The general arrangement is drawn for two design conditions, the case one is the arrangement when the heat exchanger is located above the sea water tank and the case two is when the heat exchanger is next to seawater tank. The philosophy of the design is same for both plantship. The difference is just the size of the seawater tank. In the second design, the distance between the risers and sidewall of the tanks is limited by the space for heat exchanger. In this condition, local strengthening system must be installed to resist the deflection happening on the wall plate due to dynamic pressure.

First, the center of buoyancy is estimated and the arrangement is objected so the distance between center of buoyancy and center of gravity does not cause extreme longitudinal trim. The electricity production units are divided into two compartments with pair specifications. There are in front of cold water tank and behind cold water tank. Beneath seawater tank, there is space for riser handling equipment with inner bottom height of 5 m.

The general arrangement for both cases are drawn with the size of the plantship as the mid-value of the obtained results shown in table II.8. The sample design has length of waterline of 285 m, breadth of 50 m, with adjustment draft of 17 m for case one and 26 m for case two. Consideration based on the temperature gradient at the site and required

flowrate of OTEC system implies that a cold water pipe of 800 m long with diameter of 12 m is required to be suspended at around mid-ship. A pair of warm water pipes are also necessary to pump up the warm water surface from 20 m of seawater depth. To avoid the ecological damage on the surface ocean due to temperature mix, a pair of cold water discharge pipe and a pair of warm water discharge pipe are also attached on the keel of the plantship with length of 40 m. The seawater transport velocity for CWP inlet is set to be 2 m/s, but for CWP outlet, WWP inlet, and WWP outlet are set to be 3 m/s. The location of the risers is determined considering the longitudinal stability and dynamic motion of the plantship by placing the risers in proportional distance and placing the cold water pipe at approximately near by the center of gravity. These risers are supported by a ball and socket structure incorporated in the hull which allow to rotate up to 20^{o} about the vertical axis. In the most recent state-of-the-art of riser manufacturing technology, there is still big gap between the estimated size and the practice. Thus, a specific study on the OTEC riser is necessary to be carried out. One of the solution is by examining the possibility of installing multiple risers to deliver the seawater. It can be examined to decrease the diameter of the risers.

Figures II.16- II.19 show general arrangement for case one. Figure II.16 is the side view of the plantship. Figures II.17, II.17, and II.19 are top view at waterline 5 m, 17 m and 26 m respectively. The distance between the second and the third deck is set being about 9 m high to cope the size of the heat exchanger. On the second deck, 36 submodules of condenser and evaporator are placed symmetrically to maintain the stability. The turbine-generator and all pumping system are placed on the third deck. The relative location is intended to minimize the parasitic loss energy as much as possible. However, because the seawater tanks, heat exchanger and the turbine-generator are not parallel each other, it still needs large energy to pump up the seawater from seawater tanks to heat exchanger and working fluid from heat exchanger to turbine-generator.

Placing the heat exchanger parallel with seawater tanks is the best solution to overcome the issue mentioned above. The design process indicates that it is impossible to also set the turbine-generator parallel with the heat-exchanger due to limited space. As the mass density of the working fluid is not relatively large compared with the seawater, the parasitic loss energy due to this condition is extensively acceptable. The arrangements

are shown in figures II.20- II.21. Figure II.20 is the side view of the plantship. Figures II.21 and II.22 are the top view at waterline 5 m and 16 m respectively. For the waterline 26 m, the top view is same with the case one.

For both designs, the hotel, living quarters, office room and other business rooms are located on the superstructure. The fore peak and after peak will be used for plantship control system. In case for the electricity delivery to the shore, marine cable will be used.

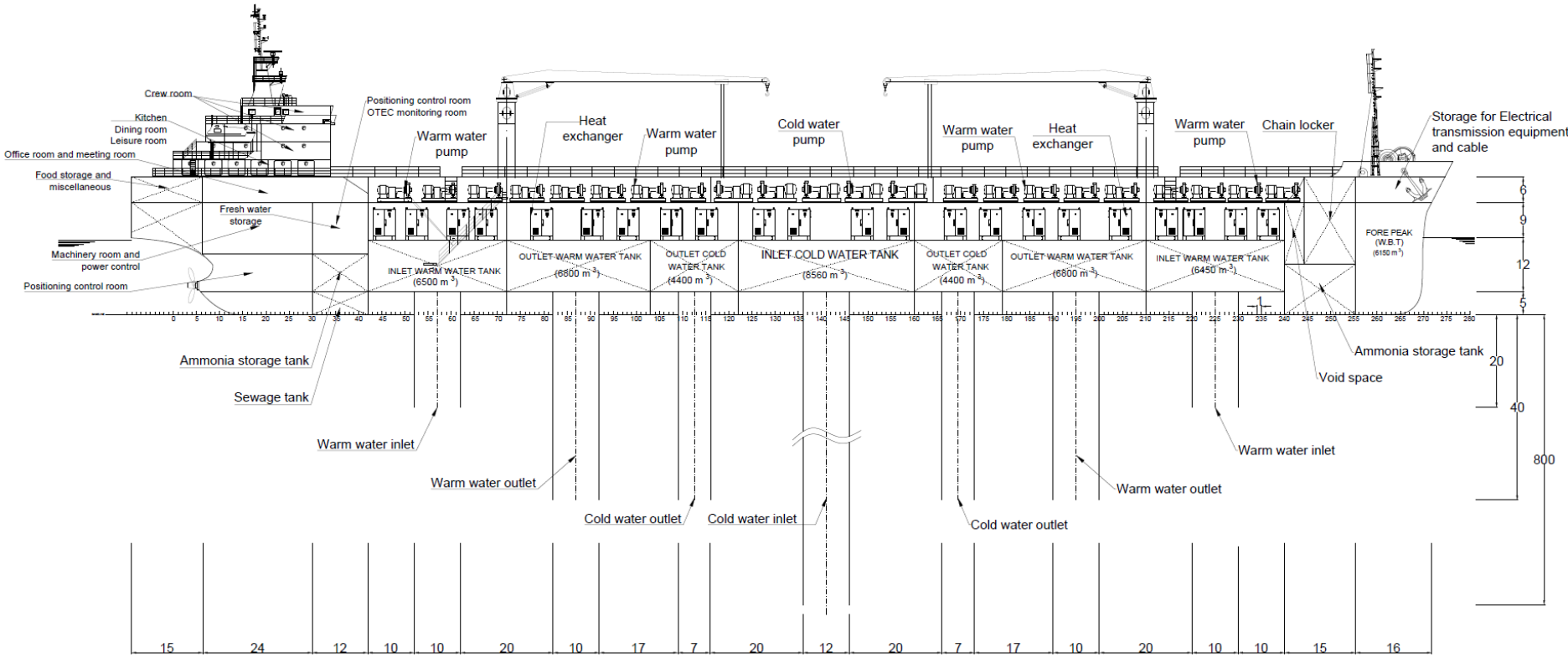

Figure II.16 Side view for case one

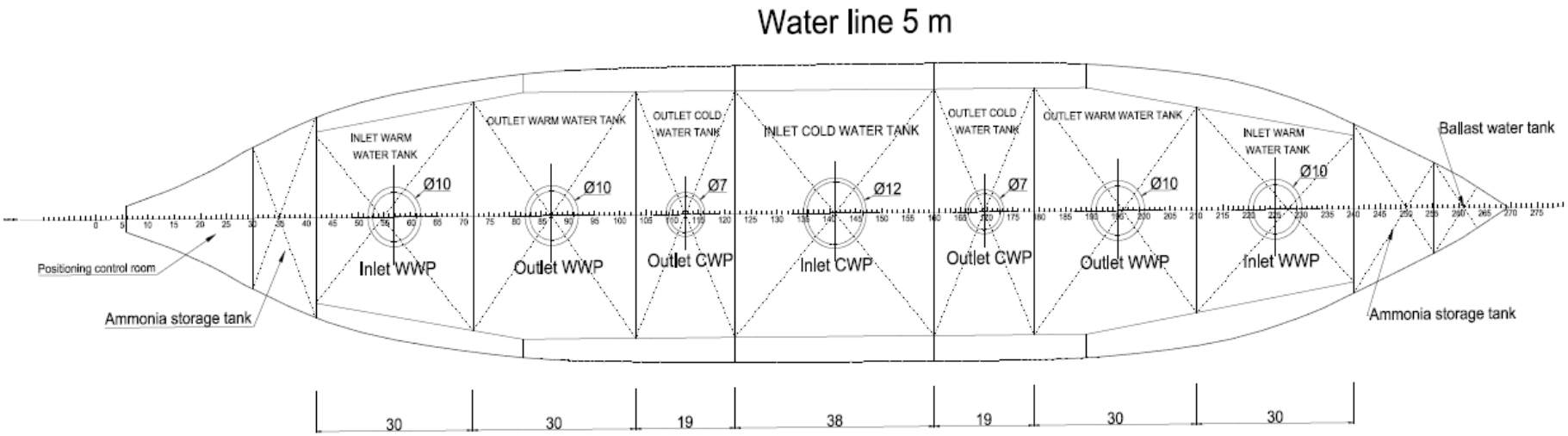

Figure II.17 Top view at waterline of 5 m for case one

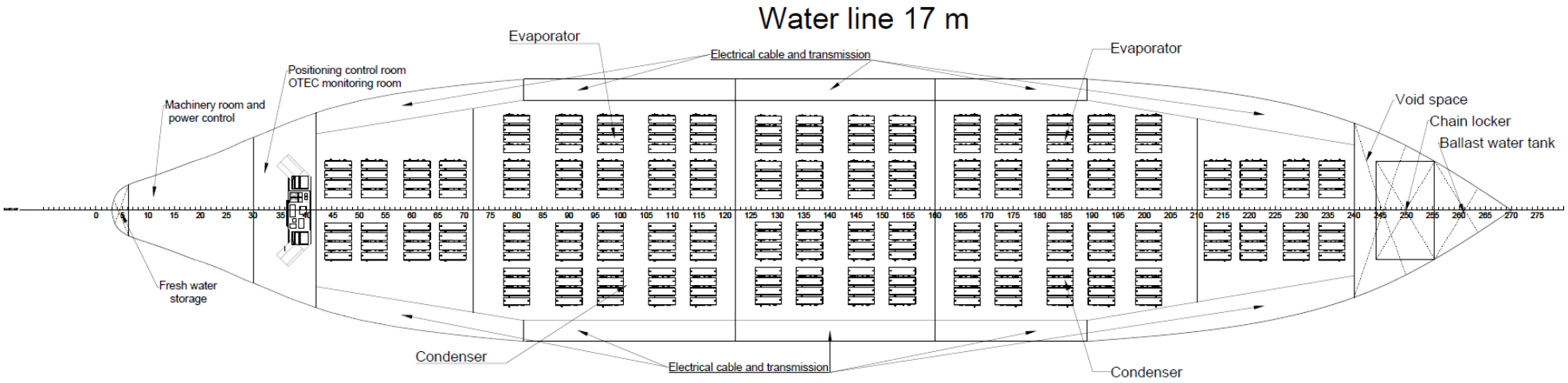

Figure II.18 Top view at waterline of 17 m for case one

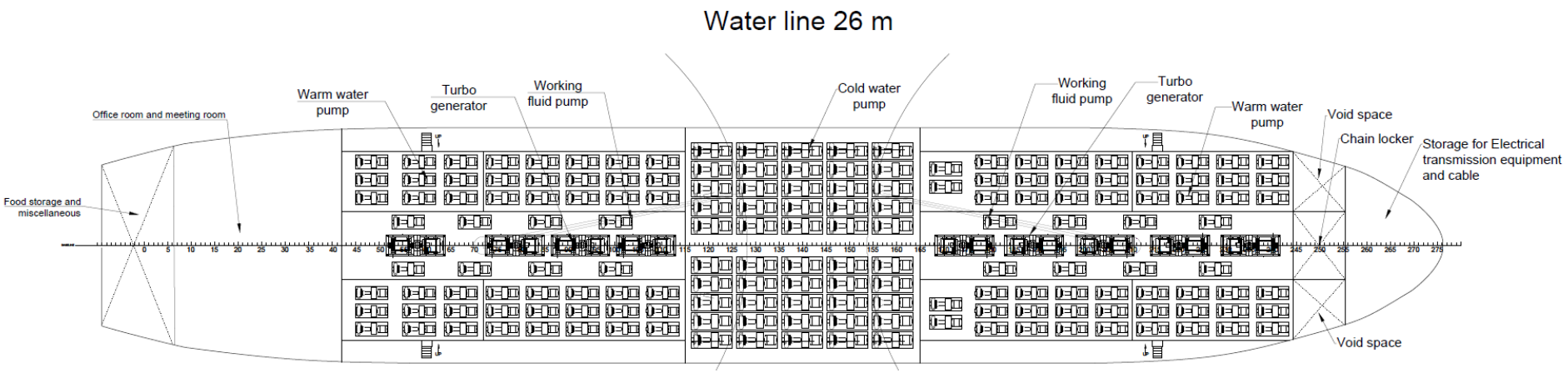

Figure II.19 Top view at waterline of 26 m for case one

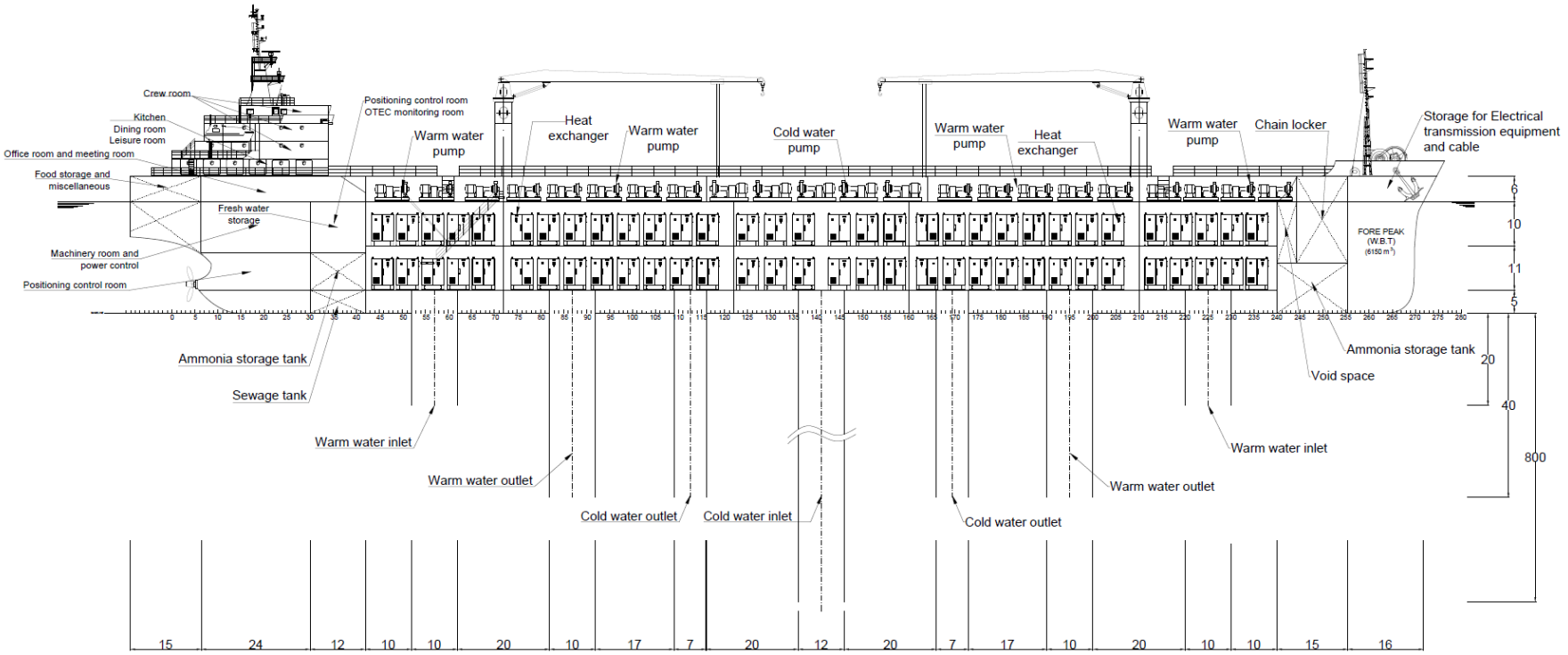

Figure II.20 Side view for case two

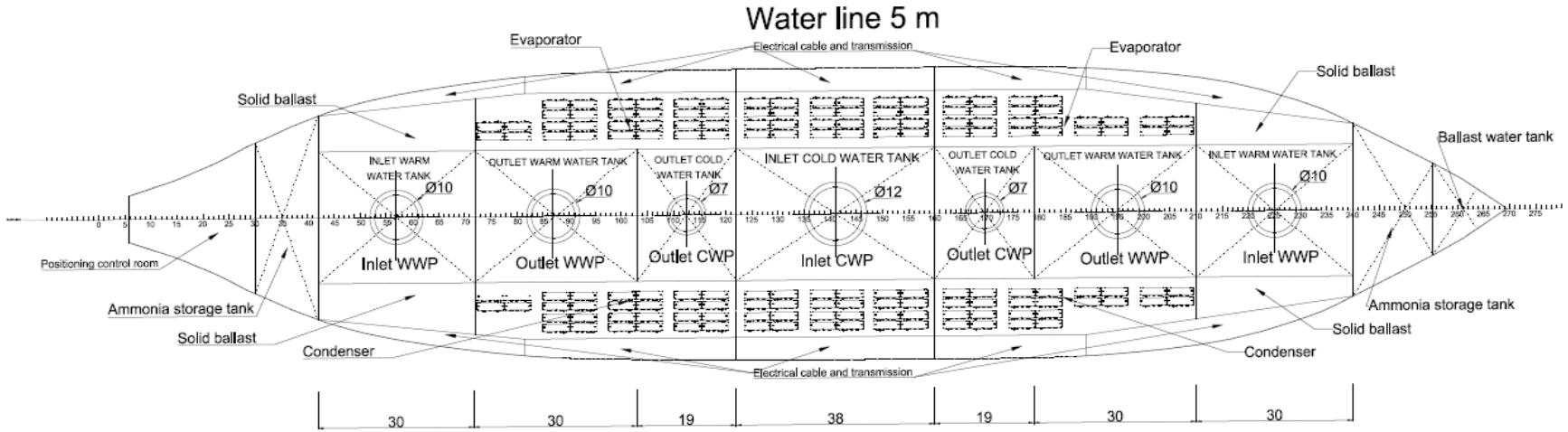

Figure II.21 Top view at waterline of 5 m for case two

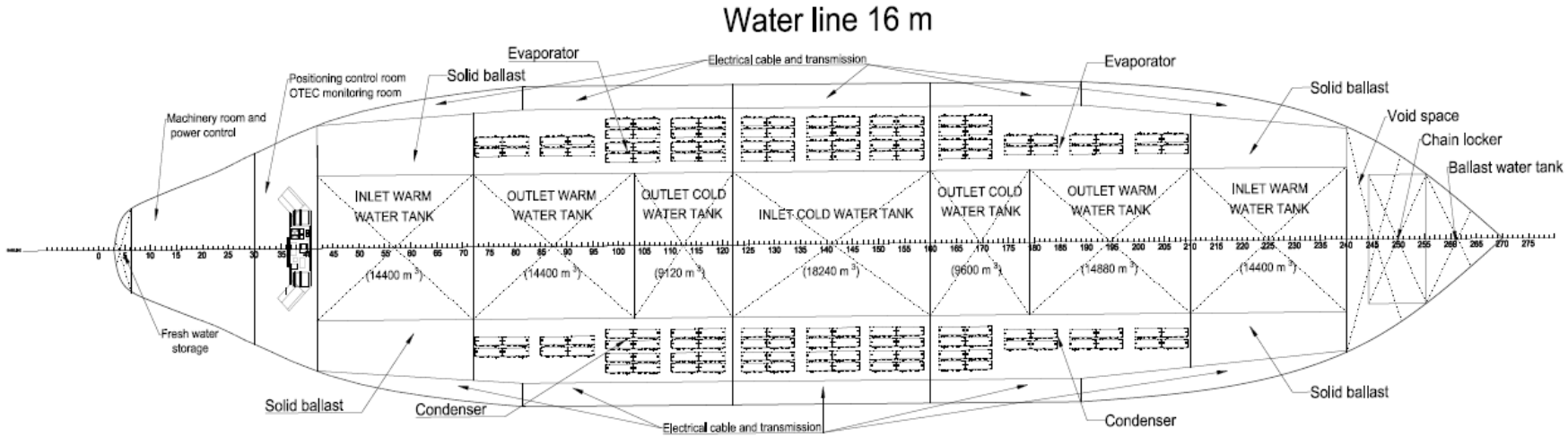

Figure II.22 Top view at waterline of 16 m for case two Top view

2.8 Conclusion

The plantship is considered from oil-tanker ship conversion and is designed to be utilized in Mentawai island, west part of Indonesia. The process of designing 100 MW-net OTEC power plant yields results implying that Suez-max oil tanker type is sufficient to be the plantship. The optimum water transport velocity also has been examined on the basis of recent progress of OTEC system and components. It can be concluded that seawater transport of 2-3 m/s is the optimum velocity.

The placement decision for the heat exchanger is solely hard to be determined. The result shows that placing the heat exchanger above seawater tank will sacrifice about 5-6 % of net power output. For the second case, setting up the heat exchanger parallel to the seawater tanks requires larger size of the plantship and the necessity of deeper draft. Due to this condition, solid ballast might be needed to be installed on board. These will increase the capital cost. The proposed win-win solution might be decreasing the space for seawater tanks so the heat exchanger and seawater tanks can be placed parallel in one layer. By this way, the required size and draft of the plantship will be decreased. However, decreasing the size of the tanks may trigger excessive pressure acting on the sidewall of the tanks. To deal with condition, installing local stiffening system on the tanks could be one solution. The visibility of this solution needs further investigation and will be done in the future.

Additionally, in this paper, converting an oil tanker ship to be used for OTEC floating structure aims to decrease the capital cost. The cost estimation analysis and study comparison between the proposed solution and others will be carried out in the near future.

REFERENCES

[II.1] Syamsuddin ML, Attamimi A, et al (2015) OTEC potential in the Indonesian seas. Energy Procedia 65:215 – 222

[II.2] Uehara H, Ikegami Y (1990) Optimization of a closed-cycle OTEC system. J Sol Energy Eng 112: 247-256

[II.3] Vega LA, Michaelis D (2010) First generation 50 MW OTEC plantship for the production of electricity and desalinated. In: Proceeding of offshore technology conference (OTC 20957). Offshore technology conference, Texas, pp 1-17.

[II.4] Finney KA (2008) Ocean thermal energy conversion. Guelph Engineering Journal 1: 17-23

[II.5] Engels W, Zahibian F (2014) Principle and preliminary calculation of ocean thermal energy conversion. In: Proceeding of American society for engineering education (ASEE 2014). American society for engineering education, Bridgeport, pp.1-5

[II.6] Vega LA (2012) Ocean thermal energy conversion. In: Encyclopedia of sustainability science and technology vol.6, Springer, New York, pp 7296-7328

[II.7] Vega LA (1992) Economics of Ocean Thermal Energy Conversion (OTEC). In: Ocean Energy Recovery: The State of the Art. American Society of Civil Engineers, New York, pp 152-181

[II.8] Vega LA (2003) Ocean thermal energy conversion primer. Mar Technol Soc J 6:25-35

[II.9] Vega, LA (2010) Economics of Ocean Thermal Energy Conversion (OTEC): an update. In: Proceeding of offshore technology conference (OTC 21016). Offshore technology conference, Texas, pp 1-18

[II.10] Lockheed martin mission systems and sensors (2012) Ocean thermal energy conversion life cycle cost assessment (final technical report DE-EE0002663). Lockheed Martin, Maryland

[II.11] International renewable energy agency (2014) Ocean thermal energy conversion: technology brief. IRENA, Abu Dhabi

[II.12] Aldale AM (2017) Ocean thermal energy conversion (OTEC). American Journal of Engineering Research (AJER) 6:164-167

[II.13] Nihous GC, Vega LA (1993) Design of a 100 MW OTEC-hydrogen plantship. MAR STRUCT 6: 207-221

[II.14] Gibbs & cox, Inc. (1978) Ocean thermal energy conversion (OTEC): platform configuration and integration. Gibbs & cox, Inc., Washington

[II.15] Glosten LR (1979) A baseline design of an OTEC pilot plantship. Johns Hopkins university, Maryland

[II.16] Office of ocean minerals and energy (1981) Ocean thermal energy conversion (OTEC): final environmental impact statement. National oceanic and atmospheric administration, Washington

[II.17] Marine board of the commission on engineering and technical system (1983) Ocean engineering for ocean thermal energy conversion. National academic press, Washington

[II.18] George JF, Richards D (1980) Baseline designs of moored and grazing OTEC pilot plants. Johns Hopkins university, Maryland

[II.19] Avery WH, Wu C (1994) Renewable energy from the ocean: a guide to OTEC. Oxford Univ. press, New York.

[II.20] Yee AA (2015) OTEC platform. In: large floating structures: technological advances. Springer, Singapore, pp 261-280

[II.21] Srinivasan NA (2009) New improved ocean thermal energy conversion system with suitable floating vessel design. In: proceeding of international conference on offshore mechanics and arctic engineering (OMAE2009). American society of mechanical engineers, Hawaii, pp 1119-1129.

[II.22] D`Souza RB, Delepine YM, Cordy AR (1994) An approach to the design and selection of a cost effective floating production storage and offloading system. In: Proceeding of offshore technology conference (OTC 7443). Offshore technology conference, Texas, pp 1-14.

[II.23] Paik JK, Thayamballi AK (2007) Overview of ship-shaped offshore installations. In: Ship-shaped offshore installations. Cambridge university press, Cambridge, pp 1-28

[II.24] Bureau Veritas (2018) Classification and certification of ocean thermal energy converter (OTEC). Bureau Veritas, France

[II.25] Brailsford SC, Potts CN, Smith BM (1999) Constraint satisfaction problems: algorithms and applications. Eur J Oper Res 119: 557-581

[II.26] Minning GC (1956) The theory and technique of ship design. The MIT press, U.S.A

[II.27] Parson MG (2004) Parametric design. Society of Naval Architects and Marine Engineers (SNAME), New York

[II.28] Papanikolaou A (2014) Ship design methodologies of preliminary design. Springer, Netherlands

[II.29] TERMPOL surveys and studies (2014) TERMPOL review process report on trans mountain pipeline expansion project. Transport Canada, Canada.

[II.30] Koto J (2017) Potential of 100 KW ocean thermal energy convention in Indonesia. In: Proceeding of the japan society of naval architects and ocean engineers (JASNAOE meeting spring). Tokyo, Japan, pp 763-767

[II.31] Koto J (2016) Potential of ocean thermal energy conversion in Indonesia. International Journal of Environmental Research & Clean Energy 4:1-7

[II.32] Fahmie M, Koto J, Nofrizal, et al (2018) Ocean thermal energy conversion in Layang-Layang and Kuala Baram, Malaysia. International Journal of Environmental Research & Clean Energy 11:12-21

[II.33] Koto.J, Ridho Bela Negara (2017) Potential of 100 kw of ocean thermal energy conversion in Karangkelong, Sulawesi Utara, Indonesia. International Journal of Environmental Research & Clean Energy, 5:1-10

[II.34] Koto J, Tasri A, Kamil I, et al (2017) Sea temperature profiles for ocean thermal energy conversion (OTEC) in Siberut-Mentawai, Sumatera Barat, Indonesia. Journal of subsea and offshore 11: 10-16

[II.35] Susanto RD, Mooree TS, Marra J (2006) Ocean color variability in the Indonesian seas during SeaWiFS era. Geochem Geophy Geosy 7:1-16

[II.36] Nihous GC (2007) A preliminary assessment of ocean thermal energy conversion resources. J Energ Resour-ASME 129:10-17

[II.37] Yong B (2001) Pipelines and riser vol.3. Elsevier Science Ltd., England

[II.38] Panchal CB, Pandolfini PP, et al (2009) Technical report No. ANL/ESD/09-6 ocean thermal plantships for production of ammonia as the hydrogen carrier. Energy systems division Argonne National Laboratory, Chicago.

[II.39] Torishima pump inc. (2018) CDM pump catalogue. Torishima pump inc., Japan

[II.40] Cheremisinoff NP (1995) Fiberglass reinforced plastic: manufacturing techniques and applications. Noyes Publications, U.S.A

[II.41] ClassNK (2017) Rules for the survey and construction of steel ships 2017. ClassNK, Japan

[II.42] Bauchau O, Craig J (2009) Structural analysis. Springer, USA

[II.43] ANSYS inc. (2017) ANSYS software version 17, ANSYS HELP. ANSYS inc., USA

[II.44] ANSYS inc. (2017) ANSYS software version 17, ANSYS CFX HELP. ANSYS inc., USA

[II.45] Idel`chik I (1960) Handbook of hydraulic resistance, National technical information service, USA

[II.46] Watson DGM (2002) Practical ship design. Elsevier Science Ltd., England

[II.47] Schneekluth H (1998) Ship design for efficiency and economy. Elsevier Science Ltd., England

CHAPTER III
DESIGN OF COLD-WATER PIPE (CWP) BASED ON STABILITY APPROACH

3.1 Introduction

Ocean Thermal Energy Conversion is a process of harvesting energy from the ocean by utilizing the temperature difference between surface warm water and deep cold water [III.1,2]. The heat from surface warm water is used to transform the working fluid from liquid into gas form. To maintain the cycle, the cold water is required to retransform the working fluid back to the liquid form after being used to drive the turbine generator [III.1]. From the OTEC feasibility study, the temperature difference between surface warm water and deep cold water must be at least 20^{o}C in order to reach the minimum required efficiency [III.2].

Preliminary studies on the design of a 100 MW-net OTEC power plant which previously carried out in chapter 2 resulted a baseline design of the floating structure from oil tanker ship conversion as shown in figure III.1.

In general, the main novelty of the OTEC floating structure compared with the other utilizations is the installation of a suspended pipe transporting deep cold seawater (Cold Water Pipe; CWP) onto the floating structure [III.3- III.7]. To produce 100 MW-net electricity, the CWP must be lengthened to reach 800 m depth with an inner diameter of 12 m. As the water comes from the bottom part of the pipe, the pipe must be installed in free hanging configuration. This condition causes the top joint conection the only supporting point to support the integrity of the pipe from the applied stress. Another challenge is the effect of the self excitation due to internal flow to the stability of the riser. Additionally, the cost estimation study for OTEC development states that the cost to build the CWP is appoximately 15-20 % of the total capital cost [III.7].

The important role of OTEC CWP to the success of OTEC installation and operation is undeniable by the fact that numerous OTEC projects failed and then abandoned due to CWP problems such as Rio de Janeiro OTEC project in 1935 and even India OTEC project in 2003 [III.4]. Until now, the immature design and unsettled technology of the CWP is one of main reasons why OTEC development still gets stuck in the pilot project [III.4].

Literature survey on the CWP design for commercial scale OTEC power plant results very limited resources which mostly done by Nihous and Vega [III.3], and Lockheed Martin [III.4, III.5]. An attempt to propose the concept of CWP for 100 MW-net OTEC power plant was done by Nihous and Vega in 1993 [III.3]. They conceptualized the CWP with diamater of 10 m from fiber reinforced plastic considering the axial strain and the top joint stress. Far after Nihous and Vega, Lockheed Martin gave additional consideration to design the CWP by including the external effects such us external pressure, platform rotation, etc [III.4, III.5].

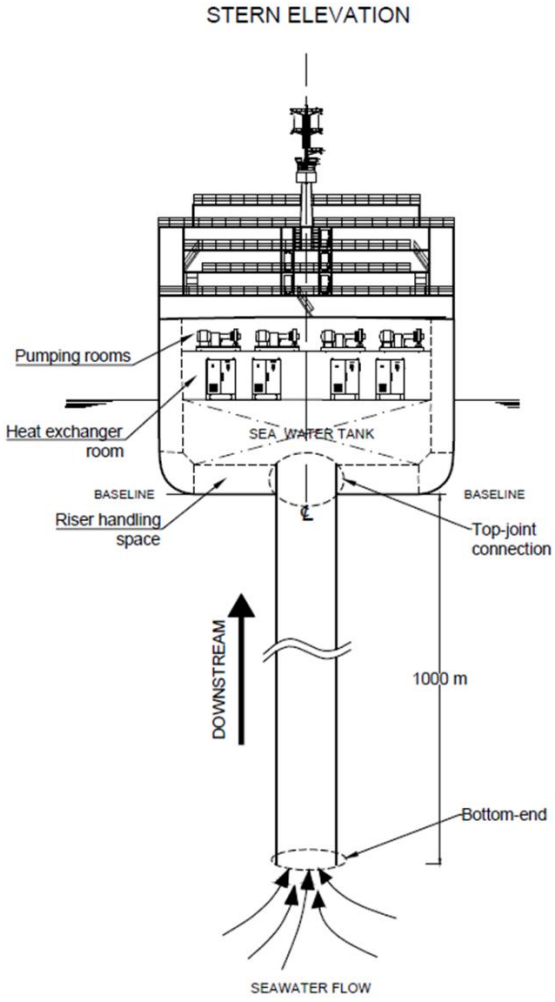

Figure III.1 Sketch of the plantship.

However, researches on the pipe aspirating fluid have analytically, numerically and experimentally proven that the internal flow could also trigger instability of the pipe [III.8- III.14]. Taking into account the significant effect of internal flow to the dynamic motion of the CWP which has not been considered in the existing published studies, the design analysis in this paper focuses on the effect of the internal flow in the term of the critical seawater transport velocity and the applied stress. As efforts to increase the integrity and ensure the survivability of the CWP, this paper also examines the feasible supporting system at the top joint connection and at the bottom-end of the pipe.

Literally, the CWP can be described as a submerged free hanging pipe conveying seawater subjected to the top stress and axial strain. The study on critical velocity assessment of free hanging riser conveying fluid has been done by many researchers in

these last decades. The works mainly refer, extend and develop the comprehensive theory by Païdoussis and Issid [III.8] for various pipe configurations, boundary conditions and applied loads. As the aim of this study is to design a pipe conveying seawater for OTEC utilization, the review will be highlighted and focused on the works which have significant correlation to portray the dynamic behavior of OTEC CWP. More detail record progress of the works on pipe conveying fluid can be found from the introduction of corresponded published papers such as in [III.9- III.11].

The numerical simulation of free hanging riser conveying fluid was carried out by Giacobbi et al. in 2008 [III.9]. In 2010, Giacobbi enhanced the methodology to more clearly duplicate the real condition of pipe conveying fluid characteristic [III.10]. Then, in 2012, Giacobbi et al. reused the simulation process in [III.10] to analyze a riser discharging and aspirating fluid and compare the results with experimental and analytical results [III.11]. In [III.9- III.11], the effect of added mass and drag coefficient which are dominant in the submerged pipe conveying fluid was disregarded. Although the used analytical solution cannot cover the dynamic components of OTEC CWP, it gives an overview how to undergo the numerical simulation and how to compare the results of numerical and analytical solutions using bifurcation curves.

In 2005, Kuiper and Metrikine specifically investigated the effect of the drag coefficient and its contribution to the stability of a submerged pipe conveying fluid [III.12]. Even though the initial intention is to question Païdoussis and Issid`s statement which valuing the effect of inlet depressurization as the reason why flutter does not take place in small velocity, the built equation also adroitly captures how to model the effect of the ambient fluid to the dynamic motion in convenient way.

In the case of boundary condition modelling, to observe its effects to the dynamic behavior of a simple fluid-conveying pipe model, Liang et al. proposed a methodology which is able to incorporate the differential quadrature method and inverse Laplace transform [III.14]. The analysis was done by varying the boundary conditions at the end edges of the pipe and resulting a conclusion that the dynamic behavior firmly depends on the boundary conditions at the both ends.

In this paper, the process of the numerical simulation from the former researches [III.9- III.11] is adapted and then modified to vary the boundary conditions at the top- and bottom-ends of the pipe. Then the general analytical model proposed by Kuiper and Metrikine [III.12] is modified by taking into account the hysteretic damping to the dynamic motion components. The added mass and adapted drag coefficient which are assumed in [III.12] will be determined using numerical analysis for the conditions with and without clump weight. To obtain the general solution, the boundary conditions are varied by adapting the boundary condition modelling as used in [III.12, III.13]. In order to verify the analytical solution, the comparison method used in [III.11] will be employed. Finally, the verified analytical solution will be used to design the CWP in full-scale models. As additional results, the vibration frequency is also investigated here. Even though in this study the vibration frequency will not be directly used to determine the acceptance of the particular cases, it will be used to predict the fatigue life of the CWP for the future work.

3.2 Case Configurations and Methods

Based on the sketch of CWP as shown in figure III.1, the CWP can be modelled as a top-tensioned, submerged, seawater-aspirating pipe subjected to the axial stress due to self-weight and bending stress due to dynamic motion. To be delivered from the subsurface to the floating structure, the seawater comes through an inlet point at the bottom-end of the pipe. As the bottom-end cannot be attached to the seabed, there is no supporting system at the bottom-end to reinforce the riser. The term `top-tensioned` is associated with this free bottom-end condition which makes the stress concentrated at the top-end joint connection between the pipe and the floating structure.

The term `submerged` brings an implication that during its dynamic motion, the surrounding fluid, in this case also seawater, will give reaction opposite to the direction of the motion. This reaction is well-known as hydrodynamic added mass and drag force. During the motion, as the pipe displaces, the bending stress will occur. The stress is sum up of the axial stress due to self-weight and the bending stress due to the dynamic motion.

The scantlings and material properties of the full scale CWP are assumed as shown in table III.1. The length and the inner diameter for all pipes are same. But for the thickness, its value is estimated based on the required flexural rigidity of CWP which assessed by Nihous and Vega [III.3]. Considering the pipe materials, the models are respectively named as pipe A, pipe B, and pipe C. Due to limited computational capability, it is impossible to carry out the numerical simulation using full scale models. Thus, the numerical simulation models are defined by scaling down the real CWP size with factor of 0.1, 0.2, 0.3 and 0.4. The model scantlings are varied incrementally to investigate how the dynamic behavior changes due to the change of the pipe sizes and then the results are used to predict the hydrodynamic coefficients of the full scale models. For convenience, here onward, the simulation models are named with two initial characters as `XY`. `X` is an alphabet referring the type of the material and `Y` is a number pointing the scale factor as 0.Y. For instance, pipe A3 means a pipe with material properties of pipe A and the scantlings which are calculated by scaling down the real size of the CWP with scale factor 0.3, that is, pipe with the length of 300 m, the inner diameter of 3.6 m and the thickness of 1.8 cm.

Table III.1 Material properties and main scantlings of CWP in full scale.

Properties		Pipe A	Pipe B	Pipe C
Material	unit	Steel	Aluminum	FRP
Inner diameter	(m)	12	12	12
Thickness	(cm)	6	10	16
Section area	(m^2)	2.27	3.78	6.03
Length	(m)	1000	1000	1000
Young`s modulus	(MPa)	205000	72000	13776
Yield stress	(MPa)	350	240	550
Dry weight	(N/m)	173247	100116	71854
Wet weight	(N/m)	150481	62109	9407
Total weight	(N)	$150.5x10^6$	$62x10^6$	$9.41x10^6$
Hysteretic damping loss factor [III.14- III.17]		$1.5\ x10^{-3}$	$1x10^{-4}$	$1.6x10^{-2}$

The supporting system at the top joint connection is investigated thoroughly by examining possible solutions including fixed joint, pinned joint and flexural joint with varied stiffness values. At the bottom configuration, the cases will be built with and without considering clump weight installation. The sketches of the case configuration due to variation of the supporting systems are listed in figure III.2 and will be explained in detail in section 3.4.2.

First, the numerical simulation is carried out for models with scale factor 0.1, 0.2 and 0.3. The results are added mass coefficient, adapted drag coefficient, and the motion

amplitude. Considering the results, the sensitivity of motion amplitude on the variables can be assessed. Using the value of added mass and adapted drag coefficient of models with scale factor 0.1, 0.2 and 0.3, the added mass and adapted drag coefficient of models with scale factor 0.4 can be forecasted. Inputting these values to the analytical simulation, the critical velocity of models with scale factor 0.4 can be determined. Separately, the numerical simulation analysis is also done for models with scale factor 0.4. Comparing the results from analytical and numerical simulation, the acceptance of analytical model can be concluded. After being verified, the analytical solution is used for the full scale models.

The term analytical solution here refers a specific definition or can be broadly described as `semi-analytical` as in the process, MATLAB is used as a helping tool. In case of the numerical simulation, Ansys interface softwares are employed to undergo the fluid structure simulation.

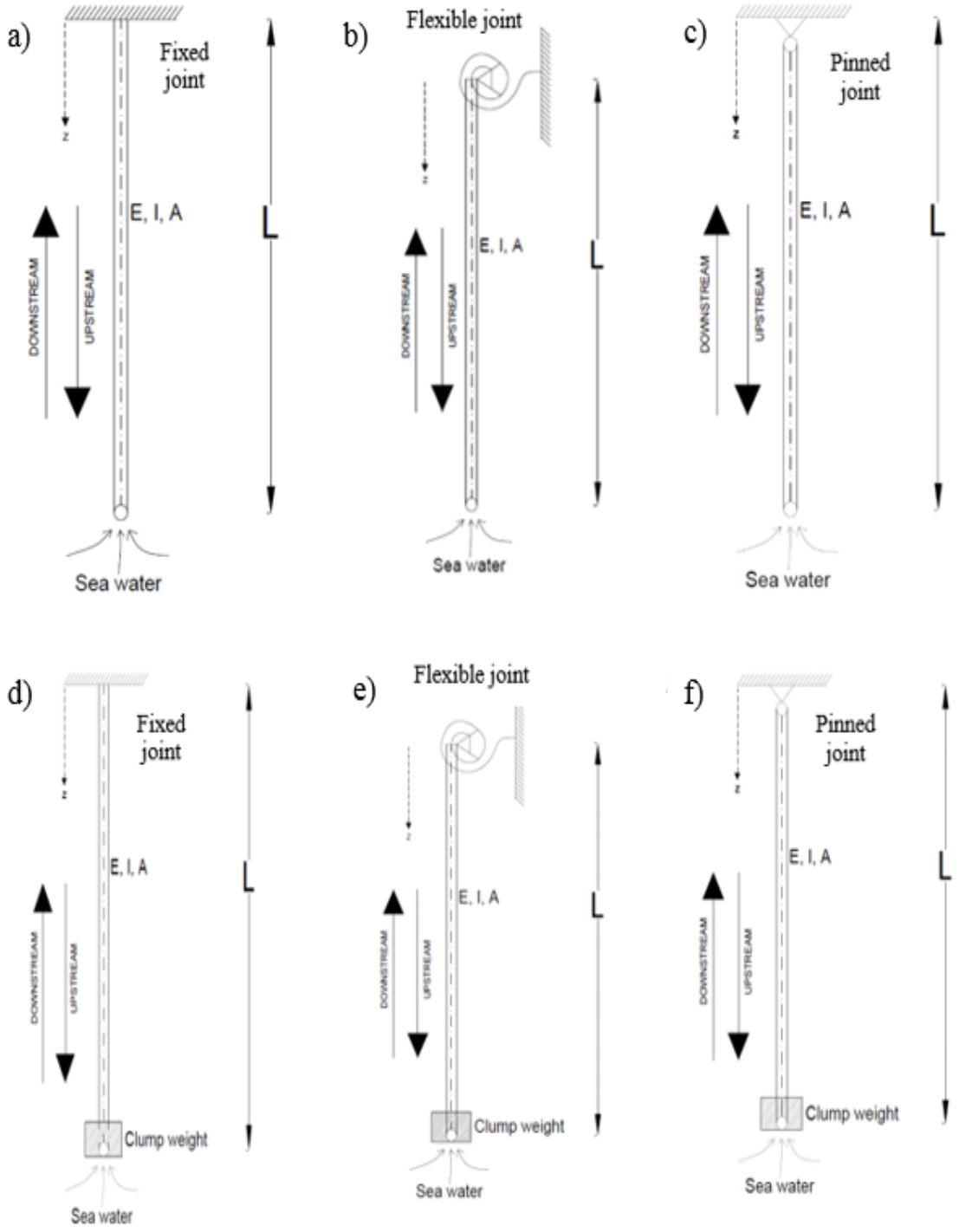

Figure III.2 Sketch of the supporting systems. a) fixed-free; b) flexible-free; c) pinned-free; d) fixed-free with clump weight; e) flexible-free with clump weight; f) pinned-free with clump weight.

3.3 Numerical simulations

The main aims of the numerical simulations are to obtain the values of the added mass coefficient, adapted drag coefficient, stress at top-end connection, vibration frequency and the vibration amplitude at the bottom-end of the pipe through mode shape observation. The values of the added mass coefficient and adapted drag coefficient will be used as input data for the analytical simulation. The values of the maximum stress, vibration frequency and the vibration amplitude are intended to verify the feasibility of the analytical solution.

3.3.1 Numerical simulation procedures

The challenges in the numerical simulation for OTEC CWP application is mainly due to the large size of the analyzed models. Even after being scaled down with scale factor 0.1, the length of the pipe is 100 m, together with the fluid domain, the size of the numerical model will be 125 m length. At this point, the efforts put on this numerical simulation are not merely to obtain the designated results but also how to minimize the computational efforts and the consumed time.

Numerical simulation here is done by combining together the structural analysis software and computational fluid dynamics software or commonly known as fluid-structure interaction (FSI) analysis. In order to ease the pipe model validation, the decoupled analysis is firstly carried out in the Computational Structural Mechanics (CSM). Without considering any applied loads nor any excitations, the mechanical characteristics of the pipe can be computed and the results can be straightforwardly compared with the results from settled theories. After ensuring the acceptance of the pipe model, the FSI analysis procedure can be started. The step by step procedure is extended in the following explanations.

Firstly, as a physical profile, for each model, a pair of pipe and fluid domain are created. Fluid domain is geometry which surrounds the solid pipe including the geometry inside and outside of the pipe. The contact surface between the pipe and the fluid domain is then later set as FSI interface. During definition process of the pipe, the fluid domain is set to be in a frozen mode. To simplify the simulation procedure, the origin point is

located at the center of the outlet area and symmetry condition is imposed along YZ-plane for all analysis step. The detailed geometry and the meshing model are shown in figure III.3.

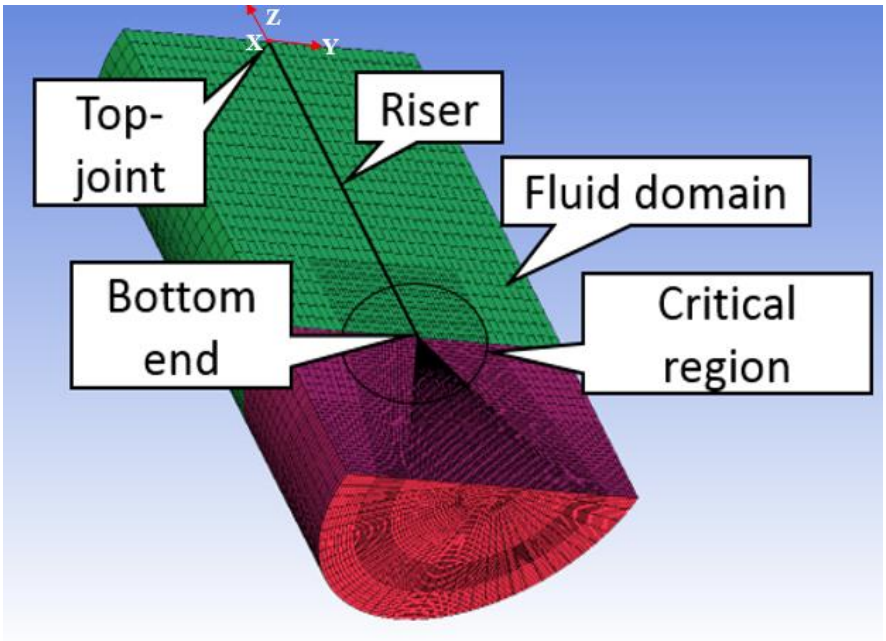

Figure III.3 Geometry and mesh modelling.

The next is the meshing step. This step will significantly influence the simulation results. No matter how advanced the simulation setting, without proper meshing procedure and representative convergence meshing size, satisfying results cannot be obtained. As the geometry of the solid pipe is very simple, its meshing process can be directly produced by using Ansys meshing provided by Ansys interface. But for the fluid domain, the meshing is done using stronger meshing software named ICEM CFD^{TM}. To reduce the computational efforts without any disturbance in the simulation process, the critical regions such as the bottom-end of the pipe and fluid domain around the FSI surface are meshed in fine meshing condition and other parts are left in rough meshes. Later in the analysis process, meshing elements of the solid pipe will be considered as finite elements and the meshing elements of the fluid domain will be treated as finite volumes. In order to conduct the fully-coupled FSI simulation, the mesh setting for both solid pipe and fluid domain must be set to allow mesh deformation.

Separately from the fully-coupled analysis, the next particular step is intended to validate the solid model via ANSYS structural simulation specifically using Modal

analysis. From this analysis, the modal frequencies and mode shapes of the system can be assessed. After being compared with the settled related theories, the model will then be used for fully-coupled analysis using Transient Structural. The Transient Structural analysis allows the system to be investigated in a function of time. This analysis is relatively complex with many requirements to be undertaken including the time-step input, the physical damping and convergence criteria. The detailed explanation about this procedure can be found in [III.10].

Stepping up from the mechanical analysis, the next step is set-up for fluid dynamic analysis using CFX-Pre which is also available in ANSYS Interface. All works correlated with fluid properties are done here. In this step, the boundary conditions of all surface on the fluid domain are defined. The details are numbered in figure III.4 and listed in table III.2.

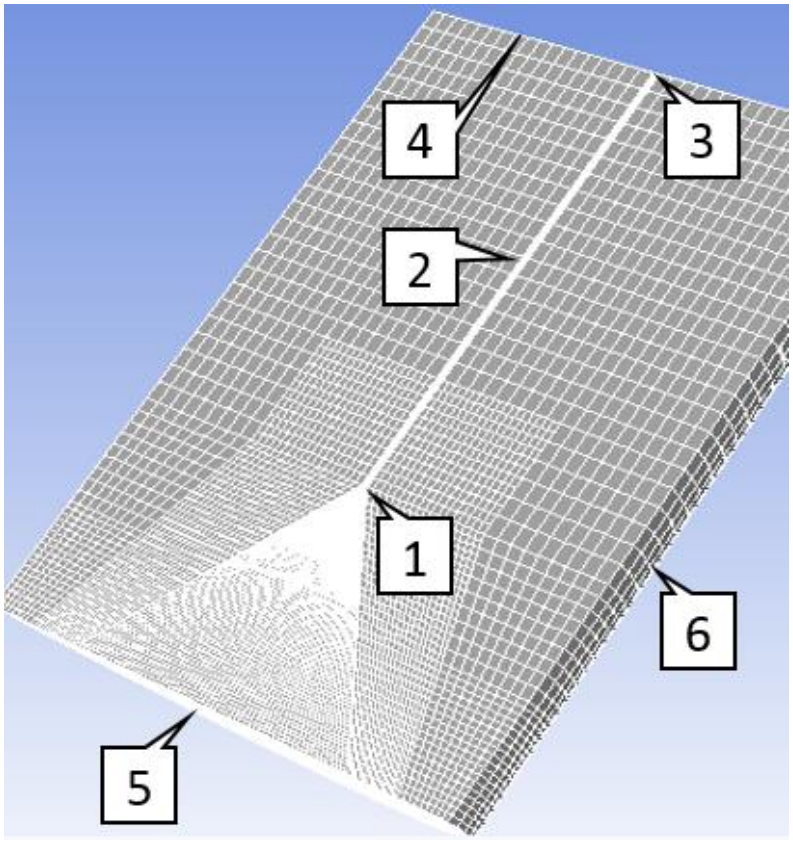

Figure III.4 Boundary conditions numbering.

Table III.2 Material properties and main scantlings of CWP in full scale.

Location	Structure		Fluid	
	Boundary condition	Motion	Boundary condition	Motion
Bottom-end (1)	FSI interface	Fluid-dependent	Inlet	Received from structure
Inner/outer pipe (2)	FSI interface	Fluid-dependent	FSI interface	Received from structure
Top-end (3)	Fixed, Pinned, Flexible	Based on cases	Outlet	Based on cases
Tank cover (4)			Rigid wall	Fixed
Tank surroundings (5 and 6)			Opening	Flow passes in

At the top surface of the solid pipe, the boundary condition is imposed in either fixed, flexible or pinned joint. On the other parts of the pipe (bottom cross section surface, inner and outer walls), the surfaces are defined as FSI interface between solid pipe and the fluid domain. It is also important to be noted that for cases where the pipe is equipped with a clump weight at the bottom-end, the clump structure is treated as part of the pipe. Thus, in this case, at the bottom part of the pipe where the clump weight exists, the outer wall refers to the outer surface of the clump weight instead of the outer pipe wall. For the boundary conditions of the fluid domain, there are several important definitions to set the simulation. All surfaces of the model must be defined based on the desired condition. The top-end of the fluid inside the pipe is defined as an `Outlet`. `Outlet` is a boundary condition which allows the fluid to flow out of the surface. The opposite is the `Inlet` which is set at the bottom-end of the fluid inside the pipe. To model the keel of the floating structure, the top-end of the fluid outside the pipe (tank cover) is defined as a `Wall`. A `Wall` is intended to duplicate the condition where the surface behaves rigid, no

deformation takes places. Finally, the surrounding tank walls are set as an `Opening` to imitate the open water condition of the sea. `Opening` is a type of boundary condition to allow the fluid pass in or pass out to the system depending on the pressure inside and outside of the wall. To model the internal flow, the $k-\varepsilon$ model is imposed as the turbulence modelling which is recommended to obtain high accuracy simulation [III.18].

3.3.2 Numerical simulation results

Numerical simulation is done for pipes A1-3, B1-3 and C1-3 in various boundary conditions as mentioned in section 3.2. In this particular section, the discussion will be focused only for pipes A and C. Pipe A represents high-density material and pipe C is the representative of low-density material.

To calculate the added mass coefficient, a simplified formula proposed by Cimbala is used [III.19, III.20]. This method assesses the added mass by considering the kinetic energy change of the ambient fluid due to change of the pipe`s vibration velocity. Mathematically, the equation can be written down as

$$m_{added} = \frac{2(EK_2 - EK_1)}{V_2^2 - V_1^2} \tag{III.1}$$

EK_1 is the kinetic energy of the surrounding fluid at pipe`s movement speed V_1. While the velocity of seawater transport increases, the pipe vibrates at velocity V_2 and the kinetic energy become EK_2. Using equation III.1, the added mass can be obtained and then divided with the displaced fluid mass to calculate the added mass coefficient.

To figure out which parameters affect the added mass coefficient at most, figures III.5- III.7 are plotted as sample results for particular cases. Figure III.5 shows the effect of the material properties to the added mass coefficient in incremental increase of seawater transport velocity. In figure III.5, the boundary condition is set as fixed at the top with clumped weight at the bottom-end. Figure III.6 shows how the added mass behaves due to clump weight installation observed using pipe C and fixed joint at the top-end. Figure III.7 shows the effect of scale factor and top joint conditions to the added mass coefficient under clump weight installation on pipe A. From figures III.5- III.6, it can be predicted that the added mass is mostly influenced by the material properties,

clump weight installation and seawater transport velocities. In case of scale factor and top joint connection, as shown in Figure III.7, their effect is relatively small.

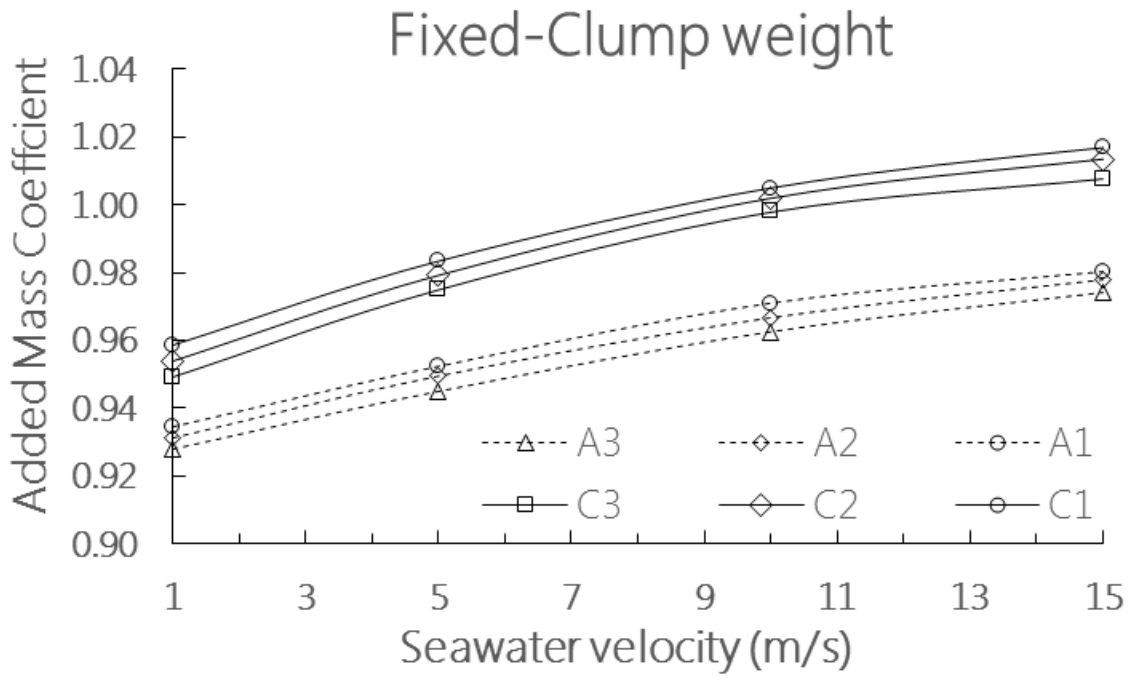

Figure III.5 Effect of material and seawater velocity to the added mass coefficient.

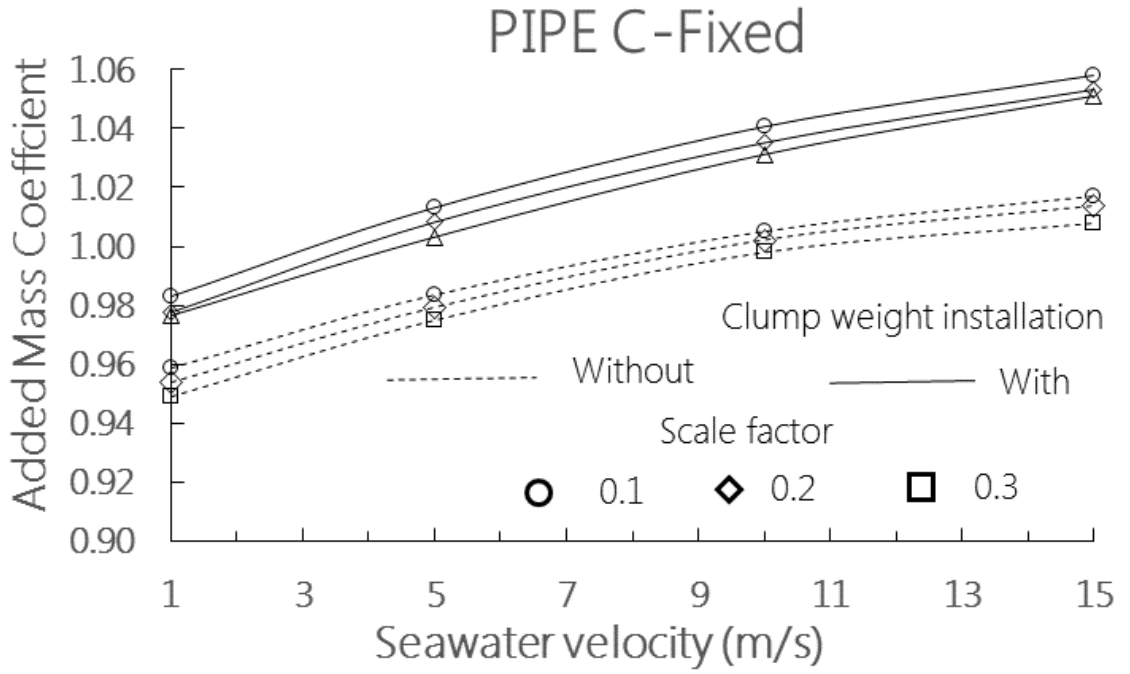

Figure III.6 Effect of clump weight installation to the added mass coefficient.

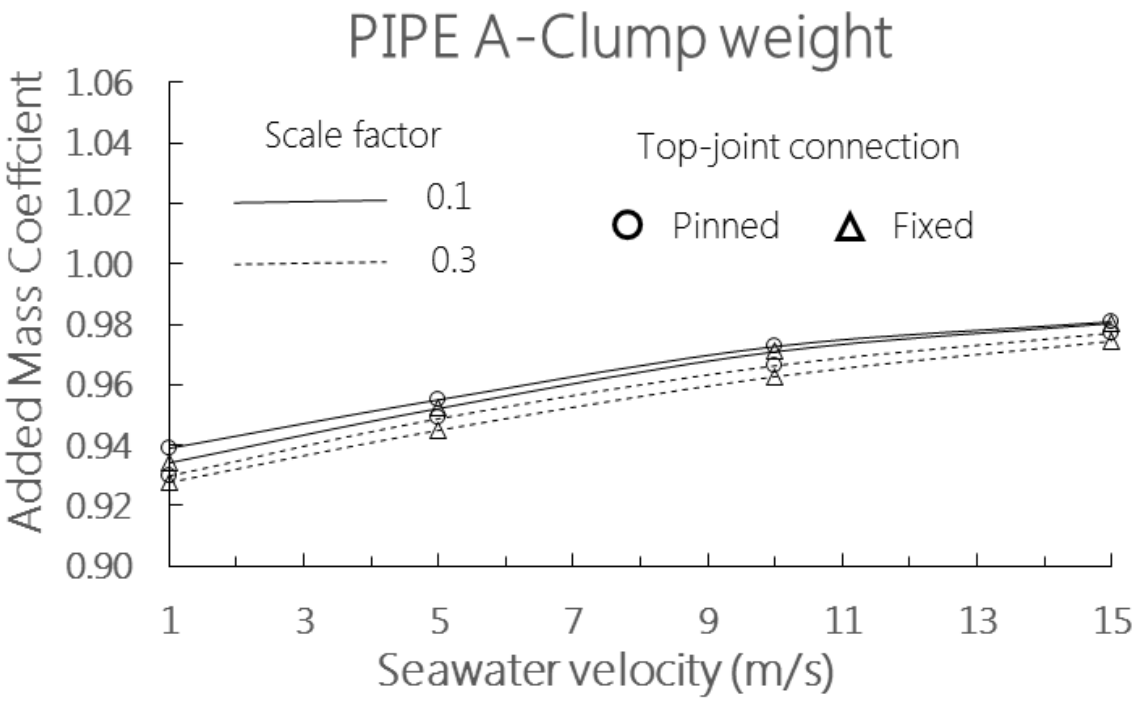

Figure III.7 Effect of scale factor and top-joint connection to the added mass coefficient.

To get more accurate conclusion, the obtained data of the added mass coefficient with all of the parameters are observed using statistical analysis. Identic with the results from visual observation, the results from the statistical analysis states that the seawater transport velocities, material properties, and clump weight installation affect the added mass coefficient with percentage of 43%, 26% and 22% respectively. The rest 9% is the sum up contribution of the scale factor and top joint connection.

The investigation on added mass coefficient is continued by considering the relation between dynamic behavior of the pipe and the added mass coefficient. As shown in figure III.8, considering the coefficient of determination of R^2, the primary parameter which influences the added mass coefficient is the dimensionless amplitude of the pipe vibration, which of course, the vibration amplitude also depends on the parameters such as material properties, etc. Simply stating, the material properties, clump weight installation, and seawater transport velocity influence the dimensionless vibration amplitude and then after all, the vibration amplitude affects the added mass coefficient. This point agrees with the previous study on added mass behavior of oscillating body mentioning that the motion amplitude can affect the added mass coefficient [III.21, III.22].

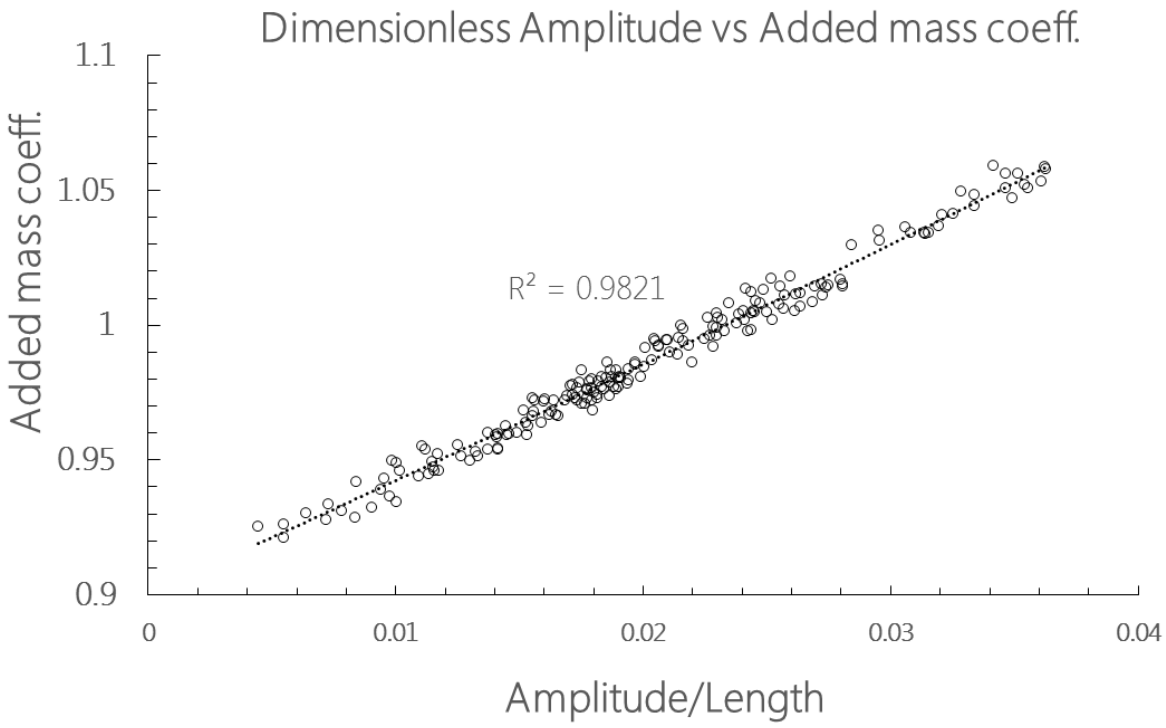

Figure III.8 Effect of motion amplitude to the added mass coefficient.

The second product is the adapted drag coefficient. As in the analytical model, the solution is derived using linearized solution, the desired component of the drag force is the adapted drag coefficient $C_d|V|$ instead of the dimensionless drag coefficient C_d. The equation to calculate the adapted drag coefficient is as follows [III.23]

$$C_d|V| = \frac{2F_d}{\rho_f AV} \quad \text{(III.2)}$$

F_d is the force component obtained from numerical simulation, ρ_f is the ambient fluid density, A is the reference area and V is the motion speed of the pipe at the bottom-end relative to the fluid velocity surrounding the pipe.

In the aim to investigate the contribution of the case variables to the adapted drag coefficient, the procedures used to produce figures III.5- III.7 are repeated which resulting figures III.9- III.11. From the visual observation on figures III.9- III.11 and statistical analysis, the results are similar with the case of added mass coefficient. The adapted drag coefficient is mainly affected by the material properties, clump weight installation and seawater velocities. The effects of scale factor and top joint connection are relatively

unremarkable. Comparing between figures III.9 and III.10 with figure III.11, the adapted drag coefficient of pipe C is about ten times higher compared with pipe A. This is because pipe C has very light density which makes its vibration velocity higher compared with vibration velocity of pipe A.

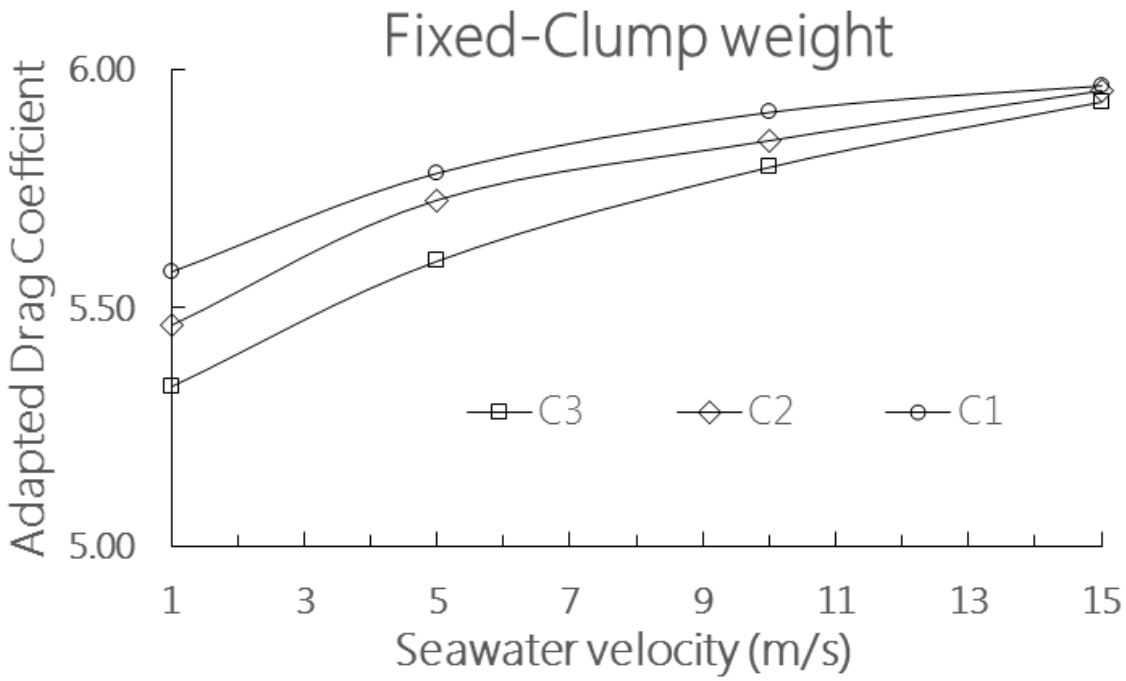

Figure III.9 Effect of material and seawater velocity to the adapted drag coefficient.

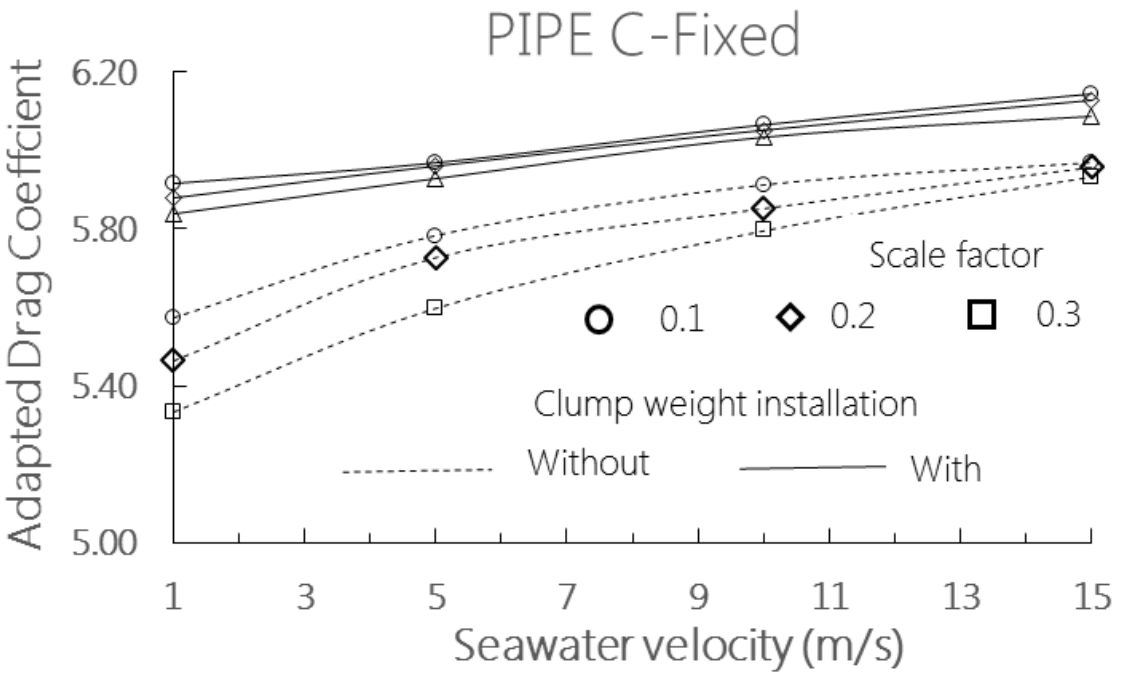

Figure III.10 Effect of clump weight installation to the adapted drag coefficient.

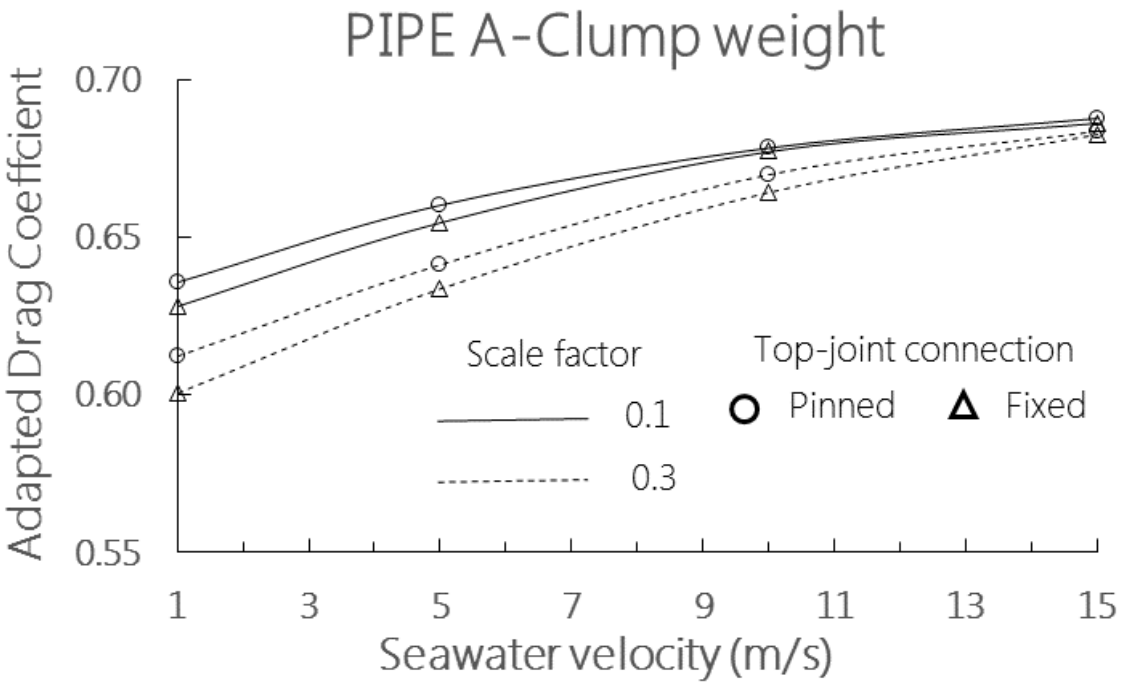

Figure III.11 Effect of scale factor and top-joint connection to the adapted drag coefficient.

To get the primary parameter which influences the adapted drag coefficient is little complicated as its value also depends on the motion velocity of the pipe. Using the statistical programming aided analysis, the adapted drag coefficient is transformed into dimensionless adapted drag coefficient as

$$\xi` = \rho_f D_o \widetilde{C_d} L^2 / \sqrt{EIm_r} \qquad \text{(II.3)}$$

ξ` is the dimensionless adapted drag coefficient (the dimensionless adapted drag coefficient here differs with the adapted drag coefficient in the analytical solution), D_o is outer diameter of the pipe, $\widetilde{C_d}$ is the adapted drag coefficient, L is the riser length, EI is the flexural rigidity and m_r is the riser mass per unit length. The result is shown in figure III.12. Based on figure III.12, referring equation III.3, it can be understood that the correlation between the dimensionless motion amplitude and adapted drag coefficient highly depends on the material properties and the geometry.

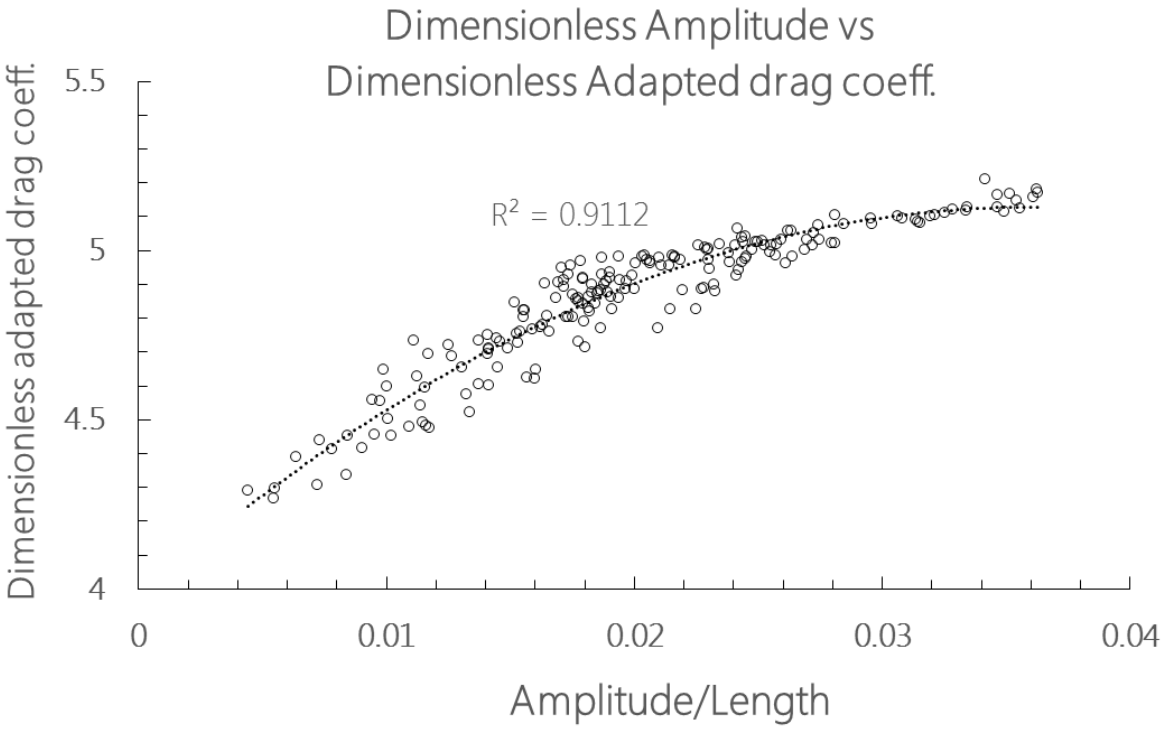

Figure III.12 Dimensionless amplitude versus dimensionless adapted drag coefficient.

Figure III.13 shows the correlation between seawater transport velocity and dimensionless motion amplitude which is defined as ratio between vibration amplitude at the bottom-end over the pipe length. To observe the critical velocity point through the incremental increase of motion amplitude due to an increase of seawater transport velocity is merely hard. For convenience, a conventional bifurcation curve is derived to observe the sudden point where the motion amplitude behaves sensitively toward seawater velocity. Instead of a single point, for more cautiously covering the possible critical velocity, the critical points will be set in range. From figure III.13, as predicted, the instability does occur at certain velocity. At low seawater velocities, the increment of motion amplitude is relatively small, skeptically affected to the change of seawater velocity. After hitting its critical velocity, the motion amplitude become susceptible and exponentially aggravated. By bifurcation curves, the critical velocity can be easily determined between 14 m/s to 15 m/s. The similar procedures are repeated to determine the critical velocity for other case configurations.

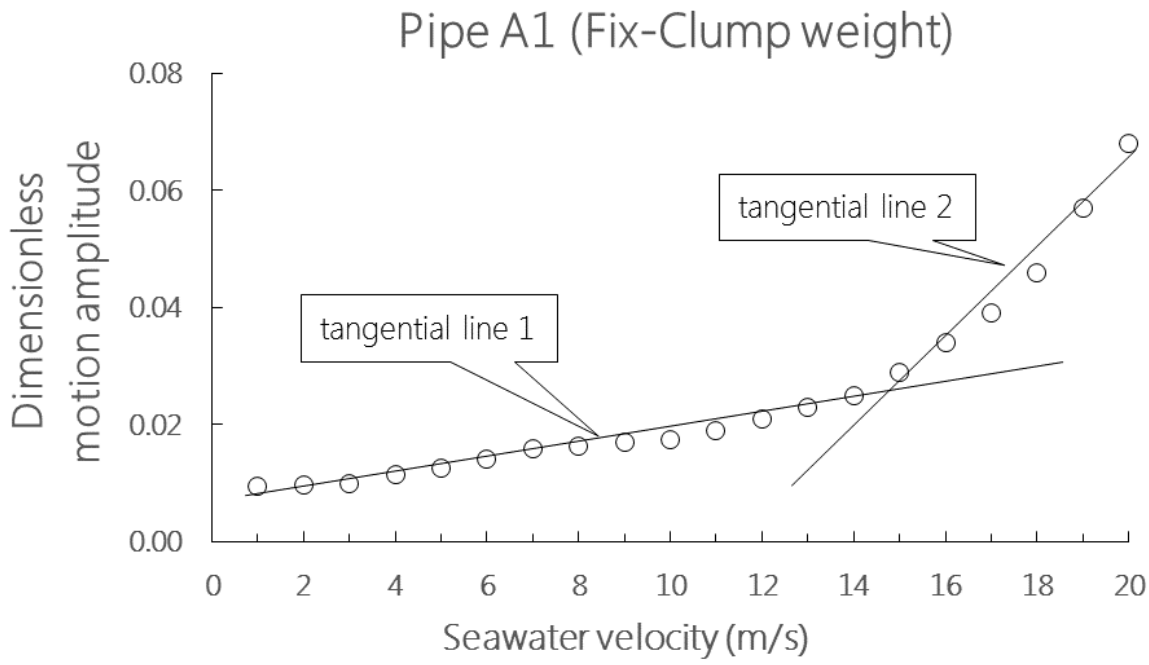

Figure III.13 Dimensionless amplitude versus seawater velocity for pipe A1 (Fixed-Clump weight).

3.4 Analytical simulations

3.4.1 Governing general equation

In the analytical analysis, the motion is observed around the straight configuration and under the following assumptions: 1) the motion of the riser is in two dimensional plane; 2) length over diameter of the riser is large enough so that the system can be investigated based on Euler-Bernoulli theory and plug-flow can be used to model the internal fluid movement; 3) the material damping is considered based on the hysteretic damping model; 4) the motion of the floating structure is not taken into account; 5) the main flow of the velocity along the riser is constant; 5) the external forces and friction force between riser and fluid are neglected.

The riser is tubular with outer diameter D_o, inner diameter D_i, the length L, density ρ_r, and cross sectional area A_r. The riser is submerged in the fluid with density ρ_f and subject to gravitational acceleration g. At time t and at the distance from the top joint , the transverse dispalement of the cross section is denoted as $w(z,t)$. The equation of its undamped lateral motion in the frame of a linearized model can be obtained as [III.12]

$$EI\frac{\partial^4 w}{\partial z^4} - 2u_f m_f \frac{\partial^2 w}{\partial t \partial z} + \left(m_f + m_r + m_a\right)\frac{\partial^2 w}{\partial t^2} + \left(-T_{BT}\left(1-\frac{Z}{L}\right) - W_c + m_f {u_f}^2\right)\frac{\partial^2 w}{\partial z^2} + \frac{T_{top}}{L}\frac{\partial w}{\partial z} + \frac{1}{2}\rho_f D_o \widetilde{C_d}\frac{\partial w}{\partial t} = 0 \quad \text{(III.4)}$$

where EI is the flexural rigidity of the pipe, u_f the velocity of seawater transport, m_f, m_r and m_a mass per unit length of the fluid, bare-riser and added mass, respectively, $\widetilde{C_d}$ adapted drag coefficient, T_{BT} wet weight of bare riser (without clump weight) calculated as $\left(\rho_r - \rho_f\right)A_r g L$, and T_{top} the total top tension (with clump weight) determined as $T_{BT} + W_c$. If installed, W_c is the weight of the clump at the bottom. In this equation, the weight of the bare riser is distributed equally along the riser but the weight of the clump is treated as a point mass located at the bottom end of the pipe. For more details on how to derive equation III.4, refer to [III.12]

If the hysteretic damping of the material with loss factor μ at motion frequency Ω is considered, the equation III.4 reads

$$EI\left[1+\left(\frac{\mu}{\Omega}\right)\frac{\partial}{\partial t}\right]\frac{\partial^4 w}{\partial z^4}-2u_f m_f\frac{\partial^2 w}{\partial t\partial z}+(m_f+m_r+m_a)\frac{\partial^2 w}{\partial t^2}+\left[-T_{BT}\left(1-\frac{Z}{L}\right)-W_c+m_f {u_f}^2\right]\frac{\partial^2 w}{\partial z^2}+\frac{T_{top}}{L}\frac{\partial w}{\partial z}+\frac{1}{2}\rho_f D_o\widetilde{C_d}\frac{\partial w}{\partial t}=0 \quad \text{(III.5)}$$

To solve equation III.5 in a convenient way, it had better to rewrite equation III.5 into dimensionless form by introducing the dimensionless variables as

$$\Delta = w/\mathrm{L}\ \ ;\Gamma = z/\mathrm{L}\ ;\tau = t\sqrt{EI/m_f+m_r+m_a}/L^2\ \ ;\ \omega=\Omega L^2\sqrt{m_f+m_r+m_a/EI}$$

$$\upsilon = u_f\sqrt{m_f/T_{top}}\quad ;\ \ \theta_{top}=T_{top}L^2/EI\quad ;\ \ \theta_{BT}=T_{BT}L^2/EI\quad ;\ \ \theta_C=W_cL^2/EI$$
$$;\ \zeta=\mathrm{L}\sqrt{m_f T_{top}}/\sqrt{EI(m_f+m_r+m_a)}\quad ;\ \xi=\rho_f D_o\widetilde{C_d}L^2/\left(2\sqrt{EI(m_f+m_r+m_a)}\right)$$
$$;\ \Lambda=\alpha\sqrt{EI/m_f+m_r+m_a}/L^2$$

Inserting all of the dimensionless variables above to the equation III.5, the new statement of the problem can be rewritten as

$$\left[1+\left(\frac{\mu}{\omega}\right)\frac{\partial}{\partial\tau}\right]\frac{\partial^4\Delta}{\partial\Gamma^4}+\theta_{top}\upsilon^2\frac{\partial^2\Delta}{\partial\Gamma^2}-(\theta_C+\theta_{BT})\frac{\partial^2\Delta}{\partial\Gamma^2}+\theta_{BT}\Gamma\frac{\partial^2\Delta}{\partial\Gamma^2}+\theta_{top}\frac{\partial\Delta}{\partial\Gamma}-2\zeta\upsilon\frac{\partial^2\Delta}{\partial\Gamma\partial\tau}+\xi\frac{\partial\Delta}{\partial\tau}+\frac{\partial^2\Delta}{\partial\tau^2}=0 \quad \text{(III.6)}$$

Equation III.6 still has variable Γ and variable τ. The next step is simplifying equation III.6 by assuming that

$$\Delta(\Gamma,\tau)=\Pi(\Gamma)e^{\lambda\tau} \quad \text{(III.7)}$$

then, equation III.6 reads

$$(1-\mathrm{i}\mu)\frac{\partial^4\Pi}{\partial\Gamma^4}+\left(\theta_{top}\upsilon^2-\theta_C-\theta_{BT}\right)\frac{\partial^2\Pi}{\partial\Gamma^2}+\theta_{BT}\Gamma\frac{\partial^2\Pi}{\partial\Gamma^2}+\left(\theta_{top}-2\lambda\zeta\upsilon\right)\frac{\partial\Pi}{\partial\Gamma}+(\lambda\xi+\lambda^2)\Pi=0 \quad \text{(III.8)}$$

From equation III.7, it can be simply understood that the system becomes unstable if the eigenvalues λ has a positive real part. At the unstable state, the unstablility happens due to flutter when im $(\lambda)\neq 0$ and by static divergence if im $(\lambda)=0$. Additionally, from equation III.8, it can be shown that the third term of dimensionless differential equation has coefficient that depents on Γ. This brings an implification that the solution of

eigenvalues cannot be solved by sinusoidal equation. Huang and Dareing [III.24] suggested that this kind of a differential form can be solved by a solution in the form of power series expansion as

$$\Pi(\Gamma) = \sum_{n=0}^{\infty} a_n \Gamma^n \tag{III.9}$$

where the constants a_n are some coefficients. If almost all of the a_n is equal to zero, the equation can be so-called polynomial function, but if many of a_n are nonzero, the convergence of the power series must be considered.

Substituting equation III.9 to equation III.8, the new produced equation will have summation product equal to zero which indicates that each term in the series must be equal to zero. Considering this condition, a recurrence relation can be derived as

$$a_n = \left(\frac{i\mu}{n}\right) a_{n-1} + \left(\frac{-\theta_{top}\upsilon^2 + \theta_C + \theta_{BT}}{n(n-1)}\right) a_{n-2} + \left(\frac{-\theta_{BT}(n-2) - \theta_{top} + 2\zeta\upsilon\lambda}{n(n-1)(n-2)}\right) a_{n-3} + \left(\frac{-(\lambda\xi + \lambda^2)}{n(n-1)(n-2)(n-3)}\right) a_{n-4}, \ (n \geq 4) \tag{III.10}$$

In the aim to change the starting n from four to zero, the recurrence relation of equation III.10 is repeated so then a_n can be expressed as a linear summation of a_0, a_1, a_2, a_3, a_4 as

$$a_n = \mathrm{W}_n a_0 + \mathrm{X}_n a_1 + \mathrm{Y}_n a_2 + \mathrm{Z}_n a_3, \ (n \geq 0) \tag{III.11}$$

where W_n, X_n, Y_n, Z_n can be calculated as

$$\begin{bmatrix} \mathrm{W}_n \\ \mathrm{X}_n \\ \mathrm{Y}_n \\ \mathrm{Z}_n \end{bmatrix} = \frac{i\mu}{n} \begin{bmatrix} \mathrm{W}_{n-1} \\ \mathrm{X}_{n-1} \\ \mathrm{Y}_{n-1} \\ \mathrm{Z}_{n-1} \end{bmatrix} + \frac{-\theta_{top}\upsilon^2 + \theta_C + \theta_{BT}}{n(n-1)} \begin{bmatrix} \mathrm{W}_{n-2} \\ \mathrm{X}_{n-2} \\ \mathrm{Y}_{n-2} \\ \mathrm{Z}_{n-2} \end{bmatrix} + \frac{-\theta_{BT}(n-2) - \theta_{top} + 2\zeta\upsilon\lambda}{n(n-1)(n-2)} \begin{bmatrix} \mathrm{W}_{n-3} \\ \mathrm{X}_{n-3} \\ \mathrm{Y}_{n-3} \\ \mathrm{Z}_{n-3} \end{bmatrix} + \frac{-(\lambda\xi + \lambda^2)}{n(n-1)(n-2)(n-3)} \begin{bmatrix} \mathrm{W}_{n-4} \\ \mathrm{X}_{n-4} \\ \mathrm{Y}_{n-4} \\ \mathrm{Z}_{n-4} \end{bmatrix} \tag{III.12}$$

the initial condition of the equation III.12 can be defined based on the transformation of equation III.10 to equation III.11 as

$$\begin{bmatrix} W_0 & W_1 & W_2 & W_3 \\ X_0 & X_1 & X_2 & X_3 \\ Y_0 & Y_1 & Y_2 & Y_3 \\ Z_0 & Z_1 & Z_2 & Z_3 \end{bmatrix} = \begin{bmatrix} 1 & 0 & 0 & 0 \\ 0 & 1 & 0 & 0 \\ 0 & 0 & 1 & 0 \\ 0 & 0 & 0 & 1 \end{bmatrix} \quad \text{(III.13)}$$

Finally, by replacing a_n in the equation III.9 with equation III.12, the form of the equation III.9 will be

$$\Pi(\Gamma) = \sum_{n=0}^{\infty}(W_n a_0 + X_n a_1 + Y_n a_2 + Z_n a_3)\Gamma^n \quad \text{(III.14)}$$

3.4.2 Boundary condition and general solutions

To find the four unknown $a_j, j = 0..3$, equation III.14 must be substituted into boundary condition which differs depending on the case of the end-tip connection. As mentioned briefly in section 3.2, six combinations of pipe end boundary conditions are investigated including: fixed-free (Fig III.2a), flexible-free (Fig III.2b), pinned-free (Fig III.2c), fixed-clump weight (Fig III.2d), flexible- clump weight (Fig III.2e), pinned-clump weight (Fig III.2f). The boundary conditions can be expressed as follows:

Boundary conditions at the top end of the pipe

Fixed joint : $w(0,t) = 0$; $EI\frac{\partial w}{\partial z}\Big|_{z=0} = 0$ (III.15)

Flexible joint : $w(0,t) = 0$; $EI\frac{\partial^2 w}{\partial z^2}\Big|_{z=0} = C_{fl}\frac{\partial w}{\partial z}\Big|_{z=0}$ (III.16)

Pinned joint : $w(0,t) = 0$; $EI\frac{\partial^2 w}{\partial z^2}\Big|_{z=0} = 0$ (III.17)

Boundary conditions at the bottom-end of the pipe

Free : $EI\frac{\partial^2 w}{\partial z^2}\Big|_{z=L} = 0$; $EI\frac{\partial^3 w}{\partial z^3}\Big|_{z=L} = 0$ (III.18)

Clump weight : $EI\frac{\partial^2 w}{\partial z^2}\Big|_{z=L} = 0$; $EI\frac{\partial^3 w}{\partial z^3}\Big|_{z=L} = \frac{W_c}{L}w(L,t)$ (III.19)

Where C_{fl} is the stiffeness of the rotational spring and W_c is the weight of the bottom clump. Tranforming the boundary condition into dimensionless form, the new statement of the boundary condition can be explained as:

Dimensionless expression of the boundary conditions at the top end of the pipe

Fixed joint : $\Delta(0,\tau) = 0$; $\left.\frac{\partial\Delta}{\partial\Gamma}\right|_{\Gamma=0} = 0$ (III.20)

Flexible joint : $\Delta(0,\tau) = 0$; $\left.\frac{\partial^2\Delta}{\partial\Gamma^2}\right|_{\Gamma=0} = K\left.\frac{\partial\Delta}{\partial\Gamma}\right|_{\Gamma=0}$ (III.21)

Pinned joint : $\Delta(0,\tau) = 0$; $\left.\frac{\partial^2\Delta}{\partial\Gamma^2}\right|_{\Gamma=0} = 0$ (III.22)

Dimensionless expression of the boundary conditions at the bottom-end of the pipe

Free : $\left.\frac{\partial^2\Delta}{\partial\Gamma^2}\right|_{\Gamma=1} = 0$; $\left.\frac{\partial^3\Delta}{\partial\Gamma^3}\right|_{\Gamma=1} = 0$ (III.23)

Clump weight : $\left.\frac{\partial^2\Delta}{\partial\Gamma^2}\right|_{\Gamma=1} = 0$; $\left.\frac{\partial^3\Delta}{\partial\Gamma^3}\right|_{\Gamma=1} = K_C\Delta(L,\tau)$ (III.24)

K is defined as $C_{fl}L/EI$ and K_C is defined as W_cL^2/EI. The next step is inserting the boundary condition into equation III.14. This yields four linear algebraic equation with respect to $a_j, j = 0..3$.

The method to derive the general solution using these boundary expressions is basically similar for all cases. For example, let`s call the case 2 where the riser is a free hanging riser subjected to a rotational restraint at the end-tip of downstream point. In this case, equation III.21 and equation III.23 are used. For the first and the second boundary condition (Eq. III.21), it can be concluded that

$a_0 = 0$ and $a_2 = \frac{K}{2}a_1$ (III.25)

Then, equation III.25 along with the third and the fourth boundary conditions (Eq. III.23) are substitued into equation III.14, so the new relation will yield as

$$a_1(\sum_{n=2}^{\infty} \mathrm{X}_n n(n-1) + a_2 \sum_{n=2}^{\infty} \mathrm{Y}_n n(n-1)) + a_3 \sum_{n=2}^{\infty} \mathrm{Z}_n n(n-1) = 0 \qquad \text{(III.34)}$$

$$a_1(\sum_{n=3}^{\infty} \mathrm{X}_n n(n-1)(n-2) + a_2 \sum_{n=3}^{\infty} \mathrm{Y}_n n(n-1)(n-2)) + a_3 \sum_{n=3}^{\infty} \mathrm{Z}_n n(n-1)(n-2) = 0 \qquad \text{(III.35)}$$

Equations III.34 - III.35 have a non-trivial solution if and only if the determinant of following matrix is equal to zero.

$$\begin{vmatrix} \frac{K}{2} & -1 & 0 \\ \sum_{n=2}^{\infty} \mathrm{X}_n n(n-1) & \sum_{n=2}^{\infty} \mathrm{Y}_n n(n-1) & \sum_{n=2}^{\infty} \mathrm{Z}_n n(n-1) \\ \sum_{n=3}^{\infty} \mathrm{X}_n n(n-1)(n-2) & \sum_{n=3}^{\infty} \mathrm{Y}_n n(n-1)(n-2) & \sum_{n=3}^{\infty} \mathrm{Z}_n n(n-1)(n-2) \end{vmatrix} = 0 \qquad \text{(III.36)}$$

Using equation III.36, the eigenvalues of equation III.7 can be obtained for the case 2. By repeating the method for cases 2, the general solutions of the others cases can be expressed as

Fixed-free (case 1)

$$\begin{vmatrix} (\sum_{n=2}^{\infty} \mathrm{Y}_n n(n-1)) & (\sum_{n=2}^{\infty} \mathrm{Z}_n n(n-1)) \\ (\sum_{n=3}^{\infty} \mathrm{Y}_n n(n-1)(n-2)) & (\sum_{n=3}^{\infty} \mathrm{Z}_n n(n-1)(n-2)) \end{vmatrix} = 0 \qquad \text{(III.37)}$$

Pinned- free (case 3)

$$\begin{vmatrix} (\sum_{n=2}^{\infty} \mathrm{X}_n n(n-1)) & (\sum_{n=2}^{\infty} \mathrm{Z}_n n(n-1)) \\ (\sum_{n=3}^{\infty} \mathrm{X}_n n(n-1)(n-2)) & (\sum_{n=3}^{\infty} \mathrm{Z}_n n(n-1)(n-2)) \end{vmatrix} = 0 \qquad \text{(III.38)}$$

Fixed- clump weight (case 4)

$$\begin{vmatrix} (\sum_{n=2}^{\infty} \mathrm{Y}_n n(n-1)) & (\sum_{n=2}^{\infty} \mathrm{Z}_n n(n-1)) \\ \left((\sum_{n=3}^{\infty} \mathrm{Y}_n n(n-1)(n-2)) - K_T \sum_{n=0}^{\infty} \mathrm{Y}_n\right) & \left((\sum_{n=3}^{\infty} \mathrm{Z}_n n(n-1)(n-2)) - K_T \sum_{n=0}^{\infty} \mathrm{Z}_n\right) \end{vmatrix} = 0 \qquad \text{(III.39)}$$

Flexible- clump weight (case 5)

$$\begin{vmatrix} \frac{K}{2} & -1 & 0 \\ d & e & f \\ h-a & i-b & j-c \end{vmatrix} = 0 \qquad \text{(III.40)}$$

where

$a = K_T \sum_{n=0}^{\infty} \mathrm{X}_n$, $b = K_T \sum_{n=0}^{\infty} \mathrm{Y}_n$, $c = K_T \sum_{n=0}^{\infty} \mathrm{Z}_n$, $d = \sum_{n=2}^{\infty} \mathrm{X}_n n(n-1)$, $e = \sum_{n=2}^{\infty} \mathrm{Y}_n n(n-1)$, $f = \sum_{n=2}^{\infty} \mathrm{Z}_n n(n-1)$, $h = \sum_{n=3}^{\infty} \mathrm{X}_n n(n-1)(n-2)$, $i = \sum_{n=3}^{\infty} \mathrm{Y}_n n(n-1)(n-2), j = \sum_{n=3}^{\infty} \mathrm{Z}_n n(n-1)(n-2)$

Pinned- clump weight (case 6)

$$\begin{vmatrix} (\sum_{n=2}^{\infty} \mathrm{X}_n n(n-1)) & (\sum_{n=2}^{\infty} \mathrm{Z}_n n(n-1)) \\ \left((\sum_{n=3}^{\infty} \mathrm{X}_n n(n-1)(n-2)) - K_T \sum_{n=0}^{\infty} \mathrm{X}_n\right) & \left((\sum_{n=3}^{\infty} \mathrm{Z}_n n(n-1)(n-2)) - K_T \sum_{n=0}^{\infty} \mathrm{Z}_n\right) \end{vmatrix} = 0 \qquad \text{(III.41)}$$

3.4.3 Analytical results

By inputting the material properties and the model scantlings shown in table III.1 with the added mass coefficient and adapted drag coefficient projected from numerical simulation results into the analytical solutions, the natural frequency, in the form of complex number, can be obtained for each corresponding case. The instability of the riser can be determined by plotting its natural frequency parametrically in an Argand diagram. The correlation between the natural frequency and the eigenvalues of the solutions is conditioned as $\omega = i\lambda$. The instability takes place when the imaginary part of the natural frequency is negative.

This section is to particularly interpret the result of the analytical simulations. The simulation is done for pipes A4-C4 but to emphasize the explanation, the concentration, as a sample, will be focus on the pipe A4. Figures 14-16 show the Argand diagram for Pipe A4 with fixed at the top-end and clump weight ($K_c = 0.1$) at the bottom for mode 1, mode 2 and mode 3 respectively. For visual observation, the shape of modes 1, 2 and 3 for velocity of 6 m/s are plotted in figure III.17.

Firstly, by imposing zero fluid velocity and zero adapted drag coefficient, the real value of the natural frequency for all modes of interest can be assessed. The solver uses this value as a first hint to determine the natural frequency for the next conditions. Then by keeping zero fluid velocity but setting the adapted drag coefficient as projected from the numerical simulation, point a ($u_f = 0$) in figures III.14- III.16 can be assessed. The next step is gradually increasing the seawater velocity resulting decrement of the imaginary part. The critical velocity occurs when the imaginary part of the natural frequency reaches zero point (point b in figures III.14- III.16, $u_f = u_{critical}$). The simulation continues until the seawater velocity of 1.25 times of the critical velocity (point c in figures III.14- III.16, $u_f = 1.25\ u_{critical}$).

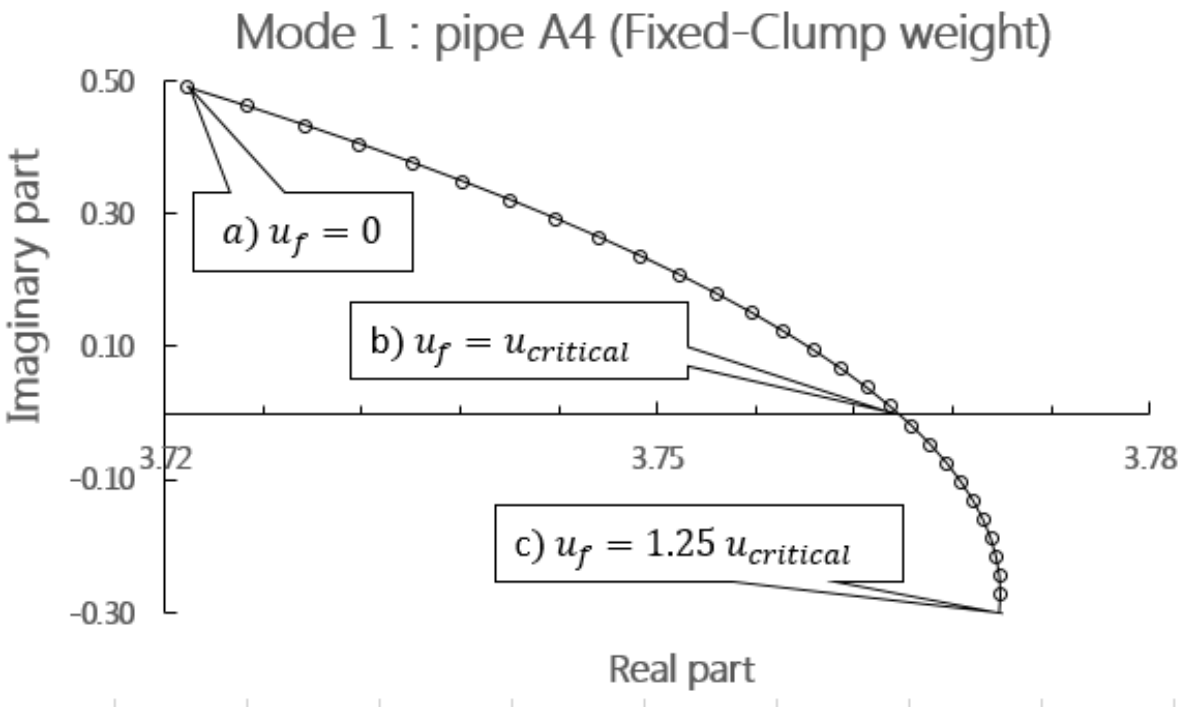

Figure III.14 Argand diagram mode 1 for pipe A4 (Fixed-Clump weight).

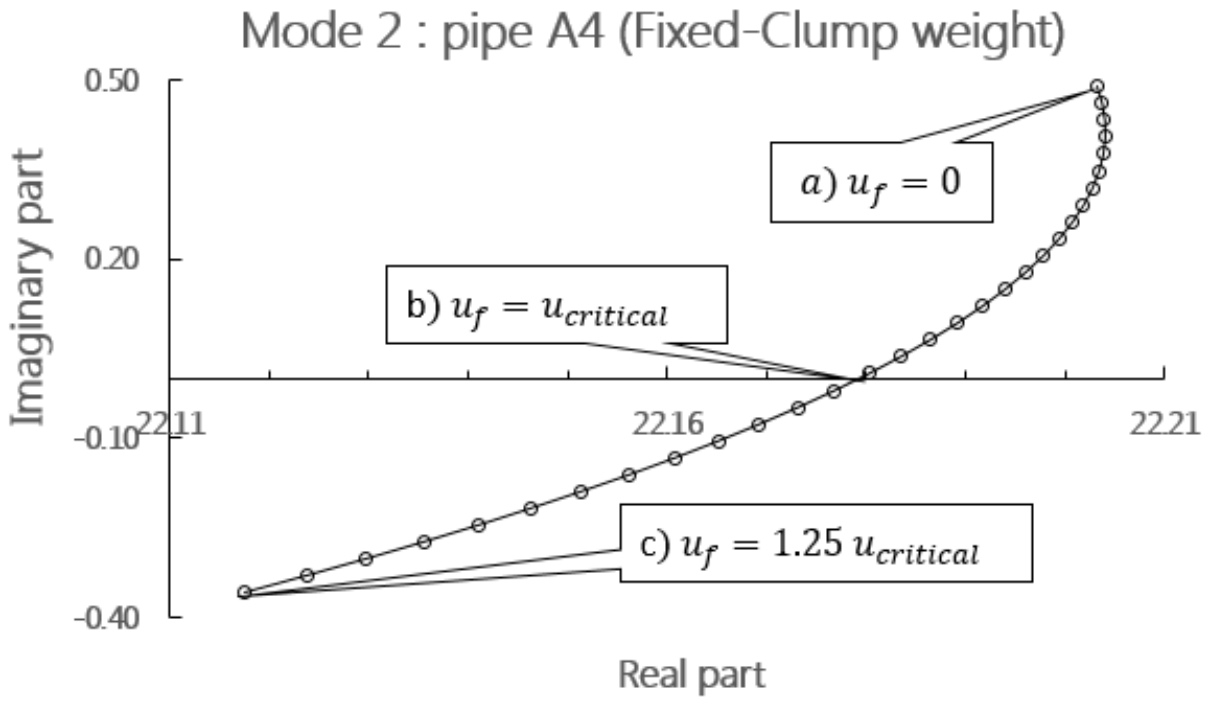

Figure III.15 Argand diagram mode 2 for pipe A4 (Fixed-Clump weight).

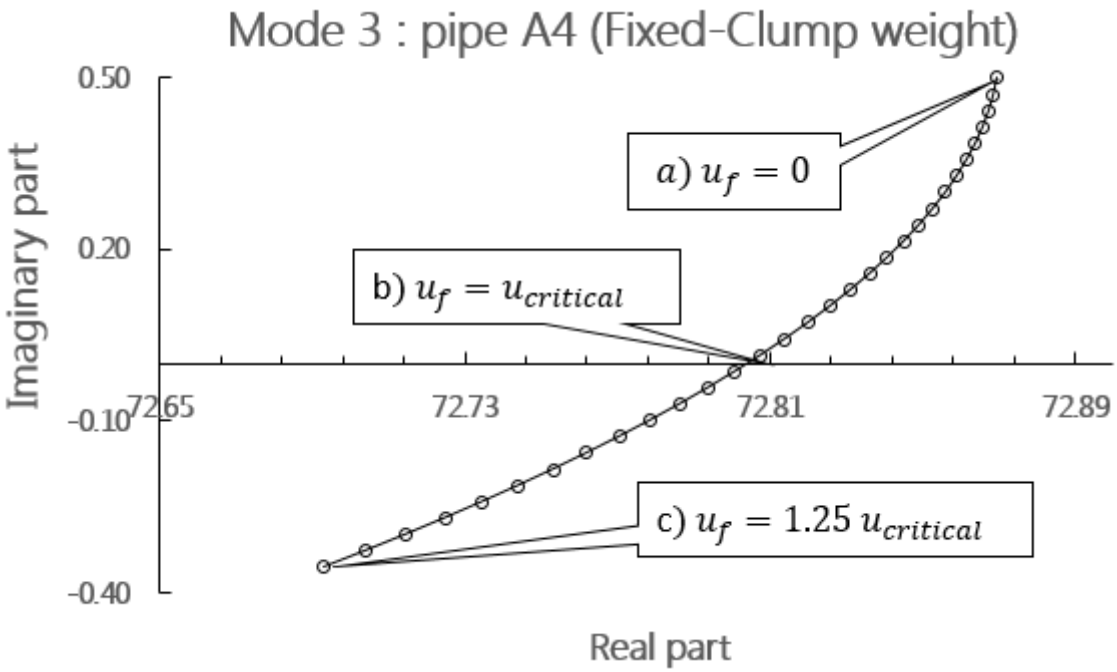

Figure III.16 Argand diagram mode 3 for pipe A4 (Fixed-Clump weight).

To investigate the effects of the end-tip boundary conditions to the critical velocity, tables III.3 and III.4 are produced. In table III.3, free hanging (no clump weight) pipe A4 is used and the top end joint is set as fixed, pinned and flexible joint with dimensionless stiffness, K of 0.01, 0.1, 1, 10 and 100. Theoretically, very high value K, the flexible joint can be seen as a fixed joint. On the contrary, very low K of flexible joint assemblies the system of pinned joint. From table III.3, it is shown that the effect of the top-joint connection to the critical velocity is not small, with range about 15% between pinned and fixed joint. The dependence of the critical velocity is very weak for very small and very high K but very sensitive for $10^{-1} \leq K \leq 10^{1}$. How the critical velocity behaves due to variation of flexible joint stiffness acquired here agrees well with the existing theory on pipe conveying fluid as can been found in [III.25].

Table III.3 Critical velocity (m/s) for various conditions of top-end joint observed in pipe A4 with no clump weight.

Top end joint		Mode		
		1	2	3
Pinned		7.99	8.02	8.04
Flexible joint $K =$	0.01	8.01	8.05	8.06
	0.1	9.04	9.07	9.08
	1	9.10	9.14	9.15
	10	9.15	9.19	9.19
	100	9.16	9.19	9.20
Fixed		9.17	9.20	9.20

In table III.4, pipe A4 with fixed at the top and clump weight installation at the bottom is investigated to observe the effect of the clump weight to the critical velocity behavior. The dimensionless parameter of the clump weight, K_c is set as 0, 0.026, 0.052, 0.08 and 1.05 which corresponds to the 0%, 25%, 50%, 75%, and 100% of the pipe weight respectively. From the results, it can be concluded that installing clump weight at the bottom of the pipe can effectively increase the stability of the pipe. Considering tables III.3 and III.4 together, they inform that the critical velocity of the mode 1 is smaller compared with the other modes. Since the most crucial critical velocity happens in the mode 1, here onwards, the analytical analysis will be used as the basis observation.

Table III.4 Critical velocity (m/s) for various values of dimensionless clump weight variable observed in pipe A4 with fixed at the top.

Top end joint		Mode		
		1	2	3
Free hanging, $K_c = 0$		9.17	9.20	9.20
Clump weight $K_c =$	0.026	9.30	9.36	9.36
	0.052	10.04	10.09	10.09
	0.08	10.55	10.59	10.59
	1.05	11.03	11.06	11.06

3.5 Analytical and Numerical results comparison

The subject of this section is to judge the acceptance of the analytical model before being used to analyze the pipe in full scale size. The comparison includes the mode shape, top joint stress, and the critical velocity for pipes A4, B4, and C4 in various end tip boundary conditions. For the numerical analysis, the mode shape and top joint stress can be directly obtained from the simulation. The critical velocity can be also observed using bifurcation curves as explained in section 3.2. But for the analytical simulation, as the final results strongly depends on the input data, more efforts are necessary to ensure that the input data are correct and meticulous especially for the value of the added mass coefficient and the adapted drag coefficient.

The value of the added mass coefficient and adapted drag coefficient of pipes A1-3, B1-3, and C1-3 are plotted versus each variable e.g. added mass vs scale factor, added mass vs seawater velocity, adapted drag coefficient vs scale factor, etc. From the graph, an equation correlating the added mass coefficient or the adapted drag coefficient with the observed variable can be derived. The equation is then used to project the added mass and adapted drag coefficient of pipe A4, B4, and C4. Then, the projected added mass coefficient and adapted drag coefficient are compared with the numerical results of the same pipes. The results show that the difference between the projected ones and the measured using numerical simulation is averagely only 2%, which is definitely a good agreement. Furthermore, the result also emphasizes the conclusion derived from the numerical simulation results in section 3.2 that the value of the added mass coefficient and the adapted drag coefficient are influenced by the material properties, clump weight installation and seawater velocities but unremarkable by the top-joint connection and scale factor.

Inserting the projected added mass coefficient, adapted drag coefficient, material properties and the scantlings for particular cases, the mode shapes and the critical velocity can be obtained via analytical simulation. Figures III.17 and III.18 show the mode shape comparison of pipe A4 (fixed top-bottom free) and pipe A4 (fixed top-clump weight, $K_c = 0.052$) respectively. Numerical simulation results show that without any advanced treatment, the vibration of the pipe naturally behaves in mode 1. Taken the data together,

the mode shapes obtained from the numerical simulation and analytical simulation agree each other well with the gap of 3%-6% in which the analytical results over-estimates the numerical ones. The effects of the clump weight to the motion amplitude can be found very significant. It can decrease the motion amplitude up to 30%. Of course it also depends on the size of the clump weight and the other variables. With clump weight installation (see figure III.19), the motion amplitude is close to zero for very small seawater velocity. From tables III.3 and III.4, the critical velocity for figure III.18 is 7.17 m/s and for figure III.19 is 8.04 m/s. Before reaching its critical point, the increase of the motion amplitude is very small. But after hitting the critical state, sharp amplitude rise takes place.

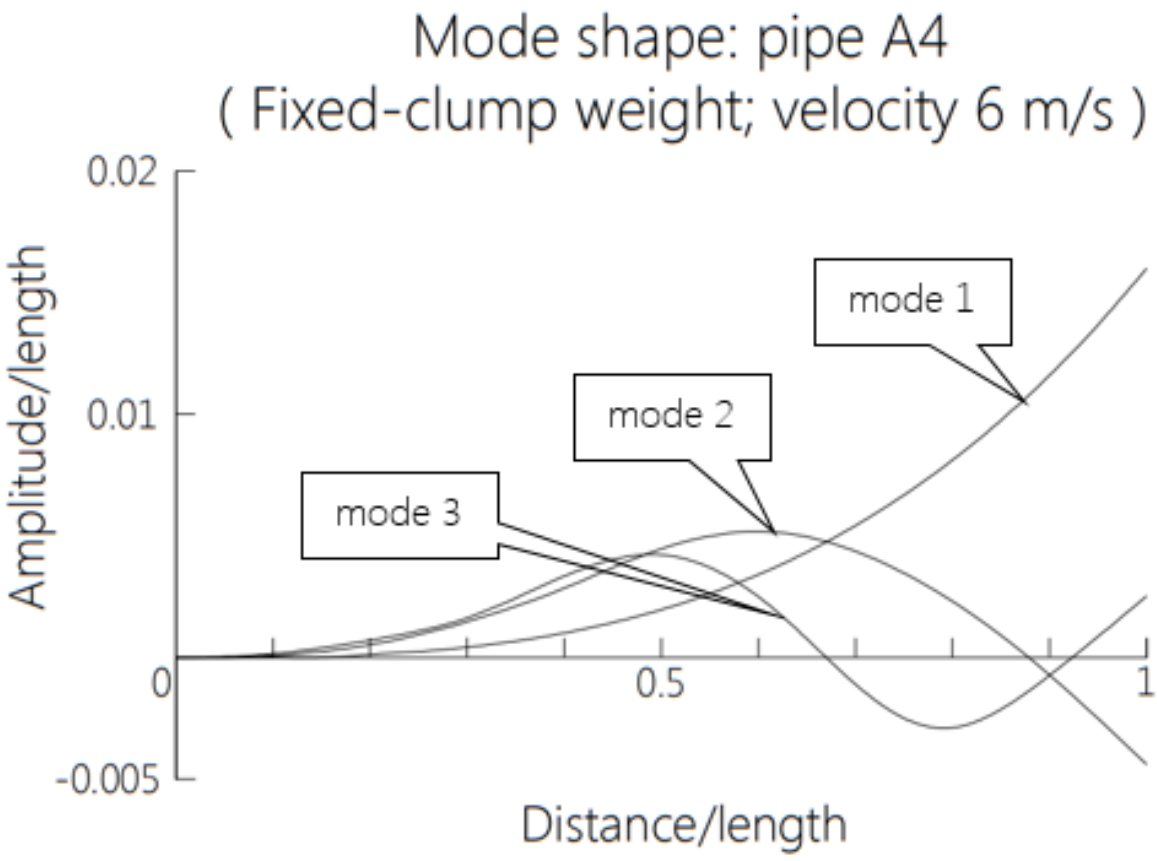

Figure III.17 The shape of modes 1, 2 and 3 for A4 (Fixed- No clump weight; velocity 6 m/s).

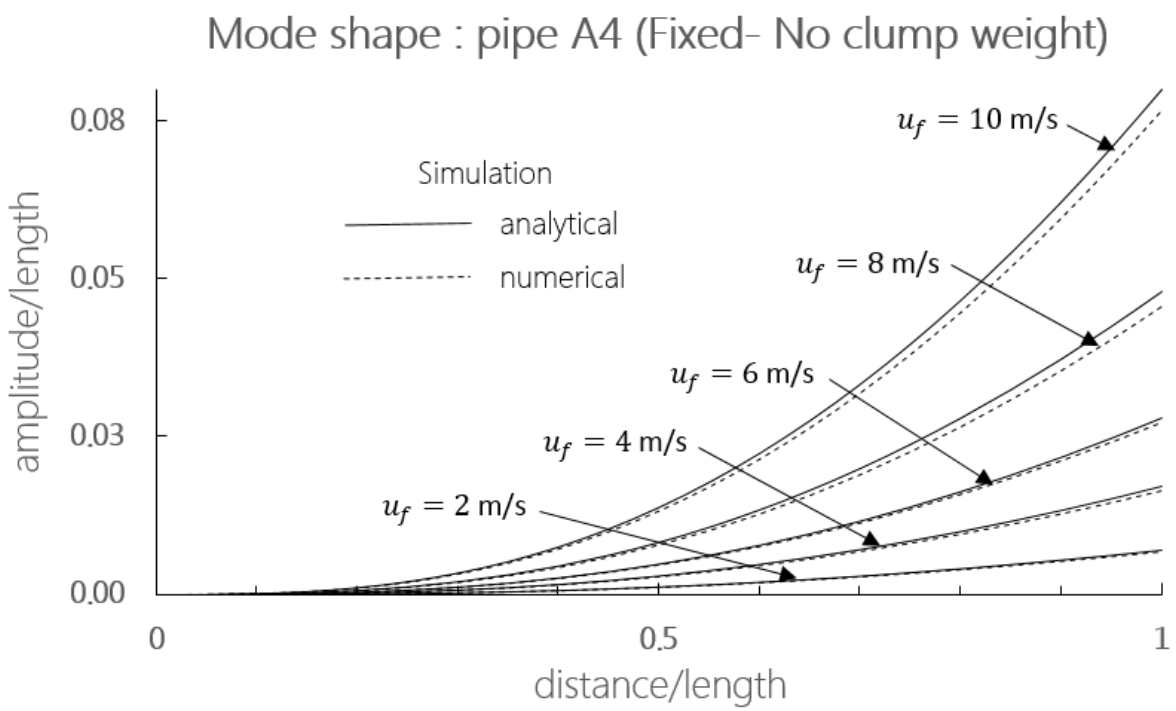

Figure III.18 Mode shape for pipe A4 (Fixed- No clump weight).

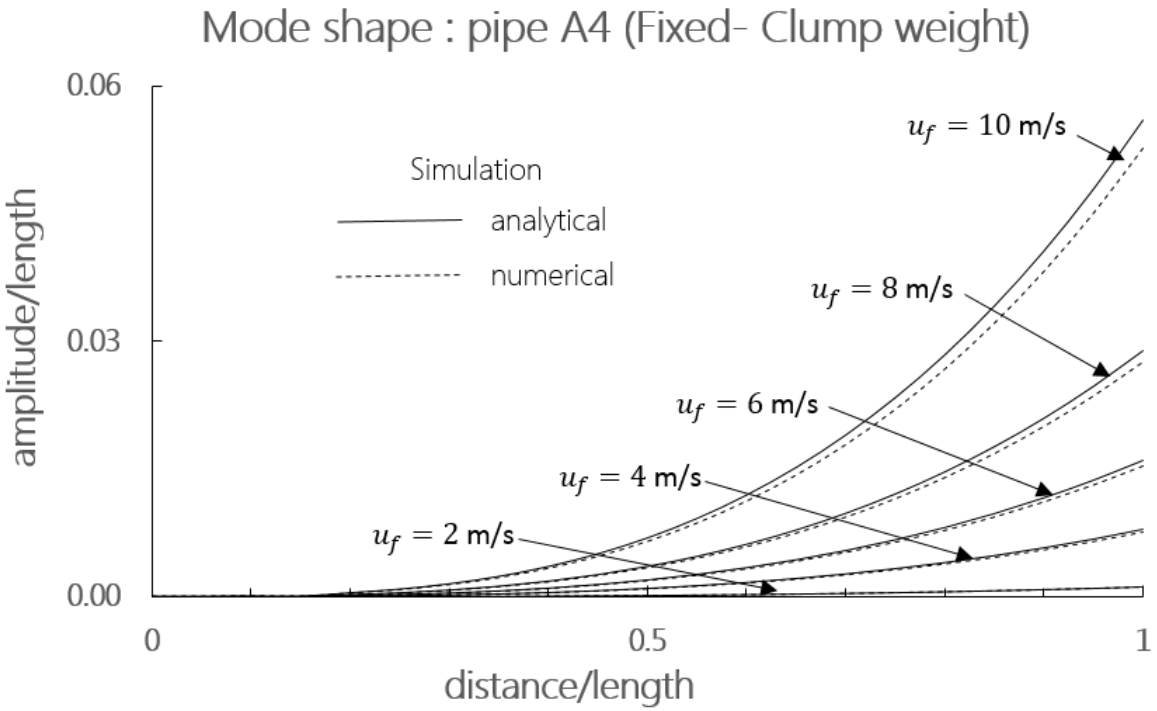

Figure III.19 Mode shape for pipe A4 (Fixed- Clump weight).

Except the axial loads due to self-weight, the riser is also subject to bending stress due to beam motion. The axial loads are distributed uniformly on the entire cross section. In case of the bending stress, the maximum stress, either in tension or compression, will be on the outer surface of the pipe. As both stresses act normal to the cross section, the resulting stress will be the combination of the two separate stresses $\sigma_A + \sigma_B$. The equation to calculate the axial stress σ_A is calculated as

$$\sigma_A = T_Z / A_r \tag{III.42}$$

where T_Z is the tension at point z including the clump weight which is calculated as $(\rho_r - \rho_f)A_r g(L - z) + W_c$, and A_r is cross sectional area of the pipe. The bending stress σ_B is calculated as

$$\sigma_B(z) = E\frac{\partial^2 w(z)}{\partial z^2}\frac{D_o}{2} \tag{III.43}$$

E is the modulus elasticity of the material. Simply speaking, the bending stress depends on the second derivative of the motion displacement as function of z. In the top fixed configuration, the bending stress maximum occurs at the top end joint which literally the maximum stress will also occur at the top end joint. But for other types, the maximum bending moment is located somewhere along the pipe. In this case, the maximum stress is observed at a point in which $-(\rho_r - \rho_f)A_r g + \partial^3 w(z)/\partial z^3 = 0$.

The final comparison results are shown in tables III.5 and III.6 for the critical velocity and top stress respectively. In table III.5, for the boundary condition, stiffness of the flexible joint at the top is set as $K = 1$ and the clump weight is 50 % of riser weight for heavy material (Steel and aluminum) and 100% of riser weight for FRP. The results show that the critical velocity predicted by analytical simulation is all in range of the critical velocity predicted by numerical simulation. The difference is only 2-6% if the analytical results are compared with the mid-value of the numerical ones. For the material choice comparison, the table indicates that the critical velocity of steel material is above compared with others. In instance, it can be said that the critical velocity increase by increasing the value of $m_r/(m_f + m_r + m_a)$ and the value of flexural rigidity, for which already well-known from the general knowledge on pipe aspirating behavior [III.25].

Table III.5 Critical velocity (m/s) comparison for pipe with scale factor 0.4.

End tip boundary condition	Pipe A4		Pipe B4		Pipe C4	
	Ana.	Num.	Ana.	Num.	Ana.	Num.
Pinned-Free	7.99	7.4-8.2	6.02	5.5-6.6	4.21	3.7-4.4
Flexible-Free	9.04	8.1-9	7.81	7-8.8	5.8	5.4-6.6
Fixed-Free	9.17	8.5-9.5	8.76	8.1-9	6.31	6.1-7.1
Pinned –Clump weight	10.04	9.4-10.4	9.91	9.5-10.4	7.41	7.8-7.5
Flexible-Clump weight	11.01	10.3-11.4	10.88	10.3-11.4	9.23	9-10.6
Fixed –Clump weight	12.6	12-13	11.23	10.7-11.4	10.2	9.6-10.4

Table III.6 shows the comparison results for the top joint stress and the motion frequency. The comparison is only done for the top-fixed joint and the weight of the clump is 50 % of riser weight. In general, the top stress predicted by the analytical simulation is 3%-6% lower compared with the ones obtained from the numerical simulations. Regarding the effect of the clump weight installation, it is able to decrease the top stress, of course the stress due to axial strain gets higher but the bending stress lessens more than the increase of the axial stress. The decrease of the bending stress is due to the capability of the clump weight to decrease the motion amplitude. In case of the frequency comparison, from table III.6, the results obtained from the analytical and numerical simulation are very close. The table also shows that the clump weight can also decrease the motion frequency.

Table III.6 Top stress over yield stress and motion frequency comparison for pipe in top-fixed configuration with scale factor 0.4 observed at critical velocity.

Pipe	Method	T_{top}/σ_{yield}		Frequency of the first mode (Hz)	
		Fixed-Free	Fixed-clump	Fixed-Free	Fixed-clump
A4	Ana.	0.361	0.321	0.72	0.54
	Num.	0.366	0.328	0.77	0.56
B4	Ana.	0.142	0.098	0.84	0.61
	Num.	0.148	0.102	0.86	0.65
C4	Ana.	0.084	0.073	1.36	0.98
	Num.	0.087	0.075	1.42	1.02

Taking tables III.5 and III.6 together, in the view of critical velocity, the heavy materials are better as they are more stable and the motion amplitude is less. But considering the top stress, heavy material makes the top-joint suffer from the large stress. From the tables, the suggestion is to use light materials (FRP) with clump weight installation. The light material choice is intended to minimize the top stress and the clump weight installation is to stabilize the system. More strictly consideration, in the top-fixed configuration, for the FRP, by installing clump weight, the critical velocity increases up to 50% and the top stress decreases up to 30%. The sensitivity of the critical velocity and the top joint stress on the clump weight installation effect definitely also varies depending on the other type of boundary condition. But generally speaking, it can be used as a clue that clump weight installation give significant effects to the critical velocity.

As final conclusion of the comparison study, considering the gap between analytical results and numerical results, it can be concluded that the analytical solution is accepted

enough to be used for the full scale models.The main aims of the numerical simulations are to obtain the values of the added mass coefficient.

3.6 Full scale models analysis

The next step of the analysis is carrying out the analytical simulation for the full scale model. The scantling and material properties are shown in table III.1. For all pipes models, in case of flexible joint at the top, the stiffness K, is varied from 0.01 to 100 with increment of logarithmic scale base 10. For the clump weigh, its weight over the riser weight is set as 25% to 150% with increment of 25%. The step by step procedure to undergo the analytical solution for full scale model is exactly same with the analytical simulation for the scaled model as already explained in section 4.3.

Considering the critical velocity and the maximum stress, deciding the best solutions through graphical comparison is possible, yet time consuming and inefficient. To ease, a post processing program is generated to automatically produce the best solutions. The acceptance criteria include the critical velocity and the top joint stress. The minimum critical velocity is 2.5 m/s, which is 0.5 m/s higher than the required one (see chapter 2). The upper limit ratio between the maximum stress over the yield stress is set to be 0.7, which means safety margin of 0.3 is imposed. This number is considered based on the unacceptable consequence of failure and the requirement of underwater accessibility for inspections [III.26]. In early stage of the analysis, the analysis finds a condition where the ratio between the maximum stress over the yield stress has reached 0.7 before the velocity has not been beyond its critical value. At this condition, the velocity where the ratio between the maximum stress over the yield stress hits 0.7 is determined as the critical velocity.

Table III.7 shows the results of the analytical simulations for the full scale model. Steel material is not recommended in all case of end-tip boundary conditions. The achieved maximum critical velocity is only 1.4 m/s, which is below the required one. For aluminum, the results state that this material is acceptable for same extents. The top joint connection must be set in pinned configuration and clump weight must be installed at 50% of bare-riser (without clump weight) weight. Yet after all, the obtained value is in precarious stage. The maximum stress is very close with the margin. The most prospective

material is FRP, its low material density makes the maximum stress relatively small and its high yield stress make it possible to choose various type of top joint connection. For FRP, the required weight of the bottom clump is at least 50% of the riser weight, which is practically accepted. For the vibration frequency, its value is relatively large which indicates that the system vibrates fast.

Table III.7 Analytical results of full scale models.

Material	End-tip configurations		Critical velocity (m/s)	$\frac{T_{top}}{\sigma_{yield}}$	Note	Frequency of the first mode (Hz)
	Top-joint	Clump weight (% W_r)				
Steel	Pinned	50	1.4	0.7	Not accepted	0.86
Aluminum	Pinned	50	2.2	0.66	Accepted	0.975
FRP	Flexible $K = 0.1$	50	2.3	0.237	Accepted	1.725
	Flexible $K = 0.1$	100	2.8	0.217	Accepted	1.561
	Flexible $K = 1$	100	3.95	0.261	Accepted	1.224
	Pinned	100	3.2	0.156	Accepted	1.975
	Pinned	150	3.6	0.128	Accepted	1.806

3.7 Conclusions

The stability analysis of submerged, top-tensioned free hanging riser has been investigated by numerical and analytical methods. The analytical approach is developed by adapting the existing formulation with some modifications by introducing the prospective boundary conditions as efforts to increase the critical velocity and to reduce the top joint stress. The numerical simulation is done using a commercial software Ansys interface. Using scale models, the results obtained from the analytical approach are compared with the results from the numerical ones. The analysis on the analytical and numerical results and the comparison processes are done by utilizing a data processing software Python. Finally, the critical velocity and maximum stress of full scale models are discussed to determine the most prospective material for OTEC utilization.

From the results obtained by both analytical and numerical simulations, the tendency of the critical velocity behavior on the change of the variables are also compared with the existing theory on riser conveying fluid. It is found that the results obtained here agree well with the existing theory. Comparison study between analytical and numerical simulations states that the analytical results are in good agreement with the numerical ones. The final result is the determination of the most prospective material for OTEC riser. Due to its low density but high yield stress, FRP material will be the most suitable material for OTEC utilization among the other examined materials in this study. Considering the obtained value of the vibration frequency, the fatigue analysis is very crucial to be examined and will be done in the near future.

In this paper, the pipe is simplified as a homogeneous structure. For the future work, the stiffening system will be introduced to support the integrity of the riser from local pressure and local bending moment, especially for pinned joint where its maximum bending moment takes place not at the top joint but somewhere along the pipe. Additionally, future research will also focus on the other excitations such as currents, floating structure motions, vortex induced vibration, etc. To increase the confidence of the analytical model, the experiment will be conducted in the near future.

REFERENCES

[III.1] L.A. Vega, Ocean thermal energy conversion. In: R.A. Meyers (Eds.), Encyclopedia of Sustainability Science and Technology vol. 6, Springer, New York, 2012, pp 7296-7328.

[III.2] M.L. Syamsuddin, A. Attamimi, A.P. Nugraha, S. Gibran, A.Q. Afifah, N.Oriana, OTEC potential in the Indonesian seas. Energy Procedia 65 (2015) 215 – 222. https://doi.org/10.1016/j.egypro.2015.01.028.

[III.3] G.C. Nihous, L.A. Vega, Design of a 100 MW OTEC-hydrogen plantship. MAR STRUCT 6 (1993) 207-221. https://doi.org/10.1016/0951-8339(93)90020-4.

[III.4] A. Miller, M. Ascari, OTEC advanced composite cold water pipe: final technical report. https://www.osti.gov/biblio/1024183, 2011 (accessed 10 March 2019).

[III.5] A. Miller, T. Rosario, M. Ascari, Selection and validation of a minimum-cost cold water pipe material, configuration, and fabrication method for ocean thermal energy conversion (OTEC) systems. In: SAMPE, Proceedings of SAMPE 2012, the Society for the Advancement of Material and Process Engineering, Maryland, 2012, pp 1-28.

[III.6] G.C. Nihous, A preliminary assessment of ocean thermal energy conversion resources. J ENERG RESOUR 129 (2007) 10-17. https://doi.org/10.1115/1.2424965.

[III.7] L. Martel, P. Smith, S. Rizea, et al., (2012) Ocean thermal energy conversion life cycle cost assessment: final technical report. https://www.osti.gov/servlets/purl/1045340, 2012 (accessed 10 March 2019).

[III.8] M.P. Païdoussis, N.T. Issid, Dynamic stability of pipes conveying fluid. J Sound Vib 33 (1974) 267-294. https://doi.org/10.1016/S0022-460X(74)80002-7.

[III.9] D.B. Giacobbi, C. Semler, M.P. Païdoussis, Numerical fluid – structure interaction study of a cantilevered pipe discharging or aspirating fluid via a computational fluid dynamics and finite element analysis model. In: M.

Papadrakakis, B.H.V. Topping (Eds.), Proceedings of the Sixth International Conference on Engineering Computational Technology, Civil Comp Press, Greece, 2008, paper 48.

[III.10] D.B. Giacobbi, The dynamics of aspirating cantilevered pipes and pipes conveying variable density fluid (M. Eng Thesis), McGill University, Montreal, 2010.

[III.11] D.B. Giacobbi, S. Rinaldi, C. Semler, M.P. Païdoussis, The dynamics of a cantilevered pipe aspirating fluid studied by experimental, numerical and analytical methods. Journal Fluid Struct 30 (2012) 73-96. https://doi.org/10.1016/j.jfluidstructs.2011.11.011.

[III.12] G.L. Kuiper, A.V. Metrikine, Dynamic stability of a submerged, free-hanging riser conveying fluid. J Sound Vib 280 (2005) 1051-1065. https://doi.org/10.1016/j.jsv.2004.09.024

[III.13] X. Liang, X. Zha, X. Jiang, L. Wang, J. Leng, Z. Cao, Semi-analytical solution for dynamic behavior of a fluid-conveying pipe with different boundary conditions. Ocean Eng 162 (2018) 183-190. https://doi.org/10.1016/j.oceaneng.2018.05.060

[III.14] A. Abbaslou, M.R. Maheri, Prediction of the damping properties of fiber-reinforced polymer composite panels with arbitrary geometries. Proc Inst Mech Eng, Part C 232 (2016) 275-283.https://doi.org/10.1177/0954406216676506

[III.15] H. Bachmann, et al., Vibration problems in structures: practical guidelines, Birkhauser Verlag, Berlin,1995.

[III.16] L. Cremer, M. Heckl, Structure-borne sound, Springer-Verlag, New York, 1988.

[III.17] W. Qi, X. Xu, Analytical method of dynamic properties of FRP based on micromechanical level, Chinese J Aeronaut 28 (2015) 939-945. https://doi.org/10.1016/j.cja.2015.03.008

[III.18] ANSYS inc, ANSYS software version 17, ANSYS help, ANSYS inc, USA,

2017.

[III.19] J.M. Cimbala, A new method for calculating added mass using CFD, In: American physical society, Proceedings of division of fluid dynamics 56th annual meeting, ECT 2008, APS, New Jersey, 2008, KK.007.

[III.20] A. Kuessesh, Added mass formulation for fluid structure interaction (MSc Thesis), American university of Sharjah, UAE, 2016.

[III.21] L. Bonfiglio, S. Brizzolara, C. Chryssostomidis, Added mass and damping of oscillating bodies: a fully viscous numerical approach. In: M.K. Jha, M. lazard et al. (Eds.), Recent advances in fluid mechanics, heat & mass transfer and biology. Harvard University Press, USA, 2012, pp. 210-215.

[III.22] S. Fackrell, Study of the added mass of cylinders and spheres (PhD Thesis), University of Windsor, Canada, 2011.

[III.23] G. Bruschi, T. Nishioka, K. Tsang, R. Wang, A comparison of analytical methods: drag coefficient of a cylinder, University of California (MAE 171A), California, 2003.

[III.24] T. Huang, D.W. Dareing, Natural frequencies of marine drilling risers, J Pet Technol 28 (1976) 813–818. https://doi.org/10.2118/5620-PA.

[III.25] M. Kheiri, M.P. Païdoussis, Dynamics of a pipe conveying fluid flexibly restrained at the ends. Journal Fluid Struct 49 (2014) 360-385. https://doi.org/10.1016/j.jfluidstructs.2013.11.023.

[III.26] Det Norske Veritas, Structural design of offshore units, DNV, Norway, 2012.

CHAPTER IV
GENERAL CONCLUSION

4.1 Main process and results

The main aim of this study is to design the floating struture and Cold Water Pipe for Ocean Thermal Energy Conversion in commerical scale. Eventhough, the design results may still require further improvement and modification, this work gives a deeper understanding on the foundations of the OTEC plantship design processes and procedures.

In the floating structure decision, there are a few types of floating strutures which have been examined by previous researchers. But in this study, to decrease the capital cost, a floating structure from oil tanker conversion for 100 MW-net OTEC power plant is considered. This plantship will be deployed in the west part of Indonesia ocean.

To measure the surface temperature and gradient temperature decrease at substantial depth, the on-site experiment was conducted. From these data, the required seawater debit for producing 100 MW-net electricity and the required length of the risers can be obtained. Keeping the seawater debit constant, the required diameter of the risers and the required size of the seawater tanks can be calculated for various seawater transport velocities. Then, the dry weight and wet weight of the risers are estimated to be included in total weight calculation. From the required size of the tank, the weight of the seawater inside the tank can be calculated.

Targeting net electricity product of 100 MW with 30% energy loss, the major OTEC components are determined. This particular step informed the numbers, required space and required weight of major OTEC components. By varying the location of the heat exchanger to the seawater tank, adding the required capacities of risers, seawater tanks and major OTEC components with 20 % spare for additional equipment, the total required volumetric space and buoyancy can be assessed.

Separately, Monte Carlo Simulation is used to vary the prospective size of the plantship. There are four types of plantship included in the design including Afra-max, Suez-max, VLCC, and ULCC. Comparing the provided capacities with the required capacities obtained previously, the acceptance for particular plantship dimension can be determined. If the provided capacities are not enough to cover the required one, the case will be rejected. If the plantship has enough space and buoyancy, the process will continue to the arrangement of OTEC major components.

The results imply that the most recommended size of the oil tanker ship to be converted is Suez-max type with seawater transport velocities of about 2-3 m/s. It is also preferable to set the location of the OTEC system next to the seawater tanks.

The next part, in order to design a cold water pipe for OTEC application concerning its critical velocity, an analytical solution has been developed and verified using numerical simulation. The analytical solution for free hanging riser with various types of the tip end is governed by including bending motion of the risers, longitudinal tension along the risers, internal flow effect in the terms of transverse loading per unit length, pressure along the pipe wall and force triggered by riser movement. Considering the boundary conditions for particular cases, the general solution can be obtained using power series expansion. The imaginary and real parts of the solutions are plotted in an Argand diagram which are then used to analyze when the instability might occur. Using scaled models, in order to validate the analytical solution, the dynamic behavior observed in the analytical analysis is compared with the one predicted using numerical analysis. Finally, the analytical solution will be used to examine the riser in full scale model.

The term analytical solution in this proposed model is meant referring `analytical` in a strict manner or simply can be summoned as being `semi-analytical` since in the solving procedure, the computational software is necessary. The computational solver used in this analysis is MATLAB. In the case of the numerical analysis, it is done using commercial software ANSYS interface, which can be broadly described as coupled analysis between Computational Structural Mechanics (CSM) and Computational Fluid Dynamics (CFD).

The main results and conclusions for each subtheme have been widely reviewed in each chapter. But in general, gathering the information from chapters 2 and 3 together,

conclusions can be derived as follow: 1) It is possible to consider an oil tanker ship conversion as a plantship for OTEC power plant with pinned or flexible joint to attached the CWP on the plantship; 2) The seawater transport velocity plays an important role in both plantship size decision and pipe stability analysis.

4.2 Practical relevance

For the offshore technology, considering the success of the conversion of oil tanker ship to be FPSO, it is very optimistic that the new floating structure for OTEC technology can be built from an oil tanker ship conversion. This solution will be a `fresh-air` for OTEC development where until now, the solution to minimize the capital cost through the floating stucture choices has not been significantly considered.

In the last couple years, so many oil tanker ships are not operated in Indonesia either because of oil price fluctuation or merely due to the operational age. The idea to convert the oil tanker to be OTEC floating stucture will give an option to enhance the value of the non-operated oil tanker ships.

For design purpose, the interesting point is that, in using a ship conviersion, the main dimensions of the floating stucture has been fixed following the existing size. Thus, the general arrangement must be set to deal with this condition yet the OTEC system equipments should be located in the most-optimum way considering the fact that the location of OTEC system will affect the required pump work. This study provides a comparison study either the OTEC system is located next to seawater tank or above seawater tank. Each option has its own merits and demerits. This study will give the designer an overview on how to locate the OTEC system on the floating structure.

In case of the OTEC CWP, the basic concept is employing and modifying the general solution of a submerged, free-hanging riser conveying fluid. Thus, the results of the riser analysis in this study can also be used to improve the understanding of dynamic behaviour of free hanging riser in general.

In the riser design process, the maximum stress applied on the riser is also investigated as an extent of the critical velocity assessment. Based on the latest author`s reference

review, there are no existing published papers which discuss about the applied stress as a comparison parameter to determine the acceptance model of an analytical solution for free hanging riser. This is also considered as an additional value of this study.

Widely, the concept of OTEC CWP is almost similar with the riser concept for a floating LNG plant. Both risers have large diameter with large capacity of seawater intake. The transported fluid is same, which is seawater. Simply speaking, this study benefits not only limited in the OTEC field but also can be applied in other fields with some extends.

4.3 Recommendation

Designing floating structure for OTEC power plant requires deep understanding and analysis since the project is very large with complex requirements. If one of the systems fails, the global failure might take place. In this study, the design focuses on obtaining the optimum size of the plantship and riser. For futher advancement in the future, the spiral model shown in figure IV.1 is recommended to be utilized as analysis guidelines to determine the supporting system of the floating structure.

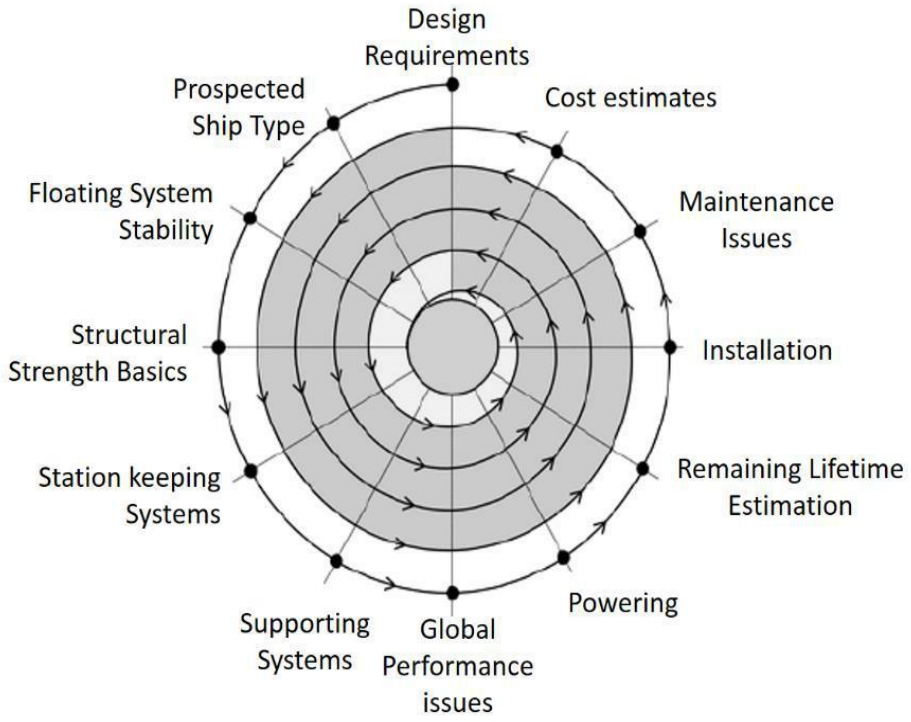

Figure IV.1 Spiral model for further design advancement

The spiral model is a development process model with very high emphasis on details for every particular step. After the process completes one cycle, the process continues from the start point again and then stops after its reaches the most desired condition. This method will lead an incremental refinement through each iteration around the spiral. By employing this method, a floating structure for OTEC power plant can be completely designed based on Indonesia sea condition with very accurate risk and cost evaluation. Based on the proposed spiral model, the detailed analysis which will include:

a. Floating systems stability: Intact stability, wind heel and righting moment, dynamic stability, ballasting requirements, damage stability and compartmentation
b. Structural strength basic: local and global strength
c. Station keeping systems: mooring systems types, environmental forces, mooring components, catenary mooring systems
d. Supporting systems: on-shore and supply vessel
e. Global performance issues: hydrodynamic response analysis, linear response, and RAO
f. Powering: required operational energy

For the riser design, in this study, the considered excitation is only the effect of the internal water intake. As the riser is also subject to external loads such as current, wave, etc, the design of the riser will be also enhanced by considering:

1. Advanced dynamic analysis: must be able to withstand collapsing loads created by suction.
2. Top joint connection: design a flexible connection to embody a sea-water seal and allow movement at the joint through an angle up to as bigger as possible.
3. Stiffening method for the riser design
4. VIV analysis to avoid fatigue damage
5. Extreme analysis
6. Management and operational analysis
    a. Axial Oscillation due to Weather/Environmental Conditions
    b. Lateral Oscillation due to Ocean Loop Current

c. Failure due to Riser Emergency Disconnect from top joint connection.

APPENDIX I
STABILITY AND TRIM ESTIMATION

I. Weight Calculation

I.1 Steel

Ref: Ship design for efficiency and economy (H. Schneekluth)

Wsteel = Weight of the steel
= 26827.71

KG_{steel} = Keel gravity of the steel
= C_{KG} x D + (V_A + V_{DH})/(L_{pp} x B)
= 16.42 m

C_{KG} = Coefficient of gravity
= 0.52-0.54 (0.53 is picked up)
= 0.53

V_A = The volume of superstructure
= 7000 m3

V_A = The volume of deck house
= 5040 m3

LCG_{steel} = Center of gravity from midship

Ref: Parametric Design - Chapter 11, page. 25

LCG_{HS} = -0.15 + LCB (%L)
LCB = % LCB = 2.576 %L
LCG_{HS} = -0.15 + 2.576
= 2.426 %L
= 6.568 m (ϕ)
= 141.943 m (FP)

I.2 Superstructure and deck house

Weigth of poop

Ref: Ship Design for Efficiency and Economy page. 164

Poop Dimensions

L behind AP = 14.25 m
L_P = 35.00 m
B_P = B ship
= 50.00 m
H_P = 4.00 m
V_P = L_P x B_P x H_P
= 35.0 x 50.000 x 4.0
= 3500 m^3

Poop Steel Weight

W_P = C_P x V_P
C_P = 0.075 ton/m^3
= 0.0750 x 3500.000
W_P = 262.500 ton

Center gravity of of poop

Ref: Parametric Design - Chapter 11, page. 25

$KG_P = H + (0.5 \times Hp)$

$H_P =$ 4.00 m

$KG_P = 30.000 + (0.5 \times 4.00)$

$=$ 32 m

$LCG_P = L_{FC\text{-}FP} + L_{CH} + (0.5 \times L_P)$

$L_P =$ 35.00 m

$LCG_P =$ 117.875 m (ϕ)

Weigth of deck house

Ref: Ship Design for Efficiency and Economy page. 164

Deckhouse Dimensions

$L_{DH} =$ 20.00 m

$B_{DH} =$ 50.00 m

$H_{DH} =$ 4.00 m

$V_{DH} = L_{DH} \times B_{DH} \times H_{DH}$

$= 20.0 \times 50.0 \times 4.0$

$=$ 2000.0 m^3

Deckhouse Steel Weight

$W_{DH} = C_{DH} \times V_{DH}$

$C_{DH} =$ Fungsi dari F_O/F_U

$F_O =$ 1750

$F_U =$ 1000

$F_O/F_U =$ 1.75

$C_{DH} =$ 0.093 ton/m^3

$= 0.0930 \times 2000.000$

$W_{DH} =$ 186.000 ton

Center gravity of deck house

Ref: Parametric Design - Chapter 11, page. 25

$KG_{DH} = H + H_P + (0.5 \times H_{FC})$

$H_{DH} =$ 4.00 m

$KG_{DH} = 30.000 + 4.00 + (0.5 \times 4.00)$

$=$ 36 m

$LCG_{DH} = L_{FC\text{-}FP} + L_{CH} + (0.5 \times L_{DH})$

$L_{DH} =$ 20.00 m

$LCG_{DH} =$ 125.375 m (ϕ)

I.3 Fluids on board

W seawater = 60243.75 ton

W water inside HE = 3636.576 ton

W working fluid = 900.00 ton

Total = 64780.33 ton

KG = 13 m

LCG = 6 m (ϕ)

The fluids on board are circulated and located in the tank and HE which placed symetrically to the amidship

I.4 Condenser, Evaporator and turbine

Weight = 48000.00 ton KG = 24 m
LCG = 6 m (ϕ)

The machinary production is located symetrically to the amidship

I.5 Residual weight (position control system, pumping control system, etc)

Weight = 122054.10 ton KG = 15 m
LCG = -4.00 m (ϕ)

I.6 Ballast

Weight = 5485.78 ton KG = 15 m
LCG = 140.375 m (ϕ)

(-) sign indicates that the center of gravity is in front of tha midship

I.7 Risers

	Length (m)	Weigth	KG_{riser} (m)	LCG from ϕ (m)
Cold water inlet	800.00	1487.95	-400	0
Cold water outlet	40.00	29.56	-20	0
Warm water inlet	20.00	12.98	-10	0
Warm water outlet	40.00	41.81	-20	0
Total		1572.30	-379.53	0

In this arrangement the inlet cold water pipe is placed to be at the centerline around midship ant the outlet cold water pipe, inlet warm water pipe and outlet warm water pipe are divided to two pipes which installed symetrically to the midship. Thus the total longitudinal center of gravity will

I.8 Center of mass recapitulation

Without riser (Decoupled)				
No	Items	Weight	KG	LCG
1	Steel	26827.71	16.42	6.57
2	Superstructure and deck hous	448.50	33.66	-120.99
3	Fluids on board	64780.33	13.00	6.00
4	Condenser, evaporator, turbir	41610.00	24.00	6.00
5	Residual weight	61027.05	15.00	-4.00
6	Ballast	5485.78	15.00	140.38
Total		200179.37	16.46	6.43
With riser (Coupled)				
7	Riser	1572.30	-379.53	0.00
Total		201751.67	13.37	6.38

II. Stability (soild) Calculation

Input Data :

L_{PP} =	270.75	m	1 feet =	0.3048	m
B =	50.00	m	L (L_{WL}) =	935.0394	ft
T =	17.00	m	B =	164.042	ft
H =	30.00	m	B_W (Waterline) =	164.042	ft
$V_{S\ (before\ converted)}$ =	8.00	kn	T (Draft) =	55.77428	ft
=	4.12	m/s	D_M (Depth) =	98.4252	ft
ρ =	1.025	ton/m3	S_F (Sheer Fwd.) =	0	ft
V =	274654.5	m3	S_A (Sheer Aft.) =	0	ft
Δ_O =	281520.9	ton	Δ_0 =	281520.86	ton
L_{WL} =	285.00	m	L_d (L Sup.Struct.) =	59.95467	ft
LCB =	6.97	m (fwd. amidship)	d (H Sup.Struct.) =	8.2021	ft
=	128.40	m (from FP)	C_B =	0.838	
=	2.576	% L	C_X (C_M) =	0.995	
LCG =	128.95	m (from FP)	C_W (C_{WP}) =	0.898	
KG =	16.46	m	C_{PV} = C_B / C_W		
			=	0.932629	
			Fn=	0.155228	

The stablity calculation was done using this refference:
Ref: The Theory and Technique of Ship Design (G.C. Manning)

II.1 Basis Calculation

Ref: The Theory and Technique of Ship Design (G.C. Manning), Appendix I, page 252 & 255

A_O = Area of waterline plane at designed draft
= C_W x L x B_W
= 137789.9 ft^2

A_M = Area of immersed midship section
= C_X x B_W x T
= 9108.016 ft^2

S = Mean Sheer (Area of centerline plane above D_M divided by length)
= (L_d x d) + (0.5 x L x (S_F / 3)) + (0.5 x L x (S_A / 3))
= 491.7542 ft^2

A_2 = Area of vertical centerline plane to depth D
= (0.98 x L x $D_{M)}$ + S
= 90682.56 ft^2

D = Mean depth
= (S / L) + D_M
= 98.95112 ft

F = Mean freeboard

= D - H

= 43.17684 ft

A_1 = Area of waterline plane at draft D may be estimated from A_0 and nature of stations above waterline

= 1.01 x A_O

= 139167.8 ft^2

II.2 GZ Coefficient Calculation

Ref: The Theory and Technique of Ship Design (G.C. Manning), Appendix I, page 252 & 255

$\Delta_T = \Delta_0 + ((AO + A1) / 2) \times (F / 35)$

= 452351.7 ton

$\delta = (\Delta_T / 2) - \Delta_0$

= -55345 ton

$C_W' = A_2 / (L \times D)$

= 0.980106

$C_{PV}'' = (35 \times \Delta_T) / (A_2 \times B)$

= 1.064304

$C_W'' = C_W' - ((140 \times \delta) / (B \times D \times L)) \times (1 - C_{PV}'')$

ABS δ = 55344.99

= 1.012934

$C_X' = (A_M + (B \times F_E)) / (B \times D)$

= 0.997455

$C_{PV}' = (35 \times \Delta_T) / (A_1 \times D)$

= 1.1497

KG = 16.45527 m

= 53.9871 ft

$f_1 = (D \times (1 - (A_O / A_1))) / (2 \times F \times (1 - C_{PV}'))$

= -0.07579

$f_0 = (H \times ((A_1 / A_O) - 1)) / (2 \times F \times (1 - C_{PV}))$

= 0.095869

$f_2 = 9.1 \times (C_X' - 0.89)$ (apabila $C_X' < 0.89$, $f_2 = 0$)

= 0.977842

II.3 h Factor Calculation

Ref: The Theory and Technique of Ship Design (G.C. Manning), Appendix I, page 253

Reffering to h factor graph

if $0 <= f_1 <= 0.5$, $h1 = (f = 0) + [(f1 - 0) / (0.5 - 0)] \times ((f = 0.5) - (f = 0))$

unless, $h1 = (f = 0.5) + [(f1 - 0.5) / (1 - 0.5)] \times ((f = 1) - (f = 0.5))$

h_1 = function of C_{PV}' and		h_0 = function of C_{PV} and f		h_2 = function of C_{PV}'' and f	
f (=0) =	0.582	f (=0) =	0.474	f (=0) =	0.529
f (=0.5) =	0.558	f (=0.5) =	0.480	f (=0.5) =	0.521
f (=1) =	0.545	f (=1) =	0.486	f (=1) =	0.516
h_1 =	0.573	h_0 =	0.475	h_2 =	0.516

II.4 GG' Calculation

Ref: The Theory and Technique of Ship Design (G.C. Manning), Appendix I, page 253

$GG' = KG' - KG$

$KG = 53.9871$ ft

$KG' = (D / 2) \times (((1 - h_1) \times \Delta_T - \delta) / \Delta_0)$

$= 43.69023$ ft

$GG' = -10.2969$ ft

II.5 $G'B_O$ Calculation

Ref: The Theory and Technique of Ship Design (G.C. Manning), Appendix I, page 253

$G'B_O = KG' - KB_O$

$KB_O = (1 - h_0) \times H$

$= 29.28465$ ft

$G'B_O = 14.40557$ ft

II.6 $G'B_{90}$ Calculation

Ref: The Theory and Technique of Ship Design (G.C. Manning), Appendix I, page 253

$G'B_{90} = (\Delta_T \times h_2 \times B / 4 \times \Delta_0) - ((\delta^2 / \Delta_0) \times (17.5 / (A_2 - (70 \times (\delta / B) \times (1 - C_{PV}''))))))$

δ = Absolute (+)

$G'B_{90} = 31.93955$ ft

II.7 $G'M_0$ Calculation

Ref: The Theory and Technique of Ship Design (G.C. Manning), Appendix I, page 254

$G'M_0 = KB_O + BM_O - KG'$

$BM_O = (C_l \times L \times B_W^3) / (35 \times \Delta_0)$

$= 29.09811$ ft

$G'M_0 = 14.69253$ ft

Reffering to C_l factor graph

C_l = function of C_W and line 1

$C_l = 0.069$

II.8 $G'M_{90}$ Calculation

Ref: The Theory and Technique of Ship Design (G.C. Manning), Appendix I, page 254

$$G'M_{90} = BM_{90} - G'B_{90}$$

$$BM_{90} = ((C_l' \times L \times D^3) / (35 \times \Delta_0)) + ((L_d \times d \times D^2) / (140 \times \Delta_0))$$

Reffering to C_l factor graph

C_l' = function of C_W'' and line 2

C_l' = 0.089

BM_{90} = 8.33666 ft

$G'M_{90}$ = -23.60289 ft

II.9 b_1, b_2, and b_3 Calculation

Ref: The Theory and Technique of Ship Design (G.C. Manning), Appendix I, page 250

$$b_1 = ((9 \times (G'B_{90} - G'B_0)) / 8) - ((G'M_0 - G'M_{90}) / 32)$$

= 18.529

$$b_2 = (G'M_0 + G'M_{90}) / 8$$

= -1.11379

$$b_3 = ((3 \times (G'M_0 - G'M_{90})) / 32) - ((3 \times (G'B_{90} - G'B_0)) / 8)$$

= -2.98505

II.10 GM_0 Calculation

Ref: The Theory and Technique of Ship Design (G.C. Manning), Appendix I, page 257

$$GM_0 = KB_O + BM_O - KG$$

= 4.395656 ft

II.11 GZ Calculation Table

ϕ	GG' sin ϕ	b_1 sin 2 ϕ	b_2 sin 4 ϕ	b_3 sin 6 ϕ	GZ (ft)	GZ solid (m)
0°	0	0	0	0	0	0
5°	-0.8974	3.21753	-0.3809	-1.4925	0.44663	0.13613
10°	-1.788	6.33729	-0.7159	-2.5851	1.2482	0.38045
15°	-2.665	9.2645	-0.9646	-2.985	2.64985	0.80767
20°	-3.5217	11.9102	-1.0969	-2.5851	4.70647	1.43453
25°	-4.3516	14.194	-1.0969	-1.4925	7.25299	2.21071
30°	-5.1484	16.0466	-0.9646	-4E-16	9.93357	3.02775
35°	-5.906	17.4116	-0.7159	1.49252	12.2821	3.74359
40°	-6.6187	18.2475	-0.3809	2.58513	13.833	4.21629
45°	-7.281	18.529	-1E-16	2.98505	14.2331	4.33823
50°	-7.8879	18.2475	0.38094	2.58513	13.3257	4.06167
55°	-8.4347	17.4116	0.71593	1.49252	11.1853	3.40928
60°	-8.9174	16.0466	0.96457	7.3E-16	8.0938	2.46699
65°	-9.3321	14.194	1.09687	-1.4925	4.46624	1.36131
70°	-9.6759	11.9102	1.09687	-2.5851	0.74606	0.2274
75°	-9.946	9.2645	0.96457	-2.985	-2.702	-0.8236
80°	-10.14	6.33729	0.71593	-2.5851	-5.6723	-1.7289
85°	-10.258	3.21753	0.38094	-1.4925	-8.1518	-2.4847
90°	-10.297	2.3E-15	2.7E-16	-1E-15	-10.297	-3.1385

II.12 h Calculation

h (radian)= ϕ / (180/Π)

ϕ = 5°

h (radian)= 0.08727

II.13 Area Under the Righting Lever Curve Calculation

Simpson from 0 - 10 degree = 1/3 x h x (a + (4 x b) + c)

Degree	A (ft.rad)	A (m.rad)
0° - 10°	0.08828	0.02691
10° - 20°	0.48154	0.14677
20° - 30°	1.26978	0.38703
30° - 40°	2.12043	0.64631
0° - 40°	3.96003	1.20702

II.14 GZ Curve

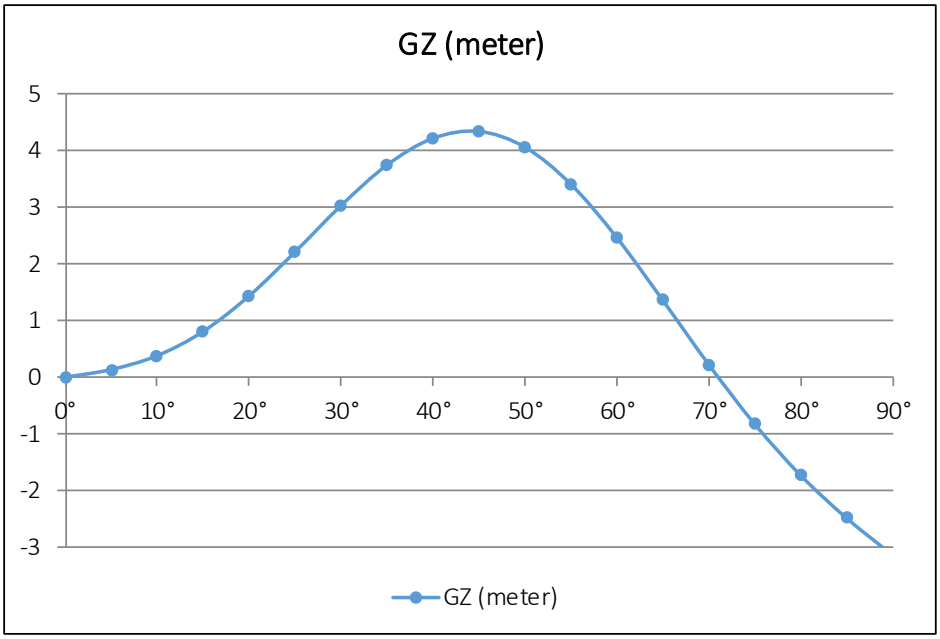

II.14 Maximum Heel Angle Calculation

Maximun	GZ max =	4.338 m	*; maximum value of GZ*
	Column =	10	*; number of column at maximum value of GZ*
	Heel at GZ max =	45°	*; heel angle at GZ max*

Spot	X_1 =	40°
	X_2 =	45°
	X_3 =	50°
	Y_1 =	4.21629 m
	Y_2 =	4.33823 m
	Y_3 =	4.06167 m

Matrix		
1	40	1600
1	45	2025
1	50	2500

Invers of Matrix		
45	-80	36
-1.9	3.6	-1.7
0.02	-0.04	0.02

Matrix calculation

a	=	-11.105
b	=	0.70184
c	=	-0.008
		; Maximum angle
θ_{Max}	=	44.03°

III. Stability (riser effect) Calculation

Input Data :

L_{PP} =	270.75	m	1 feet =	0.3048	m
B =	50.00	m	L (L_{WL}) =	935.0394	ft
T =	17.00	m	B =	164.042	ft
H =	30.00	m	B_W (Waterline) =	164.042	ft
$V_{S\ (before\ converted)}$ =	8.00	kn	T (Draft) =	55.77428	ft
=	4.12	m/s	D_M (Depth) =	98.4252	ft
ρ =	1.025	ton/m3	S_F (Sheer Fwd.) =	0	ft
V =	274654.5	m3	S_A (Sheer Aft.) =	0	ft
Δ_O =	281520.9	ton	Δ_0 =	281520.86	ton
L_{WL} =	285.00	m	L_d (L Sup.Struct.) =	59.95467	ft
LCB =	4.96	m (fwd. amidship)	d (H Sup.Struct.) =	8.2021	ft
=	140.33	m (from FP)	C_B =	0.838	
=	1.832	% L	C_X (C_M) =	0.995	
LCG =	129.00	m (from FP)	C_W (C_{WP}) =	0.898	
KG =	13.37	m	C_{PV} = C_B / C_W		
			=	0.932629	
			Fn=	0.155228	

Riser

	Length	Weight (ton)	KG (m)
Cold water inlet	800	1700	-400
Cold water outlet	40	39	-20
Warm water inlet	20	17	-10
Warm water outlet	40	56	-20

III.1 Restoring moment

ϕ	Sin ϕ	Restoring moment					GZ correction	GZ coupled
		CW inlet	CW outlet	WW inlet	WW outlet	Total		
0°	0	0	0	0	0	0	0	0
5°	0.08719	59289.7	68.0088	14.8224	97.6536	59470.271	0.211246	0.347379
10°	0.17372	118127.8	135.5	29.532	194.563	118487.57	0.420884	0.801334
15°	0.25892	176066.2	201.958	44.0165	289.991	176602.39	0.627315	1.434989
20°	0.34215	232663.5	266.879	58.1659	383.21	233372.07	0.828969	2.263501
25°	0.42278	287488.6	329.766	71.8722	473.511	288364.22	1.024309	3.23502
30°	0.50018	340124.1	390.142	85.031	560.204	341159.98	1.211846	4.239598
35°	0.57378	390168.9	447.547	97.5422	642.631	391357.22	1.390154	5.133739
40°	0.643	437241.9	501.542	109.31	720.163	438573.59	1.557872	5.774165
45°	0.70733	480984.6	551.718	120.246	792.21	482449.47	1.713725	6.051959
50°	0.76627	521063.7	597.691	130.266	858.223	522650.66	1.856526	5.918199
55°	0.81937	557174	639.111	139.294	917.698	558870.97	1.985185	5.394467
60°	0.86624	589040.5	675.664	147.26	970.184	590834.51	2.098724	4.565713
65°	0.9065	616420.5	707.071	154.105	1015.28	618297.82	2.196277	3.557588
70°	0.93986	639105.3	733.091	159.776	1052.64	641051.72	2.277102	2.5045
75°	0.96606	656922.2	753.528	164.231	1081.99	658922.91	2.340583	1.517015
80°	0.98491	669735.5	768.226	167.434	1103.09	671775.27	2.386236	0.657304
85°	0.99625	677447.7	777.072	169.362	1115.8	679510.89	2.413714	-0.07094
90°	1	679999.9	780	170	1120	682070.86	2.422808	-0.71568

III.2 h Calculation

h (radian)= ϕ / (180/Π)

ϕ = 5°

h (radian)= 0.087266

III.3 Area Under the Righting Lever Curve Calculation

Simpson from 0 - 10 degree = 1/3 x h x (a + (4 x b) + c)

Degree	A (m.rad)
0° - 10°	0.063729
10° - 20°	0.256121
20° - 30°	0.565579
30° - 40°	0.888626
0° - 40°	1.774056

IV. Intact Stability Criteria

Ref: IMO Resolution A.749 (18) - Intact Stability (IS) Code

Input Data :

Criteria	GZ		GZ	
e 0 - 30° =	0.56	m.rad	0.89	m.rad
e 0 - 40° =	1.21	m.rad	1.77	m.rad
e 30° - 40° =	0.65	m.rad	0.89	m.rad
GZ 30° =	3.03	m	4.24	m
θ Max (°) =	44.03	°	46.35	°
GM° (ft) =	4.396	ft	2.781	ft
GM° (m) =	1.3398	m	0.84765	m

IV.1 IMO Resolution A.749 (18) Criteria

- The area under the righting lever curve (GZ curve) should not be less than 0.055 m.rad up to θ = 30° angle of heel
- The area under the righting lever curve (GZ curve) should not be less than 0.09 m.rad up to θ = 40° angle of heel
- 30° - 40° should not be less than 0.03 m.rad
- The righting lever GZ should be at least 0.20 m at an angle of heel equal to or greater than 30°
- The maximum righting arm should occur at an angle of heel preferably exceeding 30° but not less than 25°
- The initial metacentric height GM_0 should not be less than 0.15 m

IV.2 Intact Stability Acceptable Criteria

Criteria		GZ decoupled	GZ Coupled
e 0 - 30° ≥	0.055 m.rad	Accepted	Accepted
e 0 - 40° ≥	0.09 m.rad	Accepted	Accepted
e 0 - 30° ≥	0.03 m.rad	Accepted	Accepted
GZ 30° ≥	0.2 m	Accepted	Accepted
θ Max ≥	25 °	Accepted	Accepted
GM_0 ≥	0.15 m	Accepted	Accepted
STATUS =		ACCEPTED	ACCEPTED

V. trim calculation

Input Data :

L_{PP} =	270.75	m	L_{WL} =	285.00	m
B =	50.00	m	LCB =	6.97	m (fwd. amidship)
T =	17.00	m	=	128.40	m (from FP)
H =	30.00	m	=	2.58	% L
V_S =	8.00	kn	LCG =	136.62	m (from FP)
=	4.12	m/s	KG =	16.46	m
ρ =	1.03	ton/m3	C_B =	0.838	
V =	274654.50	m3	C_M =	0.995	
Δ =	281520.86	ton	C_{WP} =	0.898	

LCG of ballast from amidship (m)	Final LCG (m)	LCG of ballast from amidship (m	Final LCG (r
-140	-1.25	20	3.10
-120	-0.70	40	3.65
-100	-0.16	60	4.19
-80	0.38	80	4.73
-60	0.93	100	5.28
-40	1.47	120	5.82
-20	2.01	140	6.37
0	2.56		

Trim calculation referred to:
Ref: Parametric Design - Chapter 11.

V.1 Vertical Center of Bouyancy (KB) Calculation

Ref: Parametric Design - Chapter 11. page 17-18

KB = Center of bouyancy to the keel
KB = (KB / T) x T

For C_M > 0.9 the calculation is as follow:

KB / T = $(1 + C_{WP})^{-1}$
= (1 + 0.898) ^-1
= 0.526781
KB = 0.527 x 17.00
= 8.955272 m

V.2 Location of Metacenters at Tranverse Direction (BM_T) Calculation

Ref: Parametric Design - Chapter 11. page 18-19

BM_T = Center of bouyancy to transverse metacenter

$BM_T = I_T / \nabla$

I_T = Moment of inertia of waterplane relative to ship's transverse axis

$I_T = C_I \times L \times B^3$

C_I = Transverse inertia coefficient

= $0.1216 \times C_{WP} - 0.0410$ (D'Arcangelo Tranverse)

= $0.1216 \times 0.898 - 0.0410$

= 0.068236

$I_T = 0.068 \times 270.750 \times (50.000 \text{ ^3})$

= 2309365

BM_T = 2309365.324 / 274654.500

= 8.408256 m

V.3 Location of Metacenters at Longitudinal Direction (BM_L) Calculation

Ref: Parametric Design - Chapter 11. page 18-19

BM_L = Center of bouyancy to longitudinal metacenter

$BM_L = I_L / \nabla$

I_L = Moment of inertia of waterplane relative to ship's longitudinal axis

$I_L = C_{IL} \times B \times L^3$

C_{IL} = Longitudinal inertia coefficient

= $0.350 \times C_{WP}^2 - 0.405 \times C_{WP} + 0.146$ (D'Arcangelo Longitudinal)

= $0.350 \times (0.898\text{^2}) - 0.405 \times 0.898 + 0.146$

= 0.064624

$I_T = 0.065 \times 50.000 \times (270.750 \text{ ^3})$

= 64130875

BM_L = 64130875.046 / 274654.500

= 233.4965 m

V.4 Longitudinal Metacenters Height (GM_L) Calculation

Ref: Parametric Design - Chapter 11. page 18-19

GM_L = Longitudinal distance between CoG and longitudinal bouyancy metacenter

= $BM_L + KB - KG$

= $233.497 + 8.955 - 16.455$

= 226.00 m

V.5 Trim Calculation

Ref: Parametric Design - Chapter 11. page 27

Trim = $T_A - T_F$

= ((LCG - LCB) x L) / GM_L

Recommendation criteria = 1% x L

= 1% x 270.750

= 2.7075

LCG of ballast from amidship (m)	LCG from F	Trim (m)	Status	Conclusion
-140	136.62	9.85	rim by ster	Not recommended
-120	136.08	9.20	rim by ster	Not recommended
-100	135.54	8.55	rim by ster	Not recommended
-80	134.99	7.90	rim by ster	Not recommended
-60	134.45	7.24	rim by ster	Not recommended
-40	133.90	6.59	rim by ster	Not recommended
-20	133.36	5.94	rim by ster	Not recommended
0	132.82	5.29	rim by ster	Not recommended
20	132.27	4.64	rim by ster	Not recommended
40	131.73	3.99	rim by ster	Not recommended
60	131.19	3.34	rim by ster	Not recommended
80	130.64	2.68	rim by ster	Recommended
100	130.10	2.03	rim by ster	Recommended
120	129.55	1.38	rim by ster	Recommended
140	129.01	0.73	rim by ster	Recommended

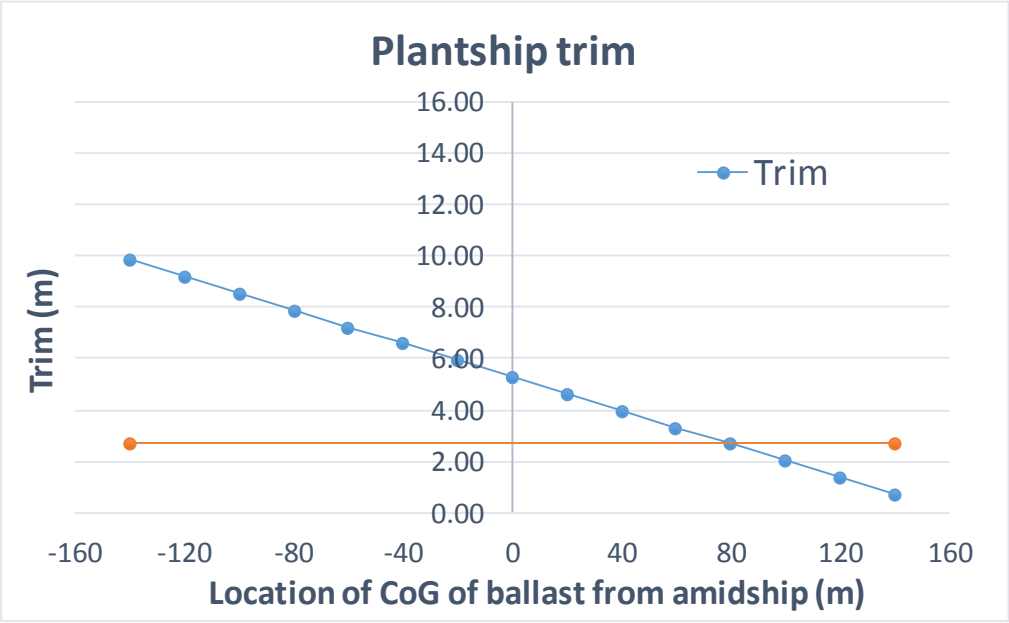

APPENDIX II

BUILDING GENERAL SOLUTION FOR RISER DYNAMIC

Governing general equation.

The equation can be governed based on several terms including bending motion of the beam, longitudinal tension in the riser, internal flow effect in terms of transverse loading per unit length, pressure along the pipe wall and the force triggered by riser movement.

Bending motion of the beam. The riser is supended with the length of l, constant density ρ_r, and cross sectional area A_r. The transverse displacement of the cross section at the distance from the top tip joint z at time t is denoted by $w(z,t)$. According to the Euler- Bernoulli theory, the motion of the beam can be written as

$$EI\left[1+\left(\frac{\mu}{\Omega}\right)\frac{\partial}{\partial t}\right]\frac{\partial^4 w}{\partial z^4}+m_r\frac{\partial^2 w}{\partial t^2}=f_b \tag{1}$$

f_b is the reaction force due to beam motion and m_r is mass of the riser per unit length which can be defined as

$$m_r = A_r \times \rho_r \tag{2}$$

Longitudinal tension. The second term is concerning the tension due to gravity acceleration and internal fluid resistance. Literally, each term can be denoted as

$$w_r = \rho_r A_r g(L-z)+W_c \tag{3}$$

$$w_b = \rho_f A_r g L \tag{4}$$

$$w_i = \rho_f A_i \frac{f_{DW}}{D_i}\frac{u_f^2}{2}(L-z) \tag{5}$$

w_r is the longitudinal tension due to weight of the riser below z point, W_c is the weight of the clump. w_b is bouyancy force in the upward direction, w_i is longitudinal tension due to internal fluid resistance, g is gravity accelaration, L is length of the riser, f_{DW} is the resistance coefficeint of Darcy-Weisbach, ρ_f is fluid density and D_i is inner diameter of the pipe. Summing up all equation above with considering the direction of the force, the tension reads

$$T_r(z) = w_r - w_b - w_i \tag{6}$$

$$T_r(z) = \rho_r A_r g(L-z) - \rho_f A_r g L - \rho_f A_i \frac{f_{DW}}{D_i}\frac{u_f^2}{2}(L-z) \tag{7}$$

The effect of the longitudinal tension to the riser movement is defines as

$$f_t = \frac{\partial}{\partial z}\left(T_r(z)\frac{\partial w}{\partial z}\right) \tag{8}$$

Internal flow effects. The internal flow of the fluid is assumed as a plug flow which means the flow can be investigated as if it was an infinitely flexible rod travelling through the pipe. Thus, the acceleration of the flow can be estimated as

$$a_f = \frac{d^2w}{dt^2}\Big|_{z=u_f t} = \frac{d}{dt}\left(\frac{\partial w}{\partial t} + \frac{\partial w}{\partial z}u_f\right)\Big|_{z=u_f t} = \frac{\partial^2 w}{\partial t^2} + 2u_f\frac{\partial^2 w}{\partial t \partial z} + {u_f}^2\frac{\partial^2 w}{\partial z^2} \tag{9}$$

Equation (9) shows that the acceleration of the internal flow consists of 3 terms: local acceleration, $\frac{\partial^2 w}{\partial t^2}$; Coriolis acceleration, $2u_f\frac{\partial^2 w}{\partial t \partial z}$; and centripetal acceleration, ${u_f}^2\frac{\partial^2 w}{\partial z^2}$. As the acceleration works on the fluid mass $m_f = \rho_f A_i$, the force due to internal flow will be

$$f_f = a_f \times m_f = m_f\left(\frac{\partial^2 w}{\partial t^2} + 2u_f\frac{\partial^2 w}{\partial t \partial z} + {u_f}^2\frac{\partial^2 w}{\partial z^2}\right) \tag{10}$$

Pressure along the pipe. There are two main pressure acting on the riser which are caused by internal and external fluid. Disregarding the temperature difference along the pipe, the pressure due to external fluid can be simply estimated as

$$p_e(\mathrm{z}) = \rho_f g z \tag{11}$$

The equation of internal pressure can be estimated as

$$p_i(z) = \rho_f g z - \rho_f \frac{f_{DW}}{D_i}\frac{u_f^2}{2}(L - z) \tag{12}$$

Dynamic motion due to surrounding water. The dynamic reaction, $\boldsymbol{f_r}(\mathbf{z}, \mathbf{t})$ is a superposition of an inertia force, $\boldsymbol{f_{in}}(\mathbf{z}, \mathbf{t})$ and a drag force $\boldsymbol{f_{drag}}(\mathbf{z}, \mathbf{t})$. The inertia force can be estimated by

$$f_{in}(z,t) = \rho_f A_e (C_a + 1)\frac{\partial u}{\partial t} - m_a \frac{\partial^2 w}{\partial t^2} \tag{13}$$

where A_e is external cross section area of the pipe, C_a is added mass coefficient and m_a is added mass, u is the velocity of external flow.

The second term of the dynamic reaction is drag force. In the real condition, the drag force is influenced by wall surface roughness, water turbulance, Reynold number, etc. In this calculation, all these effects and the non liniarity are disregarded. Hence, the liniarized drag force equation expression is used.

$$f_{drag}(z,t) = \frac{1}{2}\rho_f D_o \widetilde{C_d}(u - \frac{\partial w}{\partial t}) \tag{14}$$

where $\widetilde{C_d}$ is adapted drag coefficient and D_o is the outer diameter of the riser. Summing up the inertia force and drag force, the dynamic reaction due to surrounding water can be obtained as

$$f_r(\mathrm{z},\mathrm{t}) = \rho_f A_e (C_a + 1)\frac{\partial u}{\partial t} - m_a \frac{\partial^2 w}{\partial t^2} + \frac{1}{2}\rho_f D_o \widetilde{C_d}(u - \frac{\partial w}{\partial t}) \tag{15}$$

General equation. In essense, the system is a submerged beam influenced by external and internal pressure with longitudinal tension which then triggers drag motion as the response of the surrounding water. Mathematically, the equation can be built as

$$f_b(\mathrm{z},\mathrm{t}) + f_t(\mathrm{z},\mathrm{t}) + f_f(\mathrm{z},\mathrm{t}) + p_i(z) = f_r(\mathrm{z},\mathrm{t}) \tag{16}$$

Substituting Eq. (1,8,10,12) and (15) into Eq. (16) and doing mathematical modification, the new general equation can be built as

$$EI\left[1+\left(\frac{\mu}{\Omega}\right)\frac{\partial}{\partial t}\right]\frac{\partial^4 w}{\partial z^4}-2u_f m_f\frac{\partial^2 w}{\partial t\partial z}+(m_f+m_r+m_a)\frac{\partial^2 w}{\partial t^2}+\left[-T_{BT}\left(1-\frac{Z}{L}\right)-W_c+{m_f u_f}^2\right]\frac{\partial^2 w}{\partial z^2}+\frac{T_{top}}{L}\frac{\partial w}{\partial z}+\frac{1}{2}\rho_f D_o\widetilde{C_d}\frac{\partial w}{\partial t}=0 \quad (17)$$